Complete Measurement of the Top-quark Polarization in T-channel Single Top-quark Production Using Pp Collisions at 13 TeV with the ATLAS Detector

by

Runyu Bi

BSc, University of Rochester, 2015

Submitted to the Graduate Faculty of

the Dietrich School of Arts and Sciences in partial fulfillment

of the requirements for the degree of

Doctor of Philosophy

University of Pittsburgh

2020

UNIVERSITY OF PITTSBURGH

DIETRICH SCHOOL OF ARTS AND SCIENCES

This dissertation was presented

by

Runyu Bi

It was defended on

May 15, 2020

and approved by

Dr. Joseph F. Boudreau, Committee Chair, University of Pittsburgh

Dr. James A. Mueller, Professor, University of Pittsburgh

Dr. Tao Han, Distinguished Professor of High Energy Physics, University of Pittsburgh

Dr. Andrew R. Zentner, Professor, University of Pittsburgh

Dr. Manfred Paulini, Professor, Carnegie Mellon University

Complete Measurement of the Top-quark Polarization in T-channel Single Top-quark Production Using Pp Collisions at 13 TeV with the ATLAS Detector

Runyu Bi, PhD

University of Pittsburgh, 2020

The top quarks are undoubtedly one of the most promising and experimentally relevant probes into finding new physics. They can be produced in charged-current electroweak processes via a Wtb vertex. Its unique mass scale led to a late discovery in experiment — until 1995 at the Tevatron proton-antiproton collider at Fermilab on the events from top pair production. The observation of the electroweak single top process was established even later — in 2009, also at Fermilab based on 2.3 fb^{-1} and 3.2 fb^{-1} of CDF/$D\emptyset$ data. Nowadays, the high energy proton-proton collider — the Large Hardon Collider (LHC), with a data set of 139 fb^{-1} from the ATLAS detector, makes it possible to perform precision measurements on top quarks using both $t\bar{t}$ and single top channels.

At the LHC, electroweak production of single top quarks in the t-channel leads, in the standard model, to a high degree of top quark polarization. Two subprocesses, $ub \to dt$ and $\bar{d}b \to \bar{u}t$ contribute to t-channel production of single top, while the charge-conjugate processes contribute to production of antitop. The top (antitop) quark spin is expected to be polarized along(opposite to) the direction of the light-quark momentum. In this thesis I present a measurement of the top quark polarization produced within a fiducial region of acceptance, using an integrated luminosity 139 fb^{-1} of proton-proton collisions at 13 TeV, collected by the ATLAS detector. The top decay chain: $t \to W^+b \to l^+\nu b$, include a lepton, a neutrino and a b quark in the final state, which interact with the ATLAS detector, allowing the top quark to be fully reconstructed. From the angular distribution of the top quark decay products, we obtain all three components of the polarization of both top quarks and top anti-quarks.

Table of Contents

List of Tables

List of Figures

Preface

I dedicate this thesis to my parents for their unconditional love and support. I would not have the courage and perseverance to carry through all the ups and downs during this challenging study. Moreover, I would like to express my gratitude to my beloved fiancé, Kyle, for believing in me during this stressful time. It would not be the same without you.

致亲爱的爸妈: 万分感激多年来的支持和鼓励，让我能相信自己，并且完成这个从小的梦想。在外求学的这些日子，辛苦你们了。

1.0 Theoretical Framework

"What is the universe made of?"

Across various cultures around the globe, this question intrigued philosophers. Around the fourth century BC, Chinese philosophers from Daoism interpreted the universe in a fivefold conceptual scheme called "五行(wǔ xíng)" ("Five Phases"), consisting of wood, fire, earth, metal, and water. Similarly in the west, the ancient Greek philosophers, exemplified by Aristotle, reduced the components of matter down to four elements: fire, air, water and earth. Neither claim was based on evidence. However, around 450 BC, the ancient Greek philosophers Leucippus and his pupil Democritus conceived the idea of the atom, meaning "uncuttable", proposing a discrete unit that constitutes all matter. After 2000 years, in 1808, English chemist John Dalton revived the concept with his famous "atomic theory", and presented scientific evidence for atoms. It was then widely accepted that atoms were the smallest division of matter. In 1897, British physicist J. J. Thomson measured the mass of the "cathode ray" to be 1800 times lighter than the hydrogen atom, showing that atoms are not elementary after all[1]. The discovery of this light particle, later known as the "electron", kicked off the ever evolving search for subatomic particles that continues today as high energy physics. During this past century, high energy experiment has evolved from small-scale experiments to large collaborations comprised of hundreds of institutions around the world: ATLAS consist of about 3000 scientific authors from 183 institutions, representing 38 countries; while CMS consist of around 200 institutes and universities from more than 40 countries. Among the many topics under investigation at these experiments are the properties of the top quark with a mass of 172.9 ± 0.4 GeV ($340,000$ times the electron mass), as well as the existence of the Higgs boson discovered in 2012 by both the ATLAS[2] and CMS[3] collaborations.

1.1 Overview the Standard Model

The Standard Model (SM) is a relativistic gauge field theory providing a theoretical framework for all known matter and their mutual interactions. It utilizes the principle of gauge symmetry to

achieve a unification of various subatomic interactions observed in the universe. The symmetry group of the SM is the $SU(3)_C \otimes SU(2)_L \otimes U(1)_Y$, where "$C$" stands for "color," the quantum number in strong interaction, "L" stands for "left-handed," indicating a chiral theory, and "Y" stands for "hypercharge," the quantum number in electroweak interactions.

There are in total 17 elementary particles in the SM, which can be divided into two groups: fermions and bosons. Fermions following Dirac-Fermi statistics, are the building blocks of matter. Some representatives are top quarks, electrons and electron neutrinos. The latter two, along with the muon, the tau, and their corresponding neutrinos, are referred to as leptons. Bosons are the force mediators, which transmit the strong, weak and electromagnetic interactions, following Bose-Einstein statistics. They include photons, gluons and W/Z bosons, which correspond to electromagnetic, strong and weak forces, respectively. Gravitation, with its supposed particle "graviton", lies outside of the Standard Model, and is considered to be a property of spacetime rather than an interaction.

In the electroweak sector, the flavor symmetry of the quarks is broken, giving us six "flavors": up, down, charm, strange, top and bottom. There are also three generations of quarks which consist of $\binom{u}{d}$, $\binom{c}{s}$ and $\binom{t}{b}$, each quark having a different mass. The existence of exactly three generations remains unexplained in the SM[1].

Both leptons and quarks are fermions and both are arranged into *generations*. Table 1 summarizes the properties of the leptons and quarks in the SM. Since leptons do not possess colors, they do not undergo strong interactions.

The other category of the elementary particles in the SM are bosons, which are the force carriers with integer spins, in contrast to fermions with half-integer spins. In addition to the four vector gauge bosons, there is one scalar boson: the Higgs boson. As their name suggests, gauge bosons arise from gauge symmetries. The number of gauge bosons is equal to the number of generators of each symmetry group. In Quantum Electrodynamics (QED), one gauge boson, the photon, mediates the electromagnetic force, corresponding to the single generation of $U(1)$ symmetry. In weak interaction, there are $W(+/-)$ and Z bosons, reflecting the $SU(2)$ group symmetry ($N^2 - 1 = 2^2 - 1 = 3$). Similarly, in QCD, there are eight massless gluons with different color charge combinations, arising from the $SU(3)$ group symmetry. Finally, the Higgs boson, the only

[1]This reminds the author of a famous quote by the Nobel laureate I. I. Rabi: "Who ordered that?"

Generation	lepton/quark	charge $[Q/e]$	mass [GeV]
First	e	-1	0.511×10^{-3}
	ν_e	0	$< 0.225 \times 10^{-6}$ (95% C.L.)
Second	μ	-1	0.106
	ν_μ	0	$< 0.19 \times 10^{-3}$ (90% C.L.)
Third	τ	-1	1.777
	ν_τ	0	< 0.182 (95% C.L.)
First	u	+2/3	2.2×10^{-3}
	d	-1/3	4.7×10^{-3}
Second	c	+2/3	1.27
	s	-1/3	$< 96 \times 10^{-3}$
Third	t	+2/3	173.2
	b	-1/3	4.18

Table 1: The fermions in the SM. Their masses are taken from Reference[4].

scalar boson, plays a consequential role in giving masses to the otherwise massless W/Z bosons as well as to the fermions.

Boson	charge $[Q/e]$	mass [GeV]	interaction
γ	0	0	electromagnetic
$W^\pm$	$\pm$ 1	80.4	weak
Z	0	91.2	weak
g	0	0	strong

Table 2: The bosons in the SM. Their masses are taken from Reference[4].

1.1.1 Quantum Field Theory

Quantum Field Theory (QFT) combines quantum theory, fields, and relativity[5], offering the essential tools in particle physics to predict the dynamics and interactions of all particles. Its rigorous structure provides for unprecedented precision in SM predictions, but also imposes strict

requirements such as re-normalizability upon physics both within and beyond the SM.

The temporal evolution of particles are governed by the Lagrangian L, which in QFT is replaced by the Lagrangian density[2] $\mathcal{L}$ depending upon fields ϕ_k and their derivatives $\partial_\mu \phi_k$. It appears as the integrand in the formulation of the action S:

$$S = \int dt L = \int d^4x \mathcal{L}(\phi_k, \partial_\mu \phi_k). \tag{1}$$

Hamilton's principal states that nature takes the path that minimizes the action, namely:

$$\delta S = \delta \int d^4x \mathcal{L}(\phi_k, \partial_\mu \phi_k) = 0. \tag{2}$$

This leads to the Euler-Lagrangian equation of motion for a field:

$$\partial_\mu \left(\frac{\partial_\mu \mathcal{L}}{\partial(\partial_\mu \phi_k)} \right) - \frac{\partial \mathcal{L}}{\partial \phi_k} = 0. \tag{3}$$

The set of continuous transformations on the fields is called a symmetry if it leaves the equations of motion invariant. Infinitesimal transformations are:

$$\phi_k(x) \to \phi_k(x) = \phi_k(x) + \epsilon \frac{\partial \phi_k}{\partial \epsilon} \phi(x). \tag{4}$$

A symmetry transformation is one which leaves the Lagrangian invariant, or modified by, at most , the four divergence of some four-vector field J^μ:

$$\mathcal{L}(x) \to \mathcal{L}'(x) = \mathcal{L}(x) + \epsilon \partial_\mu J^\mu(x). \tag{5}$$

Plugging into (3), one obtains Noether's theorem:

$$\partial_\mu j^\mu = 0, \text{for } j^\mu(x) = \frac{\partial \mathcal{L}}{\partial(\partial_\mu \phi_k)} \Delta \phi_k - J^\mu \,, \tag{6}$$

where J^μ is a conserved current (Noether current). According to Noether's theorem, symmetries of the Lagrangian are associated with conserved quantities.

[2]The Lagrangian density will be referred to simply as the "Lagrangian" for the rest of the dissertation.

1.1.2 Quantum Electrodynamics

Quantum Electrodynamics (QED) is an Abelian gauge theory with the symmetry group U(1), governing the electromagnetic interactions. It possesses local gauge symmetry under the transformation:

$$\psi \to \psi' = U\psi = \exp(-ieQ\theta)\psi, \tag{7}$$

where $e, Q,$ and θ are all real numbers. In terms of real physical quantities, e is the gauge coupling constant for the U(1) group, Q is the electric charge of a field, and θ is a phase parameter. The full Lagrangian of QED takes the form:

$$\mathcal{L}_{QED} = i\bar{\psi}\gamma^{\mu}D_{\mu}\psi - m\bar{\psi}\psi - \frac{1}{4}F_{\mu\nu}F^{\mu\nu}, \tag{8}$$

where ψ represents the spinor field for fermions, γ^{μ} denotes the Dirac matrices, D_{μ} is the covariant derivative defined by

$$D_{\mu} = \partial_{\mu} + ieQA_{\mu}, \tag{9}$$

A_{μ} being the gauge field that undergoes the gauge transformation:

$$A_{\mu} \to A'_{\mu} = A_{\mu} + \partial_{\mu}\theta, \tag{10}$$

and $F^{\mu\nu}$ being the electromagnetic field strength tensor defined by:

$$F^{\mu\nu} = \partial^{\mu}A^{\nu} - \partial^{\nu}A^{\mu}. \tag{11}$$

The spin-1 gauge boson for QED is the photon. Following the procedure from (4), one obtains the Noether current for QED:

$$j^{\mu} = eQ\bar{\psi}\gamma^{\mu}\psi. \tag{12}$$

The conserved quantity associated with this current is the electric charge Q.

1.1.3 Quantum Chromodynamics

Quantum Chromodynamics (QCD) is a non-Abelian gauge theory describing the strong interactions. Its gauge group, $SU(3)$, avoids long-range force mediators and also gives rise to quark confinement. In $SU(3)$, the local gauge transformation takes the form:

$$\psi \to \psi' = U(\theta)\psi = \exp(-i\frac{\lambda_a}{2}\theta_a)\psi, \tag{13}$$

where λ denotes the Gell-Mann matrices, which generated $SU(3)$ and which obey the commutation relations:

$$\left[\lambda^a, \lambda^b\right] = 2if^{abc}\lambda^c, \tag{14}$$

where f^{abc} are the structure constants of $SU(3)$, which are real and totally antisymmetric. The non-vanishing structure constants have the values:

$$\begin{gathered} f^{123} = 1\,, \\ f^{147} = -f^{156} = f^{246} = f^{257} = f^{345} = -f^{367} = 1/2\,, \\ f^{458} = f^{678} = \sqrt{3}/2\,, \end{gathered}$$

The Lagrangian for QCD is:

$$\mathcal{L}_{QCD} = \bar{\psi}(i\gamma^\mu D_\mu - m)\psi - \frac{1}{4}G^a_{\mu\nu}G^{\mu\nu}_a, \tag{15}$$

where the covariant derivative $D_\mu = \partial_\mu - ig_s A_\mu$, contains A_μ the gauge field of QCD that can be identified with gluons, and the gluon field tensor $G^a_{\mu\nu}$ is analogous to the electromagnetic field strength tensor such that:

$$G^{\mu\nu}_a = \partial^\nu A^\mu_a - \partial^\mu A^\nu_a - g_s f^{abc} A^\nu_b A^\mu_c. \tag{16}$$

1.1.4 Electroweak Theory

In the electroweak sector of the Standard Model, the symmetries that give rise to the interaction are hidden, reflection symmetry (parity) is absent, and charge parity symmetry is broken. An experiment conducted by C.S. Wu in 1956[6], proposed by late Nobel prize winners Tsung-Dao Lee and Chen-Ning Yang, surprised the physics world with strong evidence of violation of parity in the weak interaction. The combined symmetry of Charge-Parity (CP), which also indicates a symmetry between matter and anti-matter, was however still considered as a good symmetry. In 1964, James Cronin, Val Fitch and collaborations discovered CP violation in the decays of neutral kaons[7], for which they were awarded the Nobel prize in 1980. Although the weak interaction shows only a very small amount of CP violation, it is a crucial and intriguing element of the SM, and may play a role in explaining baryogenesis in the early universe.

1.1.4.1 The Weak Interaction The gauge symmetry for the weak interaction is $SU(2)$. However, in order to incorporate the charge and parity violating nature into the theory, a Vector minus Axial vector (V-A) structure (as shown in Table 3) is included in the Lagrangian. Hence, the gauge symmetry is actually $SU(2)_L$, and the local gauge transformation takes the form:

$$\psi_L = \frac{1}{2}(1-\gamma^5)\psi \rightarrow \psi'_L = \exp[1 + ig\vec{T}\cdot\vec{\alpha}(x)]\psi_L, \tag{17}$$

where $\vec{T} = \frac{\vec{\sigma}}{2}$ are generators of the $SU(2)$ group, and $\vec{\alpha}$ is a spacetime dependent parameter.

Type	Form	Components	Boson spin
Scalar	$\bar{\psi}\phi$	1	0
Vector	$\bar{\psi}\gamma^5\phi$	4	1
Axial vector	$\bar{\psi}\gamma^\mu\gamma^5\phi$	4	1
Tensor	$\bar{\psi}(\gamma^\mu\gamma^\nu - \gamma^\nu\gamma^\mu)\phi$	6	2

Table 3: Allowed Lorentz-invariant bilinear covariant currents.[8]

The Lagrangian for the weak interaction then takes the form:

$$\mathcal{L} = \mathcal{L}_{Kin} + \mathcal{L}_{int}, \tag{18}$$

where $\mathcal{L}_{Kin}$ is the kinetic energy term, and the interaction term governs both the charged and neutral currents:

$$\mathcal{L}_{int} = \mathcal{L}_{CC} + \mathcal{L}_{NC}. \tag{19}$$

The charged current Lagrangian for one single family of leptons and quarks is:

$$\mathcal{L}_{CC} = -\frac{g}{\sqrt{2}} \left\{ \bar{u}\gamma^{\mu}(1-\gamma^{5})W_{\mu}^{+}d + \bar{\nu}\gamma^{\mu}(1-\gamma^{5})W_{\mu}^{+}e + h.c. \right\}, \tag{20}$$

where $W_{\mu}^{\pm} \equiv (W_{\mu}^{1} \mp iW_{\mu}^{2})/\sqrt{2}$ as a complex field refers to the field that gives rise to the charged vector boson W. The neutral current Lagrangian:

$$\mathcal{L}_{NC} = -\frac{g}{\cos\theta_W} \left\{ \frac{1}{2} \bar{\psi^{f}} \gamma^{\mu} (c_V^f - c_A^f \gamma^5) \psi^f Z_{\mu} \right\}, \tag{21}$$

includes a neutral Z boson; c_V^f and c_A^f are the vector and axial vector couplings of the fermion type f, and θ_W is the Weinberg angle, $\theta_W = 0.22290(30)$, given by

$$c_V^f = T_3^f - 2\sin^2\theta_w Q^f \tag{22}$$

$$c_A^f = T_3^f, \tag{23}$$

where T_3^f is the weak isospin of the fermion that relates to the electric charge with $Q = T_3 + \frac{1}{2}Y_W$, and Y_W is the weak hypercharge that is conserved in the electroweak group. Values of c_V and c_A are given in Table 4, for each type of quark and lepton.

	Q^f	c_V^f	c_A^f
ν	0	$\frac{1}{2}$	$\frac{1}{2}$
e	-1	$-\frac{1}{2} + 2\sin^2\theta_w$	$-\frac{1}{2}$
u	$\frac{2}{3}$	$\frac{1}{2} - \frac{4}{3}\sin^2\theta_w$	$\frac{1}{2}$
d	$-\frac{1}{3}$	$-\frac{1}{2} + \frac{2}{3}\sin^2\theta_w$	$-\frac{1}{2}$

Table 4: Vector and axial vector coupling of the first generation of fermions. Second and third generations have the same quantum numbers and thus the same couplings.

1.1.4.2 Spontaneous Symmetry Breaking: The Higgs Mechanism The $SU(2)_L$ theory with a particle spectrum of fermions and vector bosons is incomplete because it cannot account for the observed masses of either type of particle. Mass terms such as $\frac{1}{2}mA^\mu A_\mu$ are simply forbidden by the gauge invariance. Therefore, a scalar field is introduced into the model in order to give mass to the fermions: the Higgs field H.

The Higgs sector of the Lagrangian takes the form:

$$\mathcal{L}_H = (D^\mu\phi)^\dagger(D_\mu\phi) - V(\phi). \tag{24}$$

The standard model introduces the simplest possibility, namely an $SU(2)$ doublet of complex scalar fields, denoted as:

$$\phi(x) \equiv \begin{pmatrix} \phi^+(x) \\ \phi^0(x) \end{pmatrix}. \tag{25}$$

The covariant derivative contains all electroweak gauge fields, in other words the $SU(2)$ gauge fields with W_μ^a, $(a = 1, 2, 3)$, and $U(1)_Y$ gauge field with B_μ:

$$D_\mu\phi = (\partial_\mu + ig\frac{\tau^a}{2}W_\mu^a + ig'Y_W B_\mu)\phi. \tag{26}$$

Note that the $U(1)_Y$ group is precisely the same as that associated with an electric charge in QED, but in this context associated with the weak hypercharge Y_W. Renormalizability and the $SU(2)_L \otimes U(1)$ gauge invariance requires the scalar potential term to take the simplest form:

$$V(\phi) = \mu^2\phi^\dagger\phi + \lambda(\phi^\dagger\phi)^2. \tag{27}$$

If $\mu^2 > 0$, the minimum energy occurs at $\phi = 0$, which preserves the $SU(2)$ symmetry. However, if $\mu^2 < 0$, there is an infinite set of degenerate states satisfying the vacuum expectation value (VEV) condition:

$$\frac{\partial V}{\partial \phi} = 0 \Rightarrow \langle \phi \rangle \equiv \frac{1}{2} v^2, \tag{28}$$

where

$$v = \sqrt{\frac{-\mu^2}{\lambda}}. \tag{29}$$

One can parametrize the scalar doublet now in this general form:

$$\phi(x) = \exp\left[i \frac{\vec{\tau} \cdot \vec{\theta}}{2} \right] \frac{1}{\sqrt{2}} \begin{pmatrix} 0 \\ v + h(x) \end{pmatrix}. \tag{30}$$

Since the $U(1)$ symmetry is present, we have the freedom to choose the global phase $\vec{\theta}$ without loss of generality. Hence a unitary gauge transformation can be conducted:

$$\phi \to \exp\left[-i \frac{\vec{\tau} \cdot \vec{\theta}}{2} \right] \phi, \tag{31}$$

which simplifies the scalar field to be:

$$\phi(x) = \frac{1}{\sqrt{2}} \begin{pmatrix} 0 \\ v + h(x) \end{pmatrix}. \tag{32}$$

Symmetry is spontaneously broken by minimizing the potential energy in the field ϕ, which has now been rewritten in terms of deviation $h(x)$ from the minimum value v. We can summarize this process as:

$$SU(2)_L \times U(1)_Y \to U(1)_{QED}. \tag{33}$$

The gauge boson masses emerge from the broken symmetries. Substituting in the non-vanishing VEV v into the first term of (24) with (26), we can obtain:

$$\mathcal{L}_{mass} = \frac{1}{4} g^2 v^2 W^{+\mu} W^-_\mu + \frac{1}{8} v^2 (-g W^3_\mu + 2 g' Y_W B_\mu)^2, \tag{34}$$

and mass of the W and Z bosons appear in the Lagrangian. For the W boson we can read off directly from (34) $M_W = \frac{1}{2} g v$. A massive neutral Z boson emerges from a mixture of W^3 and B fields:

$$Z_\mu = \cos\theta_W W^3_\mu - \sin\theta_W B_\mu, \tag{35}$$

where θ_W is the previously defined Weinberg angle with the relation $\tan\theta_W = \frac{g'}{g}$. The Z boson mass is:

$$M_Z = M_W/\cos\theta_W = \frac{1}{2}\sqrt{(g^2+g'^2)}v \approx 91.2\text{MeV}. \tag{36}$$

1.1.4.3 The Yukawa Sector The final piece of the SM is the Yukawa sector, in which interactions between fermion and Higgs fields give rise to fermion masses and mixings. Such interactions are called Yukawa because they were originally inspired by Yukawa's theory of strong interactions.

The Yukawa Lagrangian for one single generation of fermions takes the form:

$$\mathcal{L}_{\text{Yukawa}} = \sum_{\ell}(Y_\ell \bar{L}_{\ell L}\phi\ell_R + h.c.) - \sum_{A,B}(Y^{(d)}_{AB}\bar{Q}_{AL}\phi d'_{BR} + Y^{(u)}_{AB}\bar{Q}_{AL}\tilde{\phi}u_{BR} + h.c.), \tag{37}$$

where Y stands for the Yukawa coupling (for corresponding leptons and quarks), L denotes a lepton doublet, l denotes a lepton singlet, q denotes a quark doublet, and u/d denotes a up/down-type quark singlet. ℓ and A, B stand for the three generations of leptons and quark flavors. In addition, $\tilde{\phi}$ represents a conjugate Higgs field, which takes the form:

$$\tilde{\phi} \equiv \begin{pmatrix} 0 & 1 \\ -1 & 0 \end{pmatrix}\begin{pmatrix} \phi^+ \\ \phi^0 \end{pmatrix} = \begin{pmatrix} \phi^{0*} \\ -\phi^- \end{pmatrix}. \tag{38}$$

The $\tilde{\phi}$ field is necessary in order to give the up-type quarks masses.

As with vector boson masses, the mass terms for leptons and quarks are generated through SSB. The Yukawa coupling matrices for quarks are not diagonal in the weak isospin basis, but may be diagonalized by a bi-unitary transformation: $M = U_L D U_R^\dagger$. This mixing of different generations is called the Cabibbo-Kobayashi-Maskawa (CKM) matrix. The CKM matrix can be written as

$$\begin{pmatrix} V_{ud} & V_{us} & V_{ub} \\ V_{cd} & V_{cs} & V_{cb} \\ V_{td} & V_{ts} & V_{tb} \end{pmatrix}, \tag{39}$$

which contains information about the strength of flavor-changing weak interactions. The matrix is unitary, and the overall phases of the quarks can be rotated freely. These conditions lead to 4 free parameters in the CKM matrix, when assuming three generations. A convenient parameterization

utilizes the Euler angles $(\theta_{12}, \theta_{13}, \theta_{23})$, plus one additional phase factor δ. With the notation $c_{ij} = \cos\theta_{ij}$ and $s_{ij} = \sin\theta_{ij}$, the CKM matrix can be expressed as:

$$V_{CKM} = \begin{pmatrix} c_{12}c_{13} & s_{12}c_{13} & s_{13}e^{-i\delta_{13}} \\ -s_{12}c_{23} - c_{12}s_{23}s_{13}e^{i\delta_{13}} & c_{12}c_{23} - s_{12}s_{23}s_{13}e^{i\delta_{13}} & s_{23}c_{13} \\ s_{12}s_{23} - c_{12}c_{23}s_{13}e^{i\delta_{13}} & -c_{12}s_{23} - s_{12}c_{23}s_{13}e^{i\delta_{13}} & c_{23}c_{13} \end{pmatrix} \tag{40}$$

in terms of the Wolfenstein paramertrization. The magnitude of the elements in the CKM matrix are determined by experimental results. The masses of the fermions therefore are given by:

$$m_f = \frac{h_f v}{\sqrt{2}}, \tag{41}$$

where the coupling constant h_f between the Higgs boson and the fermion is proportional to the fermion mass, and the Yukawa couplings are not predicted by the theory. It is worth noting that the top quark as the most massive fermion, has its Yukawa coupling being almost exactly unity.

1.2 Top Quark Physics

The top quark is a distinctive elementary particle characterized by its large mass – it is by far the heaviest elementary particle discovered in nature, with a mass that's approximately 40 times larger than the mass of the next heaviest quark, the bottom quark. Its lifetime is about 5×10^{-25}s, which is shorter than the typical hadronization time scale ($\simeq 3 \times 10^{-24}$s), making it the only quark that may be studied as a "bare" quark. Its mass is also close to the scale of electroweak symmetry breaking, which hints at a possible connection between the top quark and electroweak symmetry breaking.

At hadron colliders, the top quarks are produced predominantly in pairs ($t\bar{t}$) via the flavor-conserving strong interaction, but charged-current electroweak processes also produce a single top quark via a Wtb vertex. The large top-quark mass delayed its experimental discovery until 1995, at which time it was observed at the Tevatron proton-antiproton collider at Fermilab by both the CDF[9] and $D\emptyset$[10] experiments. The observation of the EW single top process was established even later – in 2009, 2.3 fb^{-1} and 3.2 fb^{-1} of data collected by the CDF and $D\emptyset$

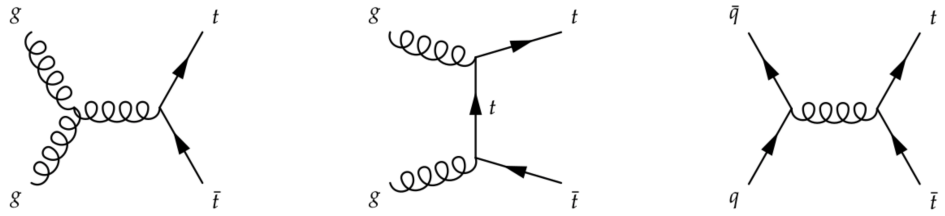

Figure 1: Feynman diagrams of $t\bar{t}$ production at leading order. The first two diagrams represent the production through gluon fusion, where the third one indicates quark-antiquark annihilation.

experiments. Nowadays, the high energy proton-proton collider – Large Hardon Collider (LHC) makes it possible to perform precision measurements on top quarks using both $t\bar{t}$ and single top channels. At the LHC@13TeV, the top-quark pair production has the largest cross section ($\sigma = 831.8$ pb@NNLO), while the single top t-channel production also possesses a sizeable cross section ($\sigma = 215$ pb@NNLO).

1.2.1 Single Top Production At The LHC

At the LHC, according to the SM, at leading order (LO) in perturbative quantum chromodynamics (pQCD), single top-quark production proceeds mostly in the following modes:

- **t-channel**: through the exchange of a virtual space-like W boson.
- **s-channel**: through the exchange of a virtual time-like W boson.
- **tW-associated**: where a single top quark is produced together with an on-shell W boson.

The t-channel has the highest production cross-section process at the LHC. The s-channel process is suppressed due to the parton distribution of the colliding protons — the antiquark in the initial state comes from the proton sea quarks, rather than proton valence quarks. Plus, the total center of mass energy of the process is high for LHC, which is disproportional to the matrix element of the s-channel process. More top quarks are produced at the LHC because of the prevalence of up quarks in the proton. The tW-associated process is kinematically suppressed due to the large mass requirement in the final state. The comparison of cross sections on different top processes at the

LHC is shown in Figure 3.

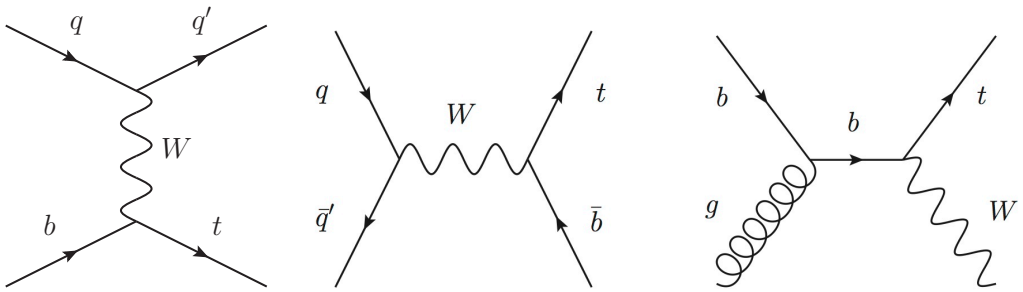

Figure 2: Representative LO Feynman diagrams for (from left to right) t-channel, s-channel, and tW single top-quark production.

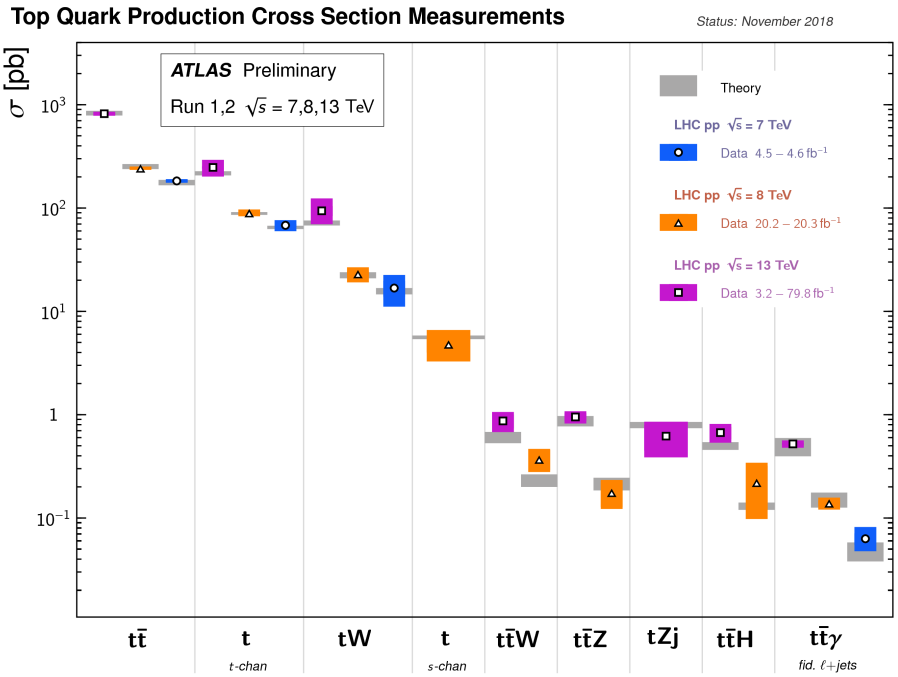

Figure 3: Summary of several top-quark related production cross section measurements, compared to the corresponding theoretical expectations. All theoretical expectations were calculated at NLO or higher. [11].

The electroweak t-channel single top quark production can be represented with a leading order Feynman diagram as shown in Figure 2(a), where a light quark is scattered from a bottom quark

(which is a sea quark produced by gluon splitting), producing a down quark (so-called "spectator quark") and a top quark in the final state. The SM predicts that the top quarks are highly polarized, due to the V-A coupling structure, along the direction of the momentum of the spectator quark, which recoils against the top quark[12]. At the LHC, two subprocesses contribute to the t-channel production of either single top quarks (t) or single top antiquarks ($\bar{t}$) at LO. The dominant subprocess is the scattering of an up- (down-)type quark from the beam from a bottom quark (antiquark), to produce a down- (up-)type spectator quark and a top quark (antiquark), as illustrated in Figure 4(a) and Figure 4(d). The subdominant subprocess is the scattering of a down- (up-)type antiquark from the beam from a bottom quark (antiquark), to produce an up- (down-)type spectator antiquark and a top quark (antiquark), as illustrated in Figure 4(b) and Figure 4(c). Thus, since the valence u-quark density of the proton is about twice as high as the valence d-quark density, the production cross-section of single top quarks is expected to be about twice as high as the cross-section of top-antiquark production.

1.2.2 Top Quark Polarization

Due to top's extremely short lifetime, the top quark decays before it hadronizes, passing its spin information to the decay products. An ensemble of top quarks is characterized by a spin-density matrix ρ which depends on the three-dimensional polarization vector, $P \equiv \{P_x, P_y, P_z\}$, where the ρ is:

$$\rho = \frac{1}{2}\begin{pmatrix} 1+P_z & P_x - iP_y \\ P_x + iP_y & 1-P_z \end{pmatrix}, \tag{42}$$

and the physical parameter space for a physical polarization is required to be $|\vec{P}| \leq 1$. ($|\vec{P}| = 1$) means the top quarks are produced in a pure spin state. At leading order, the top quark or anti-quark is 100% polarized along (against, in the case of top anti-quarks) the direction of the down-type quark. Depending on the subprocess, this is either the direction of the spectator quark, or the direction of the down-type quark donated by the beam (see Figure 4).

In the analysis presented in this thesis, we determine the components of the top quark polarization in the rest frame of the top quark, along three orthogonal directions. The first is taken to be the direction of the spectator quark. This is chosen because in the dominant subprocess for top production, or the subdominant anti-top production, the top or anti-top is 100% polarized along

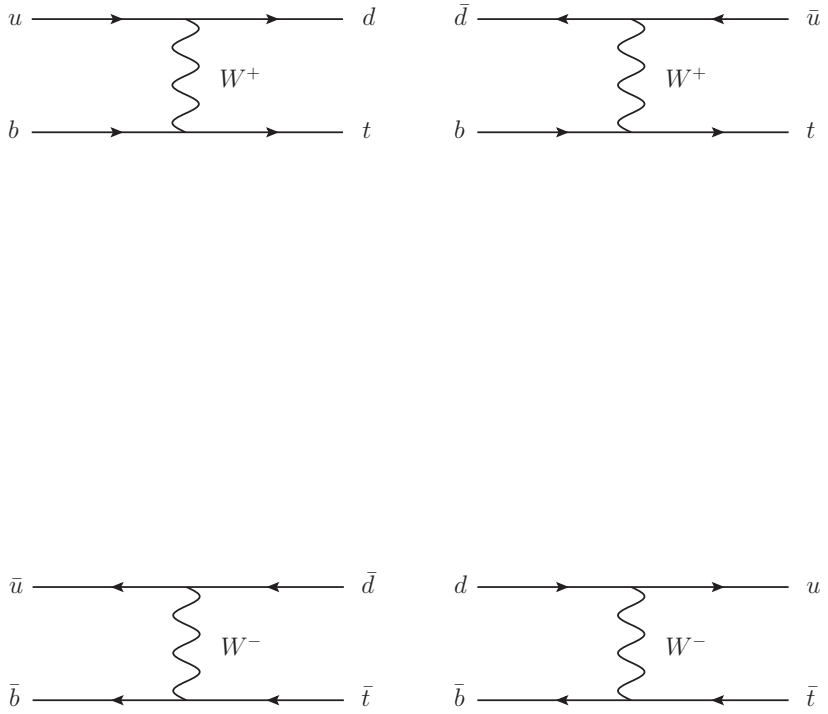

Figure 4: Subprocesses contributing to the t-channel production at LO. In the dominant subprocess, an up- or down-type quark from one of the colliding protons interacts with a b-quark or -antiquark from another proton by exchanging a virtual W boson to produce a top quark (upper-left) or top anti-quark (lower-right). In the subdominant subprocess, a down- or up-type anti-quark from one of the colliding protons interacts with a b-quark or -anti-quark from another proton by exchanging a virtual W boson to produce a top quark (upper-right) or top anti-quark (lower-left).

(or against) the direction of the spectator quark direction. Even when the polarization is along the beam direction, the kinematics of t-channel production ensure that the beam direction is nearly aligned with the direction of the spectator quark, particularly in the rest frame of the top quark. This is because the cross section of the t-channel production favors the phase space where little momentum transfer occurs, making the spectator quark extremely forward.

Two orthogonal axes are also defined, as shown in Figure 5. The spectator quark direction defines the z-axis, and lies in the production plane. The x-axis is orthogonal to the z-axis and also lies in the production plane. The y-axis is perpendicular to the production plane. Thus, the x-, y-, and z-axes form an orthonormal set. In terms of initial and final state particles in the top quark reference frame, these axes are defined by

$$\hat{z} = \frac{\vec{p}_s}{|\vec{p}_s|}\,, \qquad \hat{y} = \frac{\hat{z} \times \vec{p}_q}{|\hat{z} \times \vec{p}_q|}\,, \qquad \hat{x} = \hat{y} \times \hat{z}\,. \tag{43}$$

The $\hat{z}$ direction is the direction of the momentum of the spectator quark, $\vec{p}_s$, in the top-quark reference frame. The $\hat{y}$ direction taken like along $\hat{z} \times \hat{p}_q$, where $\vec{p}_q$ is the direction of the incoming light quark, in the top-quark reference frame. Finally, the $\hat{x}$ direction lies in the plane of production, orthogonal to $\hat{y}$ and $\hat{z}$. Figure 5 illustrates these axes in the Zero Momentum Frame (ZMF).

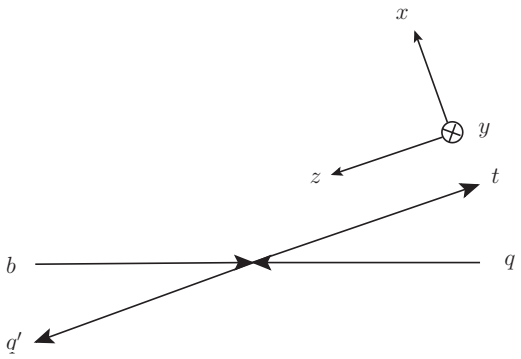

Figure 5: Diagram illustrating the three directions $\hat{x}$, $\hat{y}$ and $\hat{z}$ used in this analysis, as seen in the zero-momentum frame. The $\hat{z}$ direction is that of the spectator quark in the top-quark rest frame. The $\hat{x}$ direction lies in the plane of production, while the $\hat{y}$ direction is perpendicular to the plane of production.

We can parameterize the decay distribution in terms of the cosine of decay angles in a linear form:

$$\frac{1}{\Gamma}\frac{d\Gamma}{d\cos\theta_{ji}} = \frac{1}{2}(1+\alpha_j P_i \cos\theta_{ji})\,, \tag{44}$$

where $i = x, y, z, \theta_{Xi}$ is the angle between particle X and axis i, α_X is the spin analyzing power associated with particle X, and P_i is the top-quark degree of polarization in a given direction Y. In the SM, the charged lepton from W-boson decay is the best spin analyzer, with $\alpha_\ell = 1$ exactly calculated at tree level. All other potential analyzers (semileptonic W decay only) are quoted in Table 5. While it might be surprising that the charged lepton is a better analyzer than its mother, the W boson, this is due to the constructive (parallel direction to $\vec{s}_t$) and destructive (opposite direction to $\vec{s}_t$) interference of the two spin states ($\lambda_W = 0, -1$) of the W boson.

Decay Product	α_i
b	-0.40
ν_ℓ	-0.33
$\bar{\ell}$	1.00

Table 5: Correlation coefficients α_i for semileptonic top quark decays. The first two entries are a function of M_t^2/M_W^2 , and have been evaluated for M_t = 173.8 GeV and M_W = 80.41 GeV. [13]

Higher-order effects have been studied to modify the polarization. For instance, the spin axis definition becomes ambiguous when an extra gluon enters the picture. Beyond-Standard-Model (BSM) effects, such as top anomalous couplings and four-fermion operators, may also manifest themselves by altering the polarization. As Figure 6 shows, the P_y component of polarization is sensitive to the imaginary part of the anomalous coupling g_R[14]. Furthermore, comparison between cross-section and polarization measurements was also studied with regard to their sensitivities towards these BSM effects in Ref[15][16]. Demonstrated in Figure 7, polarization measurements were shown to hold a considerable advantage over the cross-section measurement in order to hunt for new physics such as extracting effective four-fermion coefficients[16].

The ATLAS and CMS both adopted these aforementioned definitions, and published measurements on the polarization of combined top quark/anti-quark data collected at $\sqrt{s} = 8$ TeV in the

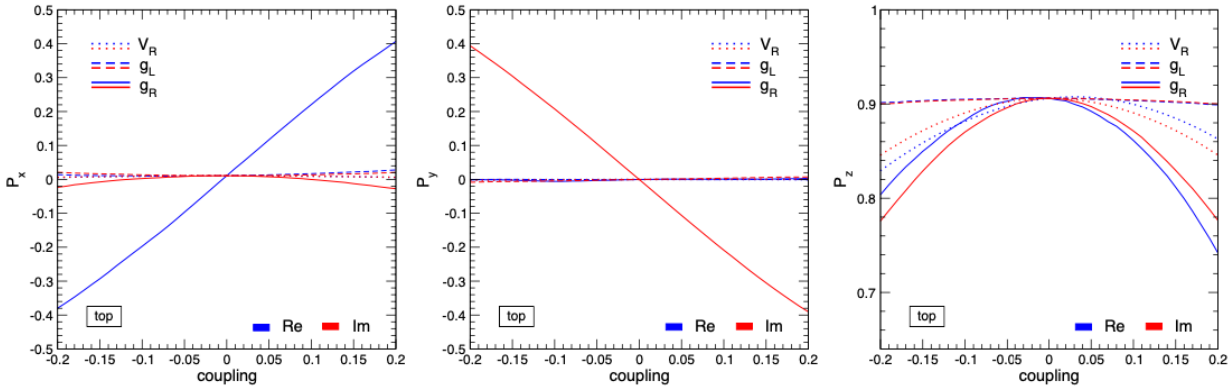

Figure 6: Displaying how the anomalous couplings affect the single top polarization with respect to the three orthogonal axes. Strong linear dependence is expected from the g_R Wtb coupling.

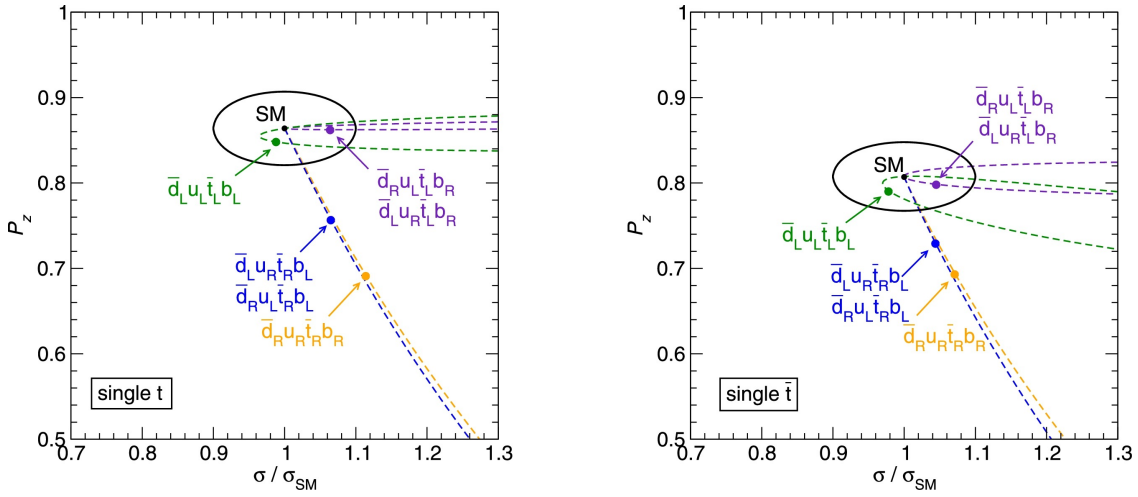

Figure 7: Effect of four-fermion contributions in the single top cross section (normalized to the SM value) and polarization, for top quarks (left) and anti-quarks (right). The black dots and ellipses represent the SM predictions and expected uncertainties. The points corresponding to operator coefficients $C/\Lambda^2 = 1\text{TeV}^{-2}$ are indicated.

single top t-channel. Measured by the unfolding technique, the ATLAS collaboration extracted the polarization along the $\hat{z}$-axis $P_z(t+\bar{t}) = 0.98 \pm 0.12$[17] and $P_z(t+\bar{t}) > 0.86(68\%C.L.)$[18],

which are consistent with the SM prediction of $P \approx 0.9$ shown in [12][19][20], while the CMS collaboration reported the result of $P_z(t+\bar{t}) = 0.56 \pm 0.24$[21]. At $\sqrt{s} = 13$ TeV, the expected values at LO of the polarization of top quarks and anti-quarks are:

$$\begin{aligned} P^t &= (0.0, 0.0, +0.90)\,, \\ P^{\bar{t}} &= (-0.14, 0.0, -0.86)\,, \end{aligned} \tag{45}$$

computed in the four-flavor scheme in [14]. These polarization values in fiducial region will be altered by the event selection criteria (which limit the reference sample to events containing top quarks with higher velocity in the ZMF); these happen to have a higher degree of polarization.

1.2.3 The Fully Differential Top Decay Distribution

As mentioned above, we can determine the top spin through its decay angular distributions. According to the Jacob and Wick helicity formalism[22], the amplitude of a two-body decay takes the form[23]:

$$A(a \to f) = \left[\frac{2J+1}{4\pi}\right]^{\frac{1}{2}} D^{J*}_{M,\lambda}(\phi, \theta, -\phi) A_{\lambda_1,\lambda_2}\,, \tag{46}$$

where λ_1 and λ_2 are the helicities of the outgoing particles and $\lambda = \lambda_1 - \lambda_2$, J and M are the spin and helicity of the decaying particle, $D^J_{M,\lambda}$ is the Wigner D-function, and the angles are defined in the rest frame of the decaying particle. A_{λ_1,λ_2} is the amplitude for the decay to the specified helicity states. For the entire top decay process, where there occurs two-body decays two times in total, $t \to Wb \to l\nu$, we will have the following amplitudes[24]:

$$A_{M\lambda_2\lambda_3\lambda_4} = \sum_{\lambda_1} a_{\lambda_1\lambda_2} b_{\lambda_3\lambda_4} D^{1/2*}_{M\Lambda}(\phi, \theta, 0) D^{1*}_{\lambda_1\lambda}(\phi^*, \theta^*, 0), \tag{47}$$

where $\lambda_1, \lambda_2, \lambda_3, \lambda_4$ are the helicities of the W boson, b quark, charged lepton and neutrino, respectively; M is the third spin component of the top quark, and $\Lambda = \lambda_1 - \lambda_2$, $\lambda = \lambda_3 - \lambda_4$; D is the Wigner D-function, and $a_{\lambda_1\lambda_2}, b_{\lambda_3\lambda_4}$ are constants. In top quark decay, there are only four non-zero reduced amplitudes $a_{1\,\frac{1}{2}}$, $a_{0\,\frac{1}{2}}$, $a_{0\,-\frac{1}{2}}$, $a_{-1\,-\frac{1}{2}}$. For $W^{\pm}$ decays, assuming massless charged leptons, $\lambda_3 = \pm\frac{1}{2}$, $\lambda_4 = \mp\frac{1}{2}$. In addition, $\lambda = 1$ for top quarks, $\lambda = -1$ for top anti-quarks. Incorporating

the spin density matrix introduced in Eq. (42), we can write down the normalized semi-leptonic differential decay width of the top quark in terms of four angles:

$$\frac{1}{\Gamma}\frac{d\Gamma}{d\Omega d\Omega^*} = \frac{3}{8\pi^2}\frac{1}{\mathcal{N}} \sum_{MM'\lambda_1\lambda_1'\lambda_2} \rho_{MM'} a_{\lambda_1\lambda_2} a^*_{\lambda_1'\lambda_2} D^{\frac{1}{2}*}_{M\Lambda}(\phi,\theta,0) D^{\frac{1}{2}}_{M'\Lambda'}(\phi,\theta,0) \times D^{1*}_{\lambda_1\lambda}(\phi^*,\theta^*,0) D^{1}_{\lambda_1'\lambda}(\phi^*,\theta^*,0), \tag{48}$$

where $d\Omega = d\phi d\cos\theta$ is the so-called solid angle, θ and ϕ are the polar and azimuthal angles of the W boson in the coordinate system previously defined in Section 1.2.2, and θ^*, ϕ^* are the polar and azimuthal angles of the lepton in the W-boson rest frame (the azimuth being given by the W-direction in the top quark rest frame), and $\Gamma = \lambda_1 - \lambda_2$, and $\mathcal{N} = |a_{1\,\frac{1}{2}}|^2 + |a_{0\,\frac{1}{2}}|^2 + |a_{0\,-\frac{1}{2}}|^2$. We can use the explicit expressions for the D-functions, and apply the physical parameters, then we arrive to this compact form:

$$\begin{aligned}
\frac{1}{\Gamma}\frac{d\Gamma}{d\Omega d\Omega^*} = \frac{3}{64\pi^3}\frac{1}{\mathcal{N}}\{&[|a_{1\,\frac{1}{2}}|^2(1+\lambda\cos\theta^*)^2 + 2|a_{0\,-\frac{1}{2}}|^2\sin^2\theta^*](1+\overrightarrow{P}\cdot\overrightarrow{u_L})\} \\
&+ [2|a_{0\,\frac{1}{2}}|^2\sin^2\theta^* + |a_{-1\,-\frac{1}{2}}|^2(1-\lambda\cos\theta^*)^2](1-\overrightarrow{P}\cdot\overrightarrow{u_L}) \\
&+ \lambda\, 2\sqrt{2}[\Re(a_{0\,\frac{1}{2}}a^*_{1\,\frac{1}{2}}e^{-i\phi^*})(1+\lambda\cos\theta^*) \\
&+ \Re(a_{-1\,-\frac{1}{2}}a^*_{0\,-\frac{1}{2}}e^{-i\phi^*})(1-\lambda\cos\theta^*)]\sin\theta^*\overrightarrow{P}\cdot\overrightarrow{u_T} \\
&+ \lambda\, 2\sqrt{2}[\Im(a_{0\,\frac{1}{2}}a^*_{1\,\frac{1}{2}}e^{-i\phi^*})(1+\lambda\cos\theta^*) \\
&+ \Im(a_{-1\,-\frac{1}{2}}a^*_{0\,-\frac{1}{2}}e^{-i\phi^*})(1-\lambda\cos\theta^*)]\sin\theta^*\overrightarrow{P}\cdot\overrightarrow{u_N}\}\,,
\end{aligned} \tag{49}$$

where Γ is the total decay width of the top quark, the coefficients a_{λ_w,λ_b} are the trainsition amplitudes for the decay $t \to Wb$, where λ_W and λ_b are the helicities of the W boson and the b quark, respectively. $\vec{u}_L = (\sin\theta\cos\phi, \sin\theta\sin\phi, \cos\theta)$ is the unit vector in the direction of the W boson momentum in the top quark rest frame, and $\vec{u}_T = (\cos\theta\cos\phi, \cos\theta\sin\phi, -\sin\theta)$, $\vec{u}_N = (\sin\phi, -\cos\phi, 0)$ are two ortho-normal vectors. $\vec{P}$ represents the polarization vector. This expression can be used as the basis for a decay model, executing during event generation to simulate top quark decay with arbitrary polarization.

The fully differential decay rate for any ensemble of polarised top (anti)quarks given by Eq. (49) can be written in terms of two wave-functions $\psi_j(\theta,\phi,\theta^*,\phi^*)$, one for each polarisation state along z, where $j \in \{+,-\}$, together with a 2×2 spin-density matrix ρ, describing the spin content of the ensemble, as follows

$$\begin{aligned}\frac{1}{\Gamma}\frac{d\Gamma}{d\Omega d\Omega^*} &= \sum_j\sum_k \rho_{jk}\psi_j\psi_k^* \equiv \frac{1+P_z}{2}\psi_+\psi_+^* + \frac{1-P_z}{2}\psi_-\psi_-^* \\ &+ \frac{P_x}{2}(\psi_+\psi_-^* + \psi_-\psi_+^*) + \frac{P_y}{2i}(\psi_+\psi_-^* - \psi_-\psi_+^*)\,, \end{aligned} \tag{50}$$

where j and k represent the top-quark polarisation state along $\hat{z}$. Thus the fully differential decay rate is a linear combination of four functions,

$$\frac{1}{\Gamma}\frac{d\Gamma}{d\Omega d\Omega^*} = \frac{1+P_z}{2}\mathcal{F}_{z+} + \frac{1-P_z}{2}\mathcal{F}_{z-} + \frac{P_x}{2}\mathcal{F}_x + \frac{P_y}{2i}\mathcal{F}_y\,, \tag{51}$$

where

$$\begin{aligned}\mathcal{F}_{z+}(\theta,\phi,\theta^*,\phi^*) &\equiv \psi_+\psi_+^* \\ \mathcal{F}_{z-}(\theta,\phi,\theta^*,\phi^*) &\equiv \psi_-\psi_-^* \\ \mathcal{F}_x(\theta,\phi,\theta^*,\phi^*) &\equiv (\psi_+\psi_-^* + \psi_-\psi_+^*) \\ \mathcal{F}_y(\theta,\phi,\theta^*,\phi^*) &\equiv -i(\psi_+\psi_-^* - \psi_-\psi_+^*)\,. \end{aligned}$$

Monte Carlo (MC) generation of t-channel events, configured to produce pure polarization states, can be used to obtained templates for these four functions (or their projections). Moreover, if the generation is followed by detector simulation and reconstruction, the templates for the joint probability distribution *including detector effects*, or their projections, can be obtained. These can then be used in a template fit to real data, in which the three components of polarization, P_x, P_y, P_z are allowed to float. This allows us to measure the spin-density matrix. Analytic expressions for the fully differential decay rate are not required during the actual fit; instead they are the basis of a decay model employed during MC generator in order to obtain the templates.

2.0 The ATLAS Experiment At The Large Hadron Collider

The LHC is the largest particle collider that has ever been built, and the ATLAS detector is the largest volume detector ever constructed for a particle collider.

2.1 The Large Hadron Collider

2.1.1 Overview of The Machine

The Large Hadron Collider (LHC)[26] is the state-of-the-art hadron accelerator and collider located in an area between Geneva, Switzerland and France. Its two rings span a circumference of 26.7km, and are divided into eight arcs and eight insertion regions (IRs), and lay between 45m and 170m under the surface of the Jura mountains. There are also two transfer tunnels, approximately 2.5 km long each, acting as injectors. In total 1,232 superconducting dipole magnets are accommodated in the LHC rings, with 1,104 in the arc and 128 in the Dispersion Suppressor (DS) region. In order to bend the trajectories of protons with energy as high as 7 TeV, they operate at a temperature below 2 K, use superfluid helium for cooling and generate fields above 8 T. The magnets use niobium-titaniun (NbTi) cables, and carry a 11,850 A current. Due to the space limitation in the LHC tunnels and cost concerns, a "two-in-one" or "twin-bore" design is adopted for almost all of the LHC superconducting magnets so that the cryostat and cold mass are shared between the two beam channels. Their main components are shown in Figure 9.

The nominal center-of-mass energy for the LHC is 14 TeV. In order to achieve that energy, the protons are first accelerated in the injector chain: Linac2 — Proton Synchrontron Booster (PSB) — Proton Synchrotron (PS) — Super Proton Synchrotron (SPS), before finally entering the LHC for further acceleration. Linac2 is a linear accelerator that is used to make protons by stripping electrons off Hydrogen atoms, and accelerating them to 50 MeV. Then, the protons enter PSB where they are accelerated to an energy of 1.4 GeV. Afterwards, the PS continue to accelerate the protons to 25 GeV, and arranges them into bunches. The last step before injection is the SPS,

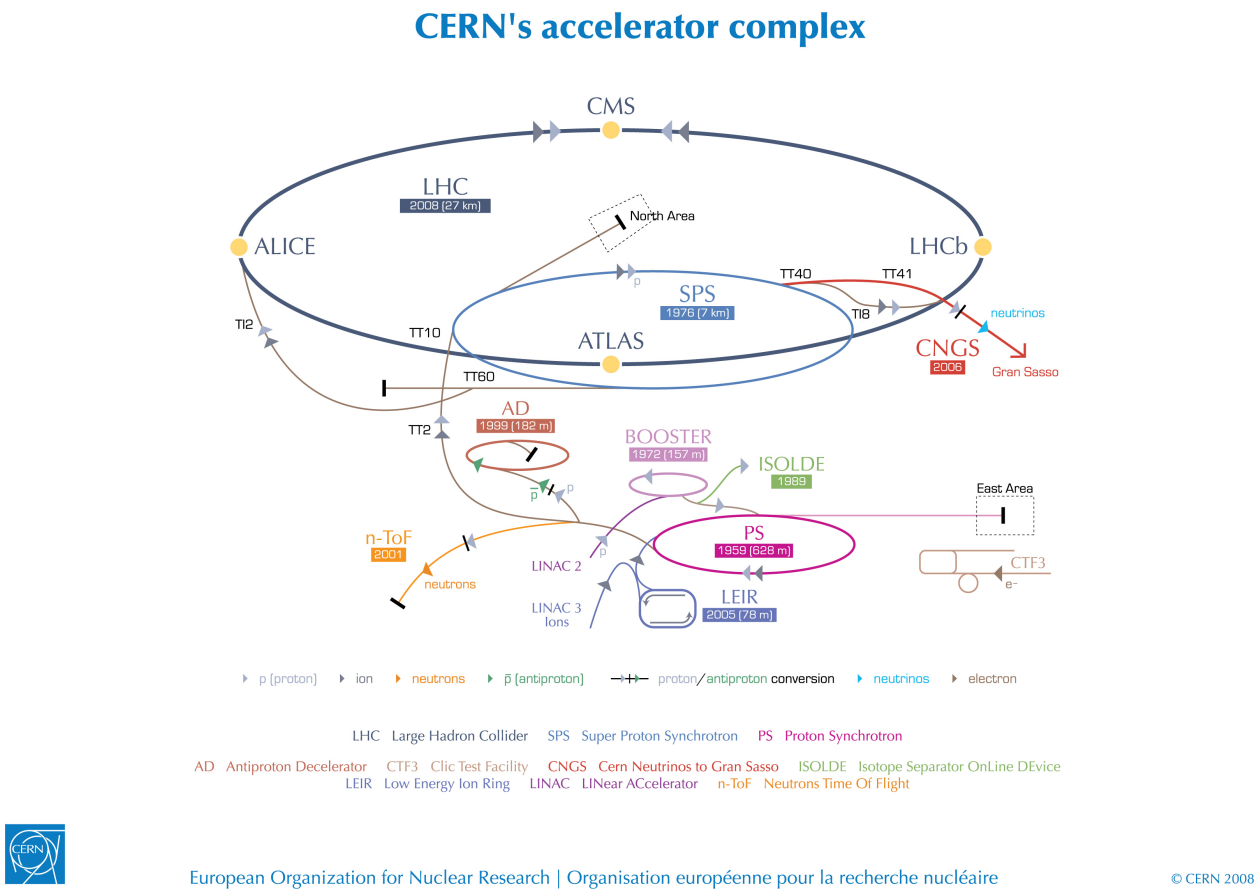

Figure 8: Schematic layout of the accelerator complex at CERN. The LHC is the last ring (dark grey line) in this complex chain of particle accelerators, and the smaller machines are used in a chain to help boost the particles to their final energy. [25]

where the protons are accelerated to 450 GeV, before transferring to the LHC. The proton beams in the LHC are grouped into 2808 circulating bunches in each ring, with about 1.15×10^{-11} protons per bunch. The two beams will collide at every "bunch crossing" at four points, shown as yellow points in Figure 8, with a peak collision rate of 40 MHz. The bunches are not continuous in the rings however: every 72 bunches are separated by 25 ns and bundled into a "bunch train", and each bunch train is separated by 12 empty bunches. The design of this layout is driven by experimental limitations such as the enhanced electron cloud negatively affect the beam, cryogenics and vacuum.

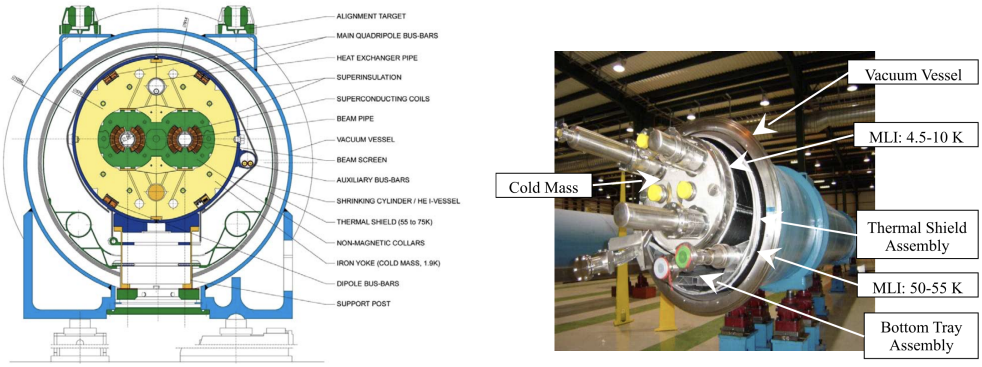

Figure 9: Detailed anatomy of a dipole magnet. The left plot displays the cross section of the magnet, while the right one displays the assembly.[25]

2.1.2 Performance Goals and Operation

The LHC aims to test the SM with an unprecedented precision and search for physics beyond the SM. The number of events per second generated in the LHC is given by:

$$N_{event} = L\sigma_{event}, \tag{52}$$

where σ_{event} is the cross section for the type of event and L is the instantaneous luminosity. The quantity L depends on the beam parameters and under the assumption of a Gaussian beam profile, it can be written as:

$$L = \frac{N_b^2 n_b f_{rev} \gamma_r}{4\pi\epsilon_n \beta^*} F, \tag{53}$$

where N_b is the number of particles per bunch, n_b is the number of bunches per beam, f_{rev} is the revolution frequency, γ_r is the relativistic gamma factor, ϵ_n the normalized transverse beam emittance, β^* is the beta function at the collision point, and F is the geometric luminosity reduction factor due to the crossing angle at the interaction point (IP):

$$F = \left(1 + \left(\frac{\theta_c \sigma_z}{2\sigma^*}\right)^2\right)^{-\frac{1}{2}}, \tag{54}$$

where θ_c is the full crossing angle at the IP, σ_z is the RMS bunch length, and σ^* is the transverse RMS beam size at the IP. We assume $\sigma_z \ll \beta$ and equal beam parameters for both beams. There are

two high luminosity experiments at the LHC: ATLAS[27] and CMS[28], both are general purpose detectors designed for a luminosity $L = 10^{34}\,\mathrm{cm}^{-2}\mathrm{s}^{-1}$. In addition there are two low luminosity experiments: LHCb [29], designed for B-physics at $L = 10^{32}\,\mathrm{cm}^{-2}\mathrm{s}^{-1}$ and TOTEM[30], designed for elastic and diffractive cross-section measurements at $L = 2 \times 10^{29}\,\mathrm{cm}^{-2}\mathrm{s}^{-1}$ with 156 bunches. While proton-proton collisions occupy most of LHC's operation, there are ion beams as well, usually scheduled near the end of the year. The LHC has one dedicated heavy ion experiment, ALICE[31], which aims at a peak luminosity of $L = 10^{27}\,\mathrm{cm}^{-2}\mathrm{s}^{-1}$ of nominal lead-lead ion operation.

Since the beginning of its operation in 2009, the LHC has completed two runs. During Run 1 (2009 - 2012), the LHC went from a center-of-mass energy of 900 GeV to 7 TeV in 2010, and then eventually reached 8 TeV in 2012. A total integrated luminosity of 22.8 fb^{-1} at $\sqrt{s} = 8\mathrm{TeV}$ was delivered to ATLAS during run 1. Then, after a long shutdown, Run 2 started in 2015 at $\sqrt{s} = 13\mathrm{TeV}$, and saw a gradual increase of integrated luminosity every year. By the end of Run 2 in 2019, a total of 156 fb^{-1} of proton-proton collision data was delivered by the LHC. The cumulative luminosity delivered to ATLAS versus time is shown in Figure 10.

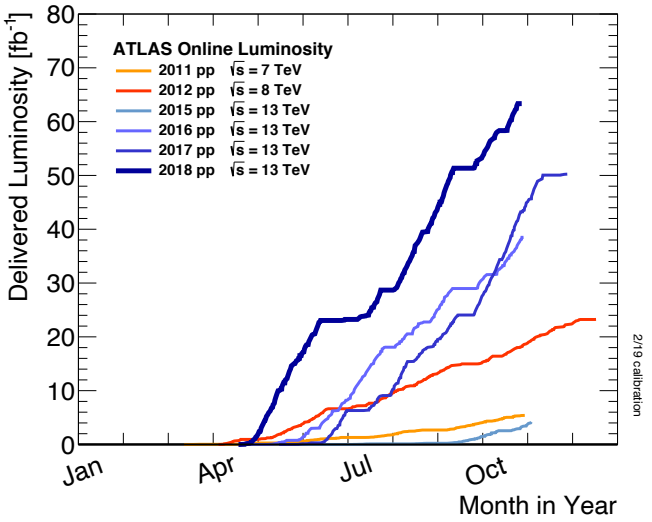

Figure 10: Delivered luminosity versus time for 2011-2018 (p-p data only). [32]

2.2 The ATLAS Detector

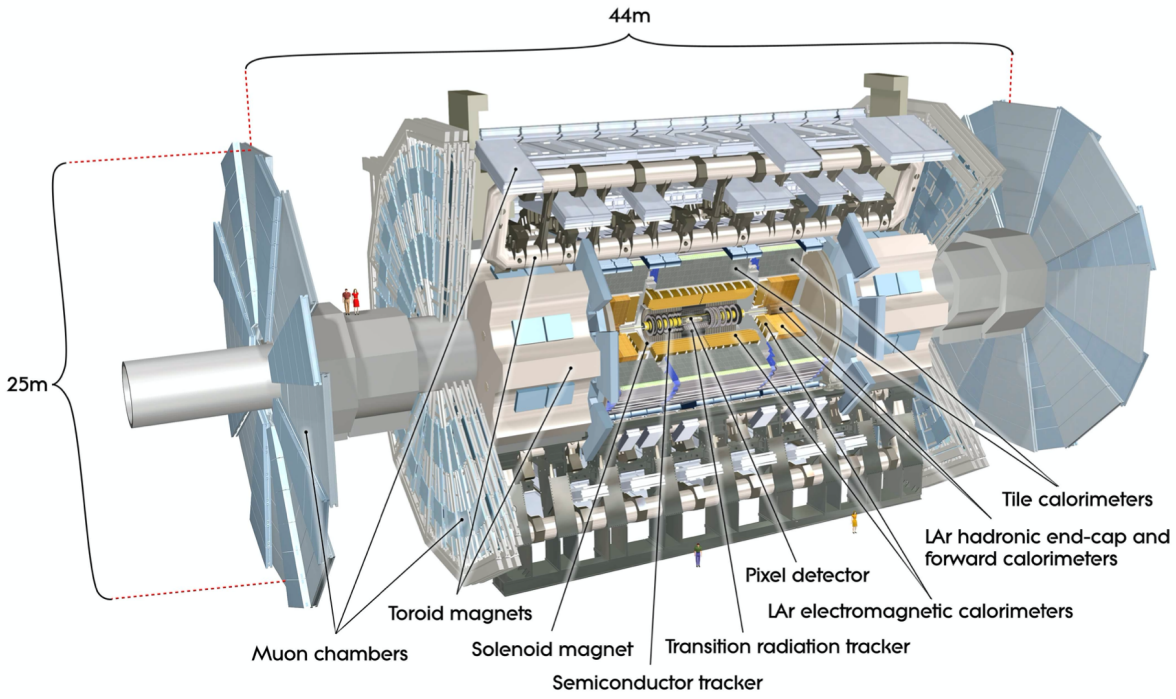

Figure 11: Cut-away view of the ATLAS detector. The dimensions of the detector are 25 m in height and 44 m in length. The overall weight of the detector is approximately 7,000 tonnes. [27]

The ATLAS (A Toroidal LHC Apparatus) detector, and the CMS (Compact Muon Solenoid) detector, are the two general purpose detectors at the LHC. Their scientific goals are the same — both built for investigating a wide range of physics, and collecting data from proton-proton and heavy ion collisions. The technical solutions and magnet designs of the two detectors however, are different. More specifically, the detectors are designed for:

- **The SM Higgs boson**: The Higgs Boson is the last piece of the puzzle in the SM. Its discovery was a major criteria for the design of the detector, and a top priority for the experiment. For a lighter Higgs ($m_H < 2m_Z$), its natural width is only a few MeV, so that fine instrumental resolution is required. In terms of data analysis, $H \rightarrow \gamma\gamma$ is the most promising channel due to high QCD backgrounds. For a heavier Higgs, $H \rightarrow ZZ^* \rightarrow l^-l^+l^-l^+$ is another important channel. Therefore, precision tracking, calorimetry and muon momentum resolution

are required for good Higgs boson mass resolution.

- **Top quark physics**: The high luminosity and center-of-mass energy at the LHC enables high precision measurements of QCD, electroweak interactions, and flavour physics. The top quark is produced at the LHC at a rate of a few tens of Hz, mostly through top-pair production and the single-top production channels. The LHC is often called "a top factory". The unprecedented statistics will allow more sophisticated tests of top quark's properties such as couplings and spin.
- **Supersymmetry(SUSY)**: The decays of hypothetical SUSY particles such as squarks and gluinos leads to a Lightest Stable supersymmetric Particle (LSP) in the final state. Because of LSP's weak coupling to the detector, a substantial amount of missing transverse energy P_T^{miss} is present. Good resolution on the measurement of E_T^{miss} is required in order to improve limits on SUSY from previous experiment, or to discover SUSY particles.

In order to accommodate this ambitious list, the ATLAS detector was equipped with cutting-edge technologies including ultrafast, radiation-hard electronics, sophisticated cryogenic systems for the superconducting magnets and Liquid Argon (LAr) calorimeter, and first-class mechanical engineering to withstand the immense Lorentz forces generated by the magnets. As shown in Figure 11, the ATLAS detector is 46 meters long and 25 meters in diameter, weighing 7,000 tonnes in total, and placed 100 meters under the ground. The four major components of the ATLAS detector are the Magnet System, the Inner Detector, the Calorimeter, and the Muon Spectrometer. Off-detector components include: the Trigger and Data Acquisition (TDAC) System, a multi-level computing system designed to select physics events with desired physical signatures with low latency; and the Computing System, processes and analyzes the collected collision data across 130 computing centres worldwide.

2.2.1 The Coordinate System

The ATLAS detector is cylindrically symmetric. Its coordinate system has its origin at the nominal interaction point (the bottom yellow dot labelled "ATLAS" in Figure 8), and therefore the detector is forward-backward symmetric with respect to the interaction point. The z-axis is defined along the beam direction, and the $x-y$ plane is transverse to the beam direction, as shown

in Figure 12. For convenience the side with the $+z$-axis is referred to as side-A, where the other side is labelled as side-C . The $+x$ direction is chosen to be pointing inwards from the interaction point to the centre of the LHC ring and the $+y$-axis is defined as pointing upwards. The angles are defined as usual in a cylindrical coordinates, where the azimuthal angle ϕ defined in the transverse plane, and the polar angle θ is the angle measured from the beam axis. The rapidity y is defined as:

$$y = \frac{1}{2} \ln \left[\frac{E + p_z}{E - p_z} \right]. \tag{55}$$

In the ultra-relativistic limit, which is the case for most particles in the LHC, the pseudorapidity, defined as:

$$\eta = -\ln \tan(\theta/2), \tag{56}$$

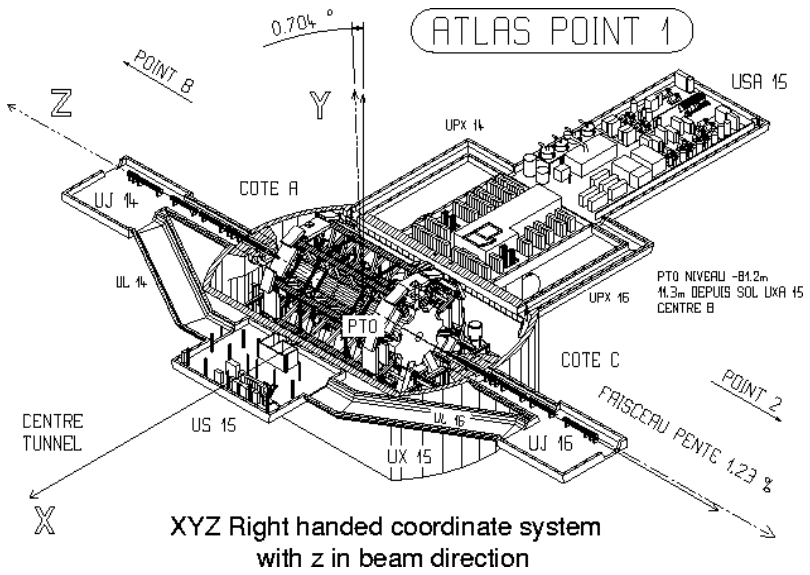

Figure 12: The coordinate system in the ATLAS detector. The general tilt of the LEP/LHC tunnel causes the y-axis to be slightly different from vertical. [27]

where θ is the polar angle is a good approximation to the rapidity. Another commonly used quantity ΔR — the distance (or sometimes called "the separation") in the space of (η, ϕ), is defined as:

$$\Delta R = \sqrt{\Delta\eta^2 + \Delta\phi^2}. \tag{57}$$

2.2.2 The Magnet System

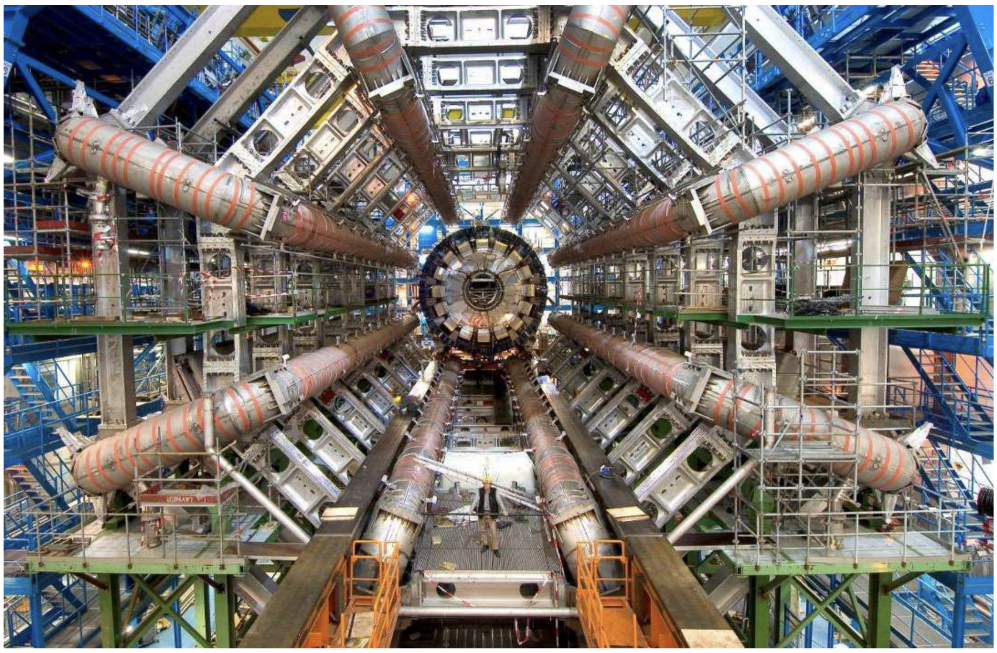

Figure 13: The Barrel toroid of the Magnet System as installed in the underground cavern. Note the symmetry of the structure and its size compared to the person standing in the picture.[27]

The Magnet System is 22 meters in diameter, and 26 meters long, with a stored energy of 1.6 GJ. It consists of: 1) a solenoid, which is aligned on the beam axis and provides a 2 T axial magnetic field for the inner detector, and 2) three toroids, consisting of one barrel and two end-cap toroids, producing a magnetic field of 0.5 T and 1 T for the muon detectors, respectively. The solenoid generates a magnetic field along the z-axis, bending any charged particle (such as the l^+ from top decay) in the transverse plane (ϕ-direction); on the other hand, the toroids generate an azimuthal magnetic field, and bend charged particles in the η-direction.

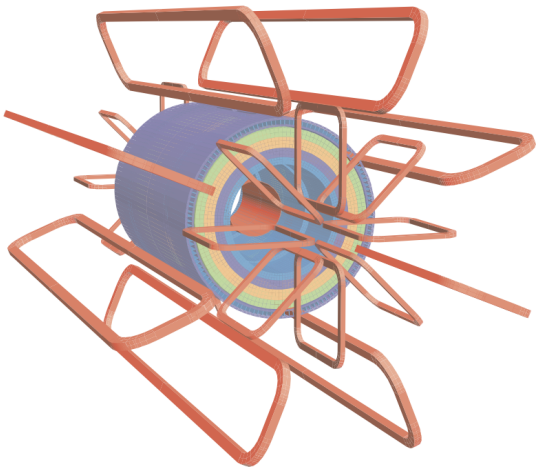

Figure 14: A sketch of the full Magnet System of the ATLAS detector. The forward shield disk is not displayed for the sake of clarity. [27]

2.2.3 The Inner Detector

The Inner Detector is the innermost part of the ATLAS detector. The main components of the Inner Detectors are the Pixel Detector, the Semiconductor Tracker (SCT), and the Transition Radiation Tracker (TRT). The layout of these components is illustrated in Figure 15. The Inner Detector provides accurate pattern recognition, momentum resolution, and primary and secondary vertex measurements for charged tracks with much higher energy (nominally a p_T threshold of 0.5 GeV). Electron identification is also provided by the TRT within the range of $|\eta| < 2.0$ and between 0.5 GeV - 150 GeV.

The outer radius of the tracking volume is 115cm, and the total length is 7 meters, and is limited by the solenoid and the calorimeter system. The inner detector contains a barrel part that extends ± 80 cm around the origin, and two identical end-caps covering the rest of the cylindrical cavity.

2.2.3.1 The Pixel Detector The Pixel Detector is a precision tracker that is highly sensitive, compact and which provides a very high granularity. As shown in Figure 15 (b), the Pixel Detector consists of three cylindrical layers in the barrel region, and three pixel disks in each end-cap region.

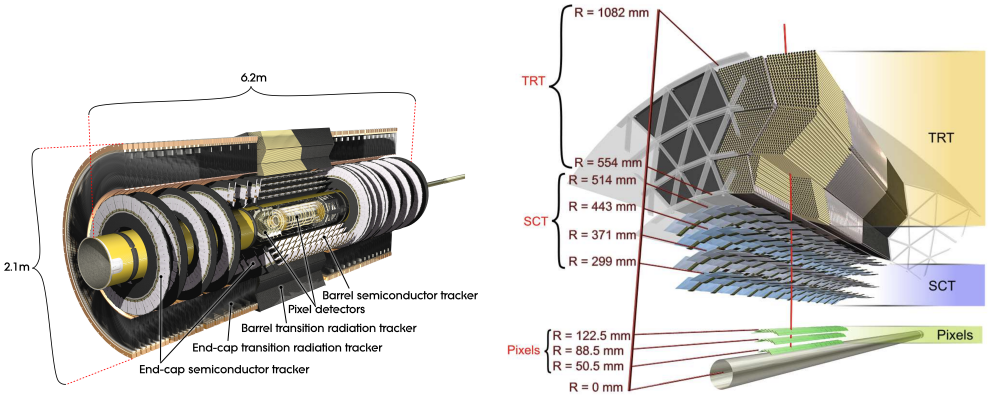

Figure 15: Detailed drawings of the Inner Detector. The left plot displays a cutaway view showing components along the beam axis. The right plot displays a cutaway view showing detailed sensors, straw tubes and support structures. Also shown is a charged track of 10 GeV transverse momentum in the barrel inner detector ($\eta = 0.3$). [27]

The B-layer, which is the innermost layer (at $R = 50.5\,mm$), is crucial in detecting secondary vertices in order to identify b-jets. B-jet identification is crucial for the reconstruction of the top quark events because the top quark decays nearly 100% of the time into a b-quark. Overall the Pixel Detector contains 80 million pixels (channels) in total, covering the full acceptance around the interaction point. Each pixel size is $50 \times 400\,\mu m^2$, with a resolution of $14 \times 115\,\mu m^2$. This enables the Pixel Detector to rapidly capture and distinguish radiations from charged particles, giving it the ability to precisely measure the impact parameter of short-lived particles such as b-quarks and τ-leptons [33]. Advanced readout technologies are employed to achieve the required high density of connections, as well as radiation resistance to over 300 kGy of ionising radiation and over 5×10^{14} neutrons per cm^2 in ten years of operation.

2.2.3.2 The Semiconductor Tracker (SCT) The SCT is a silicon microstrip tracker, also consisting of a barrel and two end-caps. Four layers of silicon microstrip detectors are installed in the barrel region, and nine disks are installed in the end-cap region. Each module contains two layers of specially doped silicon chips, and readout strips for every $80\,\mu m$ on the silicon to provide a

spatial resolution of 17 μm for charged particle tracks. Charged particles passing through the SCT modules create electron-hole pairs, which drift in the electric field and generate a current that is digitized by the readout electronics. The position information generated by these signals is used in the reconstruction of charged tracks.

2.2.3.3 The Transition Radiation Tracker

The Transition Radiation Tracker (TRT) is a polyimide drift straw tube tracker with continuous tracking ability, in contrast to the silicon technology used in the Pixel and SCT. It contains 50,000 straws in the barrel region, and each straw is 144 cm long. In both endcaps there are 250,000 straws, which are 39 cm in length. Each straw tube is 4 mm in diameter, has a gold-plated tungsten wire in the middle, surrounded by a gas mixture of 70% xenon, 27% carbon dioxide and 3% oxygen. The small diameter enables the operation of the tube at a very high rate.

The straw tube is a well-established technology for fast precision particle tracking. When a charged particle transverses the straw tube, it ionizes the gas mixture. The electrons to drift towards the tungsten wire, while the ions drifting towards the opposite direction to the outer edge of the straw. When the electrons arrive near the wire, an avalanche process takes place and generates a signal for readout. The straw tubes also detect transition-radiation photons created by electrons in a radiator between the straws[33], allowing the electrons to be distinguished from other particles. The TRT is by design radiation hard, and provides typically 36 measurements for every track. The TRT has very fast readout and offers good pattern recognition for a modest cost.

2.2.4 The Calorimeter

The ATLAS calorimeters measure the energy and position of electrons and jets with excellent precision. Unlike the Inner Detector, calorimeters aim to completely absorb particles, forcing them to deposit all theor energy. Most known particles can be absorbed by the calorimeters, except for muons and neutrinos.

The Calorimeter is comprised of sampling detectors with full ϕ-symmetry and coverage around the beam axis. It is built with active and passive material in turns, where the sampling of the energy occurs in the active volume, and showers are initiated and develop in the passive volume. The

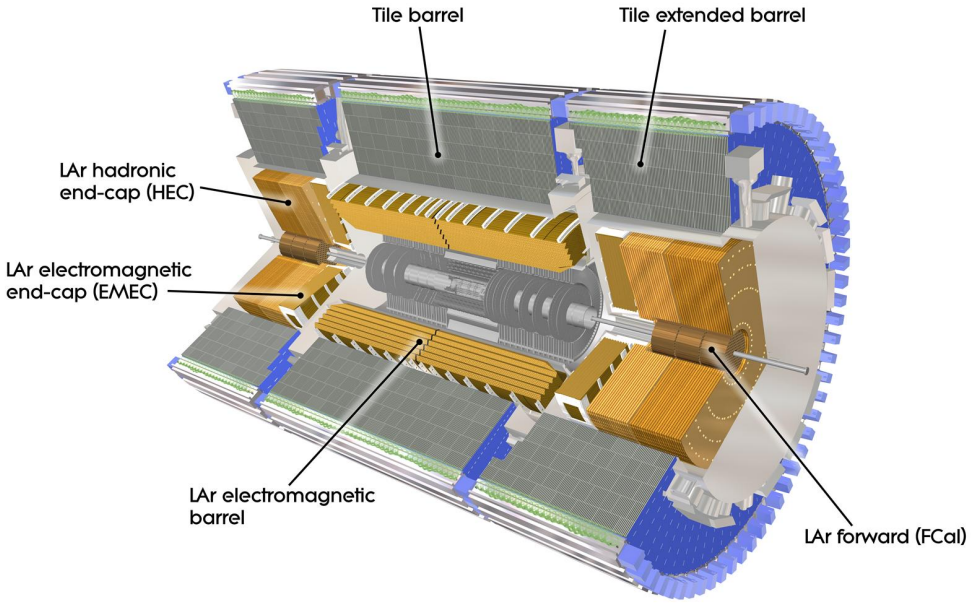

Figure 16: A cut-out view of the ATLAS calorimeter detectors.[34]

liquid argon (LAr) electromagnetic calorimeter, including one barrel detector and two LAr ElectroMagnetic End-Caps (EMEC) sit right behind the Inner Detector in the cryostat. The hadronic calorimeters include the Tile Barrel and the LAr Hadronic End-Cap calorimeter (HEC), located right after the electromagnetic calorimeters. A LAr Forward Calorimeter (FCal), which has one layer of EM and two layers of hadronic detectors, is also in place to cover the region closest to the beam.

The performance requirements for the Calorimeter are stringent. The energy resolution of a calorimeter is parameterized as:

$$\frac{\sigma_E}{E} = \frac{a}{\sqrt{E}} + \frac{b}{\sqrt{E}} + c\,, \tag{58}$$

where a is the coefficient of the sampling term, representing the statistical component of resolution from the detetor itself, b is the electronic noise term and c is a constant. In Higgs search, the sampling term is required to be 10% for the electromagnetic calorimeters, 50% for the hadronic calorimeters and 100% for the forward calorimeters. The constant term is required to be 0.7%

for the electromagnetic calorimeters, 3% for the hadronic calorimeters, and 10% for the forward calorimeters[35]. According to the recent performance study in [27], all of the requirements were fulfilled.

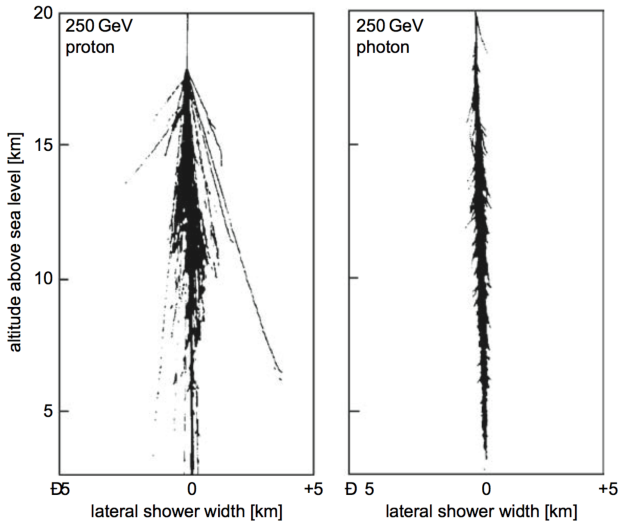

Figure 17: Monte Carlo simulations of the different development of hadronic and electromagnetic, induced by 250 GeV protons and photons in Earth's atmosphere[36]. The hadronic showers are produced by strong interactions in matter, while electromagnetic shower is produced by electromagnetic interactions, such as electron-positron pair production.

2.2.4.1 Electromagnetic Calorimeter The ATLAS electromagnetic (EM) calorimeter system is based on Pb-LAr (lead-liquid-argon) technology, with an "accordion" layout as shown in Figure 18. It covers the pseudorapidity range $|\eta| < 3.2$, and extends the coverage all the way to $|\eta| = 4.9$. It uses liquid argon as the active material, and lead as the passive / absorber. When a charged particle transverses into the LAr calorimeter, it interacts with the absorber and creates an electromagnetic shower. Then, the electrons from the shower will ionize the liquid argon and create a current in the copper electrode, sampling the energy deposit.

The accordion geometry is adopted for the lead plates and electrodes in the LAr barrel and EMEC. This choice is because with such geometry can provide a full ϕ-coverage without leaving any cracks, to ensure an almost hermetic system. The detailed configuration of this geometry is shown in Figure 18.

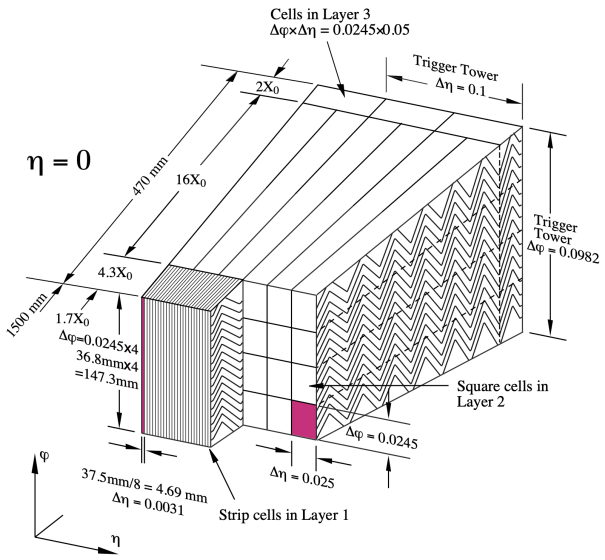

Figure 18: Sketch of a barrel module where the different layers are clearly visible with the ganging of electrodes in ϕ The granularity in η and ϕ of the cells of each of the three layers and of the trigger towers is also shown.[27]

2.2.4.2 Hadronic Calorimeter There are two technologies used for hadronic calorimetry in the ATLAS: scintillating tiles used in the tile calorimeter (TileCAL), and liquid argon used in the hadronic end-cap calorimeter (HEC) and the Forward Calorimeter (FCal). The region of $|\eta| < 1.7$ is covered by the tile calorimeter; the HEC covers $1.5 < |\eta| < 3.2$, the FCAL covering $3.1 < |\eta| < 4.9$. The HEC overlaps with the tile calorimeter on one side and the FCal on the other, in order to avoid cracks in the transition regions. Together they get energy measurement over a wide range of η in the end-cap region.

The tile calorimeter uses steel as its absorber and plastic scintillators as the active medium, in contrast to the HEC and FCAL, which uses tungsten as the absorber, and liquid argon as the active material. The choice of active media is determined based on the cost and radiation hardness.

2.2.5 The Muon Spectrometer

The ATLAS Muon Spectrometer (MS) constitutes the outermost part of the entire detector, with a surface area large enough to cover several soccer fields. Since the muon has a large mass and relatively long lifetime, it penetrates the rest of the detector without generating electromagnetic or hadronic showers while losing little energy through ionization. Sensitive tracking technology is used in the MS to reconstruct the trajectory of a muon, with a low background from other particles.

The MS contains four subsystems: Monitored Drift Tubes (MDT), Cathode Strip Chambers (CSC), Resisitve Plate Chambers (RPC) and Thin Gap Chambers (TGC). The MDT and CSC are the two precision-tracking chambers, where the RPC and TGC are mostly used for triggering. A roughly $|\eta| < 2.7$ coverage is achieved by the MS. Its performance goal is a stand-alone transverse momentum resolution of approximately 10% for 1-TeV tracks, implying a sagitta along the beam axis of 500 μm, to be measured with a resolution of $\leq 50\mu m$. An excellent charge identification is also provided, for tracks of all momenta.

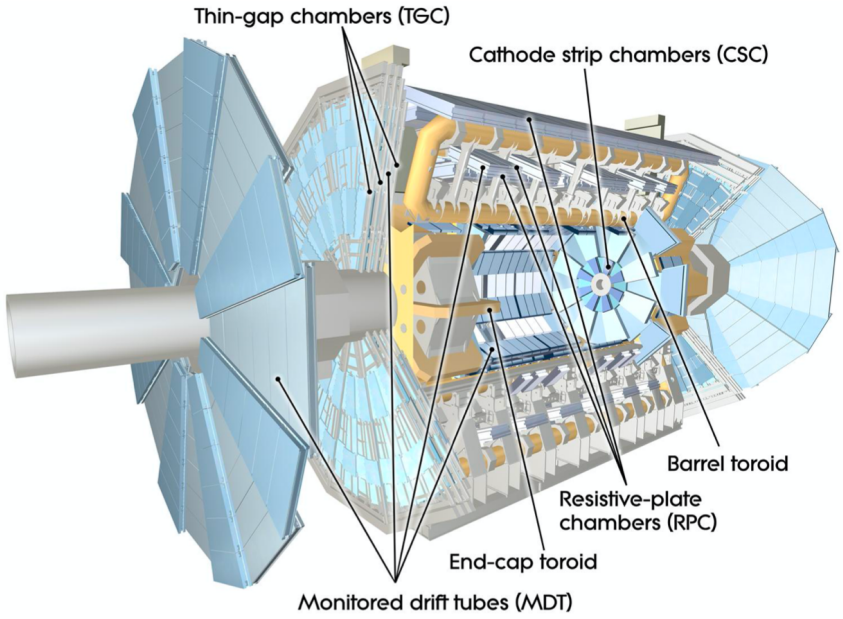

Figure 19: A schematic of the ATLAS muon spectrometer with all four of its subsystems.[27]

The MDT chambers are comprised of three to eight layers of drift tubes, which are made of thin tubes containing a stretched wire within a gas volume. When a muon or any charged particle

passes through, it ionizes the gas, liberating electrons which drift to the side or center of the tube. Tracks are reconstructed from the pattern of hits in the muon chambers. The CSCs are used in the end-cap regions where the event rates are high. They consist of layers of positively-charged anode wires oriented perpendicularly to negatively-charged copper "cathode" strips, also immersed in a gas volume. When a muon traverses the CSC, the gas is ionized and creates a so-called "Townsend avalanche", which produces a pulse for readout. The RPC and TGC both operate on the same principle as the CSC, but are optimized to achieve an even higher rate and time resolution for the purpose of triggering events. They are both fast tracking detectors with time resolution less than the bunch spacing, 25 ns.

2.2.6 Trigger, Data Acquisition

The ATLAS trigger and data acquisition (TDAQ) system selects and records interesting events with a 200 - 400 Hz rate from the initial interaction rate of roughly 40 MHz at the LHC. There are three stages of trigger systems, with each stage applying more refined selection criteria than the previous one:

- **Level 1**, or **L1 Trigger**, is built from fast online electronics that aims to search for high transverse-momentum (p_T) particles including muons, electrons, photons, and jets as well as large missing and total transverse energy. Information from only a subset of detectors, the muon trigger chambers and reduced-granularity information from all calorimeters, is accessible. A trigger "menu" including thresholds on such information in one or more Regions-of-Interest (RoI's) is then used to configure the trigger for event selection during data taking. L1 triggers make a decision within less than 2.5 μs, and bring the event rate down to 75 kHz.
- **Level 2**, or **L2 Trigger**, part of the higher level (HL) triggers, refines the selection based on events that passed the L1 trigger, by using the complete set of detectors with full granularity and precision. The L2 trigger further reduces the trigger rate to approximately 3.5 kHz, with an event processing time of about 40 ms in average.
- **The event filter**, also part of the HL triggers, serves as the final stage of the trigger system, and uses offline analysis procedures with an average event processing time of 4 seconds. It reduces the trigger rate to 200 - 400 Hz.

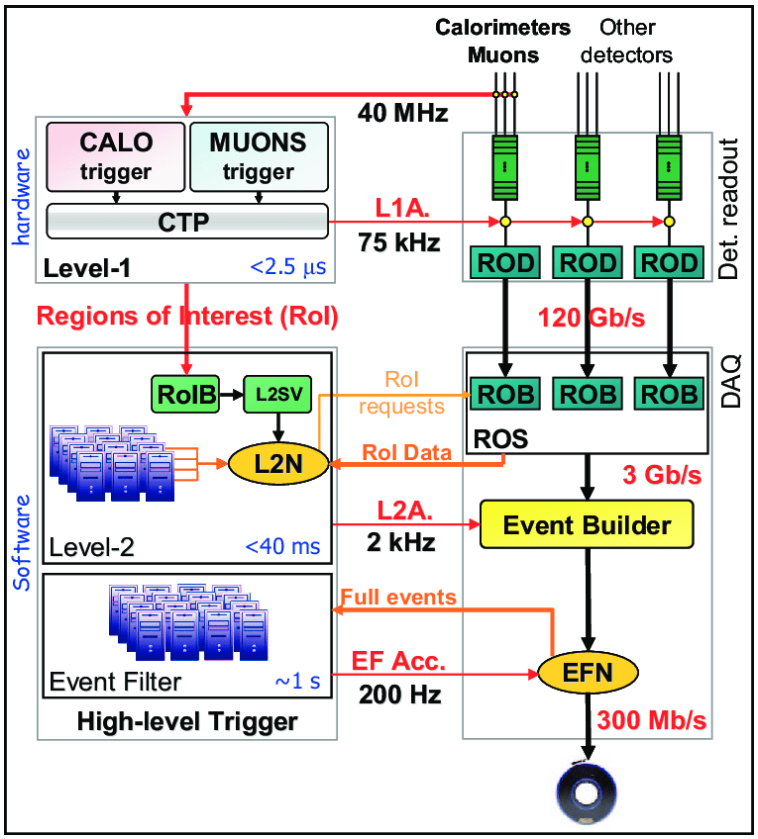

Figure 20: Overview of the overall architecture of the ATLAS Trigger system.[37]

The Data Acquisition (DAQ) system controls the readout of data, and provides for the configuration of the detector system and monitoring of the hardware and software components. The data selected by the L1-trigger is first stored in local buffers. The L2 trigger then requests the data from the buffers to be processed further. The DAQ then transfers the data to the event-building system before sending them to the event filter, from which are moved to permanent storage at the CERN computer center.

2.3 Physics Object Reconstruction

Complex software is needed to process digitization from the ATLAS detectors, into data which is useful for analysis. The software combines tracking information from the Inner Detector and the Muon Spectrometer, and energy deposits from the Calorimeters. Complex algorithms are developed in order to resolve ambiguities, find interaction vertices, tag the flavor of jets and effectively reconstruct physical objects from their decay products.

2.3.1 Track Reconstruction And Vertex Finding

The ATLAS detector contains two independent tracking detectors: the Inner Detector and the Muon Spectrometer. The track reconstruction software is modular and flexible and fulfills the requirements of both subsystems through a common Event Data Model (EDM) [38]. The primary pattern recognition for track finding follows mainly an *inside-out* strategy, followed by *outside-in* tracking.

The *inside-out* strategy is achieved by a series of modules each with a dedicated algorithm. The first step is to create a three-dimensional representation of the silicon detector measurements, called `SpacePoint` objects. Then, a track finding process takes place "seeded" by the `SpacePoint` objects, and is eventually used to build physical objects. A Kalman fitter-smoother formalism, which is essentially equivalent to a global least-squares minimization, is used to simultaneously follow the trajectory and include hits to the track candidate. Numerous spurious track candidates may be found during this process, either incomplete or fake tracks. Therefore, the candidates are ranked in likelihood to be a "real" track, determined by refitting the track with refined reconstruction geometry, and using a dedicated *track scoring* that assigns a beneficial or penalty track score. Finally, the tracks are extended into the TRT and refitted again with full detector information. The extended track is preferred if the fit score is better. The *outside-in* strategy searches for unused track segments in the TRT and is similar to the *inside-out* strategy.

After obtaining particle tracks, vertex-finding process associate the tracks to find the best positions for the interaction vertex. The reconstruction of primary vertices can generally be subdivided in two stages[39]:

- **Primary vertex finding**: association of reconstructed tracks to a particular vertex candidate.
- **Vertex fitting**: reconstruction of the actual vertex position and its covariance matrix, estimate of the quality of the fit, and refit of the incident tracks.

The algorithms featuring both the "fitting-after-finding" and "finding-through-fitting" approaches are implemented in the ATLAS Athena framework.

2.3.2 Electron Identification And Reconstruction

2.3.2.1 Central Region Electron reconstruction in the central region ($|\eta| < 2.47$) combines the energy deposits (clusters) in the EM calorimeter, and the reconstructed tracks of charged particles from the Inner Detector [40]. The EM clusters are seeded by energy deposits, which are required to have greater than 2.5 GeV of total transverse energy, and through a sliding-window algorithm with a window size of 3×5 in units of 0.025× 0.025 in (η, ϕ) space. The efficiency of this process is very high – expected to be roughly 97% at E_T= 7 GeV, and almost 100% at E_T >20 GeV from Monte Carlo (MC) simulations of W and Z leptonic decays. Then, reconstructed tracks with $p_T >$ 0.5 GeV, extrapolated from their last measured point to the middle layer of the EM calorimeter, are loosely matched to the seed clusters. A track is considered successfully matched if the distance between the impact point and the EM cluster barycenter is $|\Delta\eta| < 0.05$. Corrections such as losses from bremsstrahlung are calculated in the tracking as well. Finally, among all the candidate tracks, the one with the smallest $\Delta R = \sqrt{\Delta\eta^2 + \Delta\phi^2}$ distance to the seed cluster is chosen, and an electron candidate is formed.

2.3.2.2 Forward Region In the forward region ($2.5 < |\eta| < 4.9$), the electron reconstruction is performed only from the energy deposits in the EM calorimeters, due to the lack of tracking information. In $\eta > 2,5$, measurement is performed by grouping neighbouring cells in three dimensions in order to give directional information. Such clusters are called topological clusters, comprised of a variable number of cells, in contrast to fixed-size sliding window clusters used in the central region. The energy of the electron is determined in a manner similar to that of the central electrons – by summing up the energies in the cluster cells and adding corrections for energy loss. Finally, an electron in the forward region is constructed only when it has $E_T > 5$ GeV.

2.3.2.3 Electron Identification Among the reconstructed electrons, a high contamination is expected from background electrons (primarily from photon conversions), non-isolated electrons and jets faking electrons. Cut-based selection is used to identify electrons with a good background rejection. Discriminating variables include the shape of the EM shower, the quality and length of the tracks and the track-to-calorimeter matching. After combining variables from the calorimeter and tracking, three reference selections of cuts are defined with increasing background rejection power: loose, medium and tight[41], in the central region. A detailed breakdown of the discriminators are shown in Table 6. For the forward electrons, no tracking related discriminants are available. Therefore, two reference sets of cuts are defined: forward loose and forward tight, which are solely based on cluster moments and shower shapes. In parallel, there is also a likelihood-based identification process, which has a similar structure to the cut-based method. Their performance comparison is shown in Figure 21.

Type	Description
	Loose selection
Acceptance	$\|\eta\| < 2.47$.
Hadronic leakage	Ratio of E_T in hadronic calo to that of the EM cluster.
Middle layer of EM calo	Energy ratio, Lateral shower width.
	Medium selection (includes loose)
Strip layer of EM calo	Shower width, E_{ratio} of the largest two deposits over the sum.
Track quality	n_{pixel} hits on the pixel, n_{Si} hits on the pixel and SCT, transverse impact parameter ($\|d_0\|$ <5 mm.
Track-cluster matching	$\Delta\eta$ between the cluster position in the strip layer and track.
	Tight selection (includes medium)
Track quality	Tighter requirement $\|d_0\| < 1$ mm.
Track-cluster matching	$\Delta\phi$ <0.02 between the cluster position and the track.
TRT	n_{TRT} hits in TRT, Ratio of high-threshold hits.
Conversions	n_{BL} hits in the b-layer, veto when matched to photon conversions.

Table 6: Definition of discriminating variables in the central region for loose, medium and tight electron identification cuts[40].

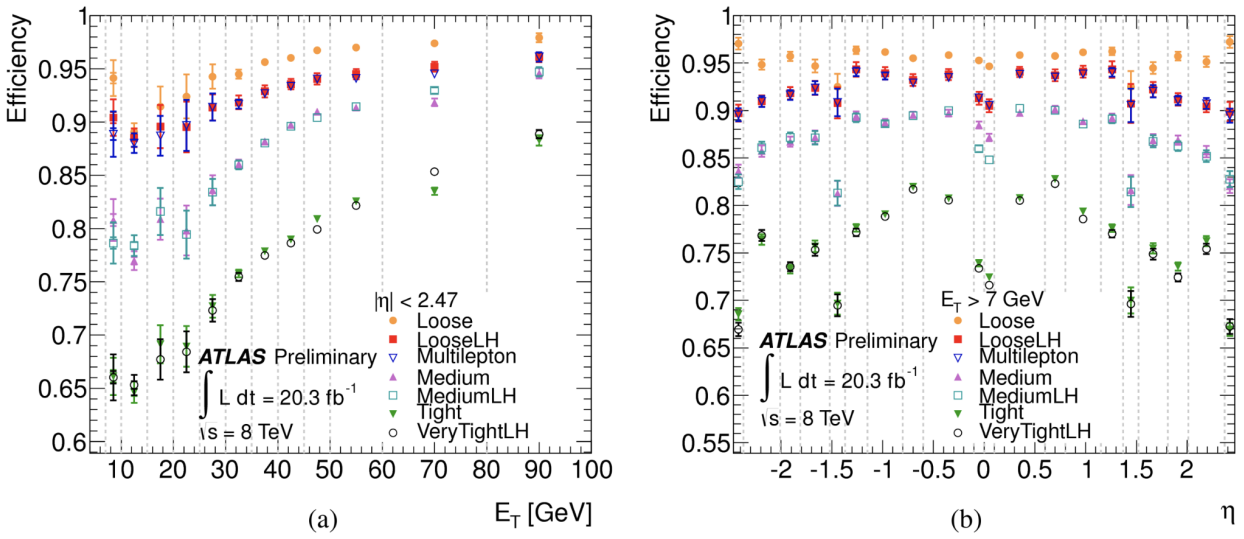

Figure 21: Measured combined reconstruction and identification efficiency for the various cut-based and likelihood selections as a function of (a) E_T and (b) η for electrons in Run 1.[42]

2.3.3 Muon Reconstruction And Identification

The muon reconstruction is based on precision measurements in the muon spectrometer combined with the Inner Detector[43][44]. A similar as with electron reconstruction is followed.

The muon identification is also based on a cut-based selection, where quality requirements are applied to suppress background, mainly from pion and kaon decays. There are four muon types defined depending on which subdetectors are used in reconstruction. They are:

- Combined (CB) muons: track reconstruction is performed independently in the ID and MS, and a combined track is formed with a global refit that uses the hits from both subdetectors.
- Segment-tagged (ST) muons: a track in the ID is classified as a muon if, once extrapolated to the MS, it is associated with at least one local track segment in the MDT or CSC chambers. It is used when the muons cross only one layer of MS chambers.
- Calorimeter-tagged (CT) muons: a track in the ID is identified as a muon only if it can be matched to an energy deposit in the calorimeter compatible with a minimum-ionizing particle.

This type has the lowest purity of all the muon types.

- Extrapolated (ME) muons: the muon trajectory is reconstructed based only on the MS track and a loose requirement on compatibility with originating from the IP. In general an ME muon is required to traverse at least two layers of MS chambers, and three layers in the forward region. It extends the acceptance for muon reconstruction into the region $2.5 < |\eta| < 2.7$.

Specific requirements such as the number of hits in the ID and MS are enforced to guarantee a robust momentum measurement. Table 7 shows a detailed breakdown of the discriminators.

2.3.4 Jet Reconstruction And Identification

Quarks and gluons undergo hadronization and produce a collimated spray of particles known as jets, through gluon splitting and radiation. The goal of jet reconstruction is to estimate the momentum of the original parton from the spray. The anti-k_t algorithm[46] is the default jet clustering algorithm in ATLAS. The algorithm clusters particles into a single jet (clustering) and combines their four-momenta. It is a sequential clustering algorithm, which combines particles in a bottom-up manner. The combination is performed according to the distance parameters:

$$d_{i,j} = \min(k_{T,i}^{-2}, k_{T,j}^{-2})\frac{\Delta R}{R}, \tag{59}$$

$$d_{i,beams} = k_{T,i}^{-2}, \tag{60}$$

where k_{T_i} is the momentum of object i on the $x - y$ plane transverse to the beam axis, and ΔR is the distance between objects i, j. The parameter R controls the size of the jet. The four-momentum of the jet is therefore simply the sum the four-momenta of the constituent objects. The other main class of jet algorithms is called cone algorithms, which finds coarse regions or cones of energy flow in a top-down manner.

Type	Description
	***Medium* selection**
Muon types	Combined (CB) and Extrapolated (ME) muons.
Acceptance	$\|\eta\| < 2.7$.
Track quality	$\leq$3 hits in at least 2 MDT layers, except for $\|\eta\| < 0.1$ for CB; at least 3 MDT/CSC layers, only in $2.5 < \|\eta\| < 2.7$ for ME.
q/p significance	< 7.
	***Loose* selection (includes *Medium*)**
Muon types	All
Track quality	CT anb ST muons restricted to $\|\eta\| < 0.1$.
	***Tight* selection**
Muon types	CB muons only that passed *Medium* selection.
Track quality	Hits in at least two stations of the MS.
Additional requirements	A two-dimensional cut in the ρ' and *q/p significance* variables as a function of the muon p_T to reject more background for momenta below 20 GeV.
	***High-*p_T selection**
Muon types	CB muons only that passed *Medium* selection.
Track quality	≤ 3 Hits in three stations of the MS.
Additional requirements	Reduced reconstruction by about 20% to improve the p_T resolution of muons above 1.5 TeV by approximately 30%

Table 7: Definition of discriminating variables in the central region for medium, and tight, loose, and high-p_T muon identification cuts[45]. The *q/p significance* is defined as the absolute value of the difference between the ratio of the charge and momentum of the muons measured in the ID and MS divided by the sum in quadrature of the corresponding uncertainties.

2.3.4.1 b-tagging The identification of jets containing a b-quark, or b-tagging, is important for both precision SM measurements and for searches. In the SM the top quark decays into a bottom quark almost 100% of the time, so b-tagging performance has a significant impact on the

top polarization measurement.

The algorithms to identify jets containing b hadrons are mostly developed by exploiting the long lifetime (τ_b 1.5 ps), high mass (4.18 ± 0.04 GeV) and decay multiplicity of b hadrons and the hard b-quark fragmentation function [47]. A common approach in b-tagging is to look for the significance of the decay length of a secondary vertex with respect to the primary vertex. Therefore, the most important input for b-tagging are the reconstructed charged particle tracks in the Inner Detector with $|\eta| < 2.5$. Other quantities such as the transverse and longitudinal impact parameters of the charged particle tracks are considered in more refined algorithms, and combined in the artificial neural network in order to achieve the best discrimination.

The performance of the b-tagging algorithms has been studied through simulated events and in data, and the b-tagging efficiency ($\epsilon_b = N_{b,tag}/N_b$) is calibrated using an inclusive sample of jets containing muons as well as a sample of $t\bar{t}$ events with one or two leptons in the final state. The mistag rate is also measured through an inclusive jet sample. Selection criteria with b-tagging efficiencies of 40%, 55% and 70% working points are referred to as: tight, medium and loose. A series of comparisons of the b-tagging efficiency, c-jet rejection and light-jet rejection with respect to different working points are shown in Figure 22- 24.

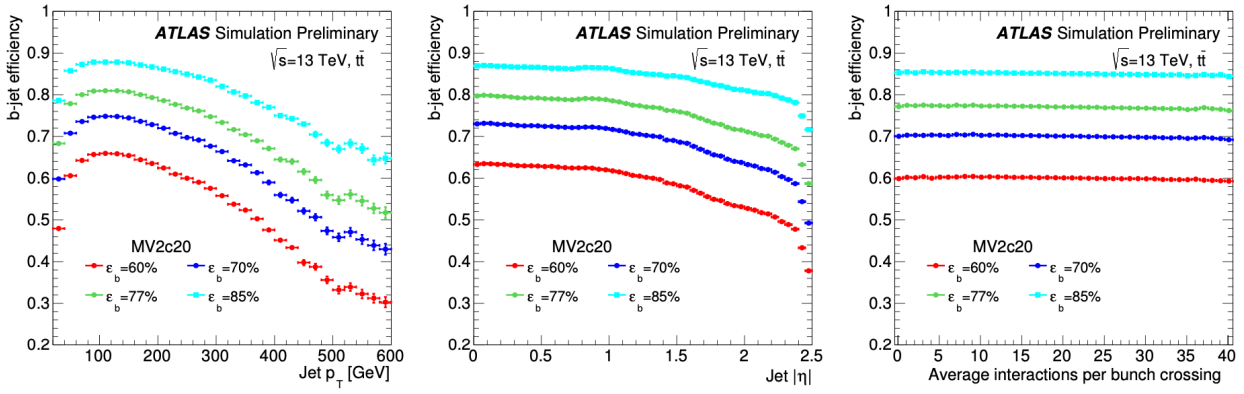

(a) (b) (c)

Figure 22: The b-jet efficiency for the four working points: 60% (red), 70% (blue), 77% (green) and 85% (light blue). Efficiencies are shown as a function of the jet p_T (a), $|\eta|$ (b) and the average number of interaction per bunch crossing (c)[48].

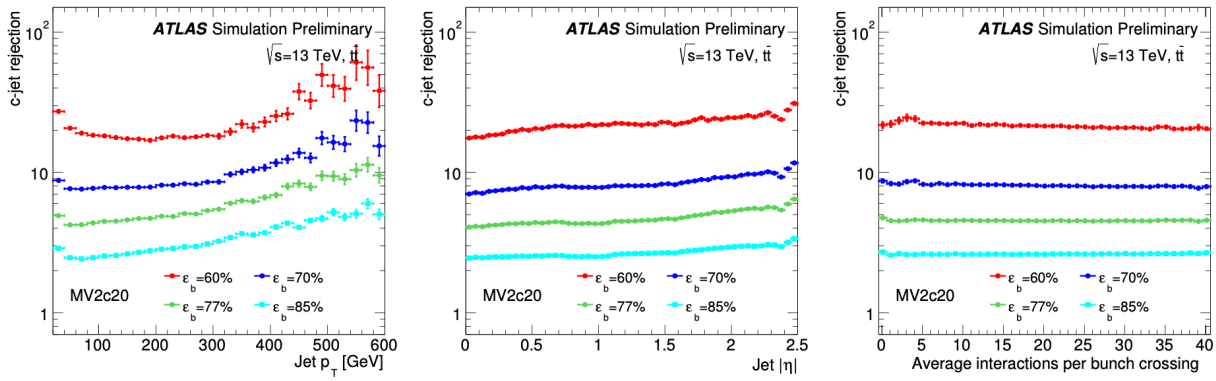

Figure 23: The c-jet rejection for the four working points: 60% (red), 70% (blue), 77% (green) and 85% (light blue). Efficiencies are shown as a function of the jet p_T (a), $|\eta|$ (b) and the average number of interaction per bunch crossing (c)[48].

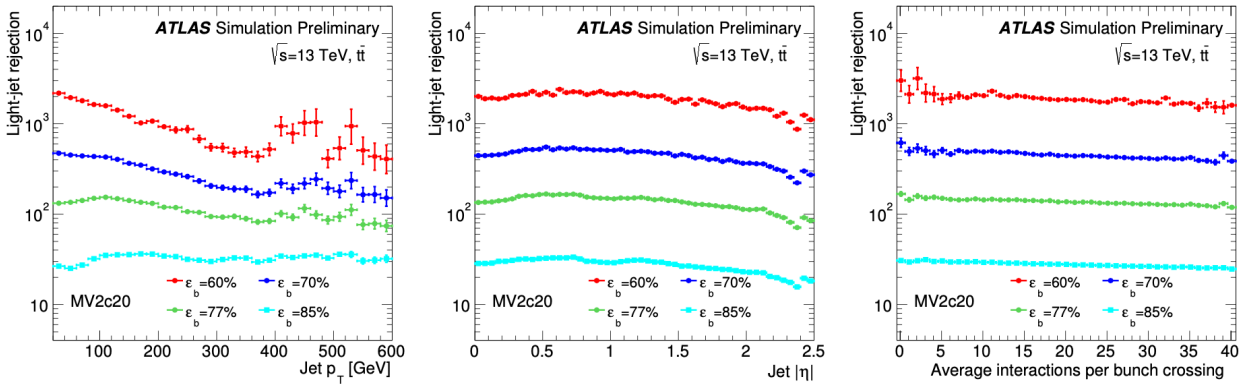

Figure 24: The light-flavour jet rejection for the four working points: 60% (red), 70% (blue), 77% (green) and 85% (light blue). Efficiencies are shown as a function of the jet p_T (a), $|\eta|$ (b) and the average number of interaction per bunch crossing (c)[48].

2.3.5 Missing Transverse Momentum

The missing transverse momentum (E_T^{miss}) is an important observable. A value incompatible with zero can indicate the production of SM neutrinos, or more exotic weakly interacting particles escaping the detector. The reconstruction of the E_T^{miss} considers two contributions:

- **Hard-event** signals with fully reconstructed and calibrated particles (e,γ,τ,μ) and jets (hard objects).
- **Soft-event** signals reconstructed comprising charged-particle tracks (soft signals) associated with a hard-scatter vertex, but not with a hard object.

The E_T^{miss} reconstruction sums the transverse momentum vectors $\vec{p}_T$ of the various contributions[49]. The missing transverse momentum components $E_{x,(y)}^{\text{miss}}$ are given by:

$$E_{x(y)}^{\text{miss}} = -\sum_{i\in\{\text{hard objects}\}} p_{x(y),i} - \sum_{j\in\{\text{soft objects}\}} p_{x(y),j}. \tag{61}$$

The set of observables obtained from $E_{x(y)}^{\text{miss}}$ is:

$$\vec{E}_T^{\text{miss}} = \left(E_x^{\text{miss}}, E_y^{\text{miss}}\right) \tag{62}$$

$$E_T^{\text{miss}} = |\vec{E}_T^{\text{miss}}| = \sqrt{E_x^{\text{miss}^2} + E_y^{\text{miss}^2}} \tag{63}$$

$$\phi^{\text{miss}} = \tan^{-1}\left(E_y^{\text{miss}}/E_x^{\text{miss}}\right) \tag{64}$$

Another observable is the scalar sum of all transverse momenta from the objects contributing to E_T^{miss} reconstruction:

$$\sum E_T = \sum_{i\in\{\text{hard objects}\}} p_{T,i} + \sum_{j\in\{\text{soft objects}\}} p_{T,j} \tag{65}$$

In real experiments however, not all relevant p_T from hard-scattered interaction from all contributions can be reconstructed perfectly, which introduces an observation bias towards non-vanishing E_T^{miss} values. The bias can be determined from the deviation of the observed E_T^{miss} from the expectation value for a given final state, either with or without a genuine source of missing transverse momentum. For example, the events with $Z \to \mu\mu$ decays are good candidates to study the E_T^{miss} reconstruction performance, since Z kinematics can be measured with high precision, and have no genuine missing transverse momentum other than very rare heavy-flavor decays in the hadronic

recoil. On the other hand, events with $W \to l\nu$ decays can be used for linearity study in order to quantify the E_T^{miss} response when there is a genuine contribution in the final state. The performance plots based on these processes are shown in Figure 25 and in Figure 26.

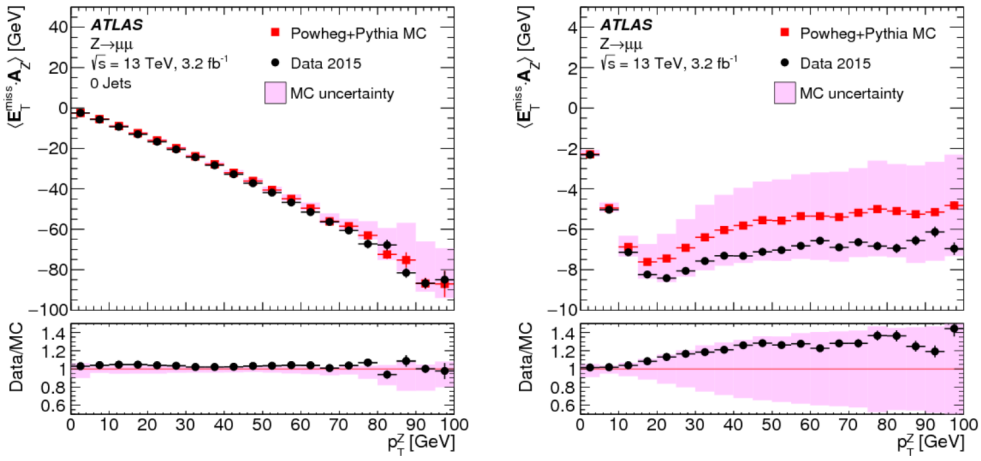

Figure 25: The average projection of E_T^{miss} onto the direction $\mathbf{A}_Z$ of the Z boson's transverse momentum vector $\mathbf{p}_T^Z$, is shown as a function of $p_T^Z = |\mathbf{p}_T^Z|$ in $Z \to \mu\mu$ events from (a) the N_{jet} = 0 sample and from (b) the inclusive sample. In both cases data are compared to MC simulations. The ratio of the averages from data and MC simulations are shown below the plots[49].

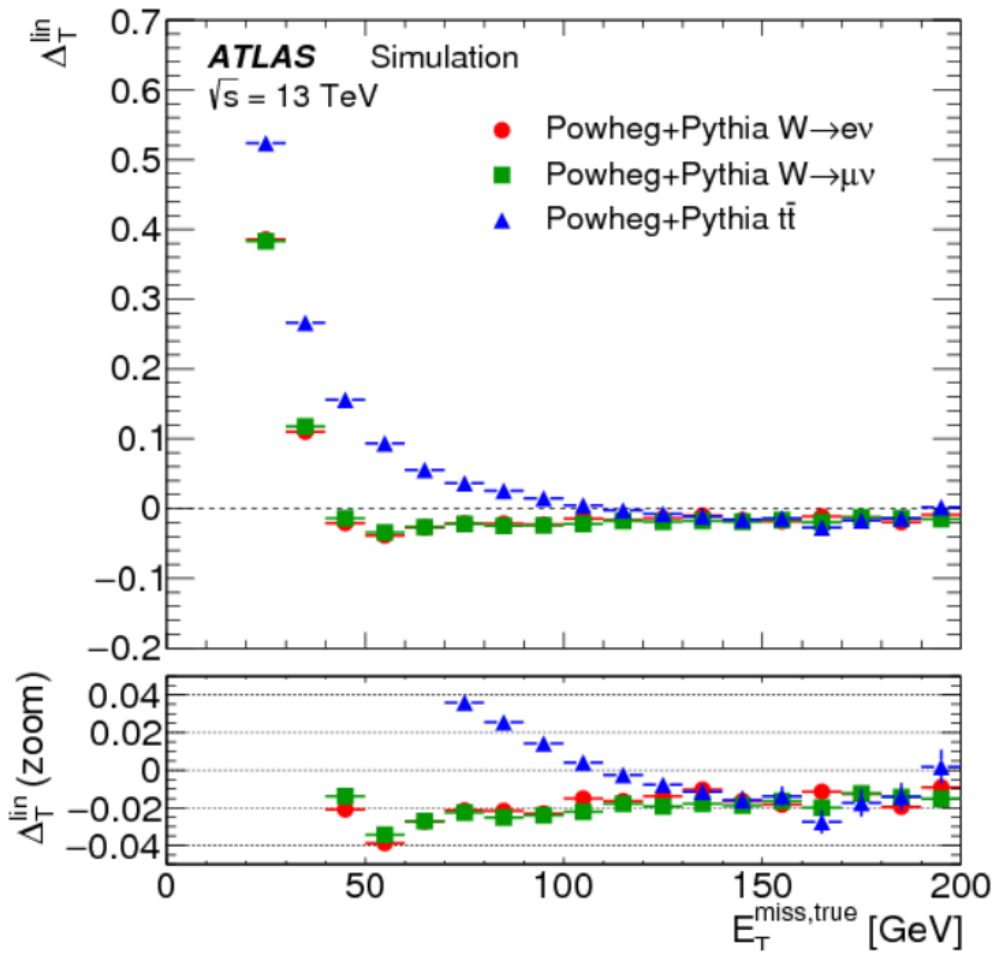

Figure 26: The deviation of the E_T^{miss} response from linearity, measured as a function of the expected $E_T^{\text{miss,true}}$ by $\Delta_T^{lin} = (E_T^{\text{miss}} - E_T^{\text{miss,true}})/E_T^{\text{miss,true}}$, in $W \to e\nu$, $W \to \mu\nu$, and $t\bar{t}$ final states in MC simulations. The lower plot shows a zoomed-in view on the Δ_T^{lin} dependence on $E_T^{\text{miss,true}}$ with a highly suppressed ordinate [49].

3.0 Complete Measurement of the Top-quark Polarization in T-channel Single Top-quark Production Using Pp Collisions at 13 TeV with the ATLAS Detector

This chapter describes the complete measurement of the top-quark polarization from the t-channel single top production in fiducial region at $\sqrt{s} = 13$ TeV. The measurement is 'complete' in the sense that all three components of the polarization vector $\mathbf{P} = (P_x, P_y, P_z)$ are determined. No previous measurement of the quantities currently exists.

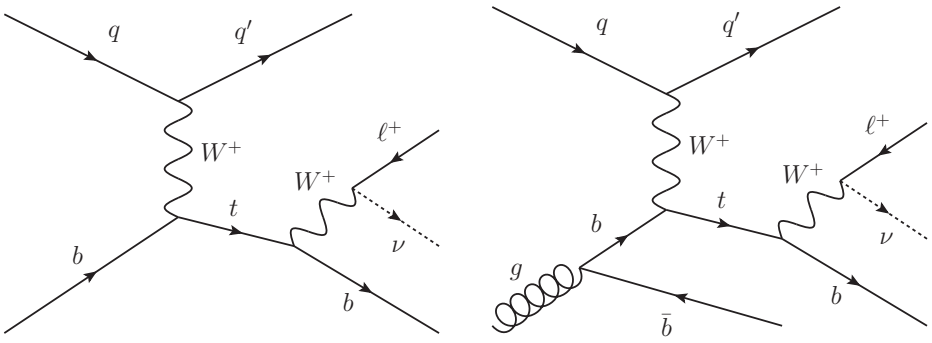

Figure 27: Representative LO Feynman diagrams for t-channel single top-quark production and decay. Here q represents the initial light quark and q' the spectator quark. The initial b-quark arises from (left) a sea b-quark in the 5FS (i.e. $2 \to 2$ process), or (right) a gluon splitting into a $b\bar{b}$ pair in the 4FS (i.e. $2 \to 3$ process).

3.1 Data And Simulated Samples

This section describes data recorded by the ATLAS detector from 2015 to 2018 as well as MC simulations used in this analysis.

3.1.1 Data

The analyzed data event samples consist of 25 ns pp collisions delivered by the LHC from 2015 to 2018 at $\sqrt{s}$ =13 TeV, and collected by the ATLAS detector. During the successful Run 2 operation of the ATLAS detector at the LHC, the cumulative integrated luminosity recorded which satisfies stringent data quality criteria is approximately 139 fb^{-1} $\pm 1.7\%$. Figure 28 shows the trend and full breakdown of the data that was delivered by the LHC, recorded by the ATLAS detector, and approved by the ATLAS data quality groups after confirming all reconstructed physics objects are satisfactory for analyses. The delivered luminosity is counted from the start of stable beams until the beam dump, while the recorded luminosity is smaller than the delivered due to DAQ inefficiencies and other operation issues.

Year	Periods	Run numbers	Number of events	Integrated luminosity [pb^{-1}]
2015	D-J	276262-284484	220.58M	3219.56$\pm$ 2.1%
2016	A-L	297730-311481	1057.84M	32988.1$\pm$ 2.2%
2017	B-K	325713-340453	1340.80M	44307.4 $\pm$ 2.4%
2018	B-Q	348885-364292	1716.77M	58450.1 $\pm$ 2.0%
2015-2018	All	276262- 364292	4335.99M	138965.16 $\pm$ 1.7%

Table 8: Integrated luminosity per year with their relative uncertainties.

The data samples were collected through the ATLAS trigger system comprising both hardware-based L1 trigger and software-based High Level Trigger (HLT), as described in Section 2.2.6. Single-charged-lepton triggers were used for selecting the data samples, where different triggering criteria were chosen for different years in order to cope with the changing pile-up conditions. In 2015, both electrons and muons are triggered by requiring at L1 a transverse energy deposit $E_T > 20$ GeV, with a reduced calorimetric granularity being considered at L1. Then for the HLT, where the full granularity of the calorimeter as well as other sophisticated algorithms are available, the trigger electron candidate is required to be isolated to satisfy *medium* identification criteria, and to have $E_T > 24$ GeV, whereas the muon candidate is required to be isolated and to satisfy *loose* identification criteria. In 2016-2018, motivated by the increased amount of pile-up, electron

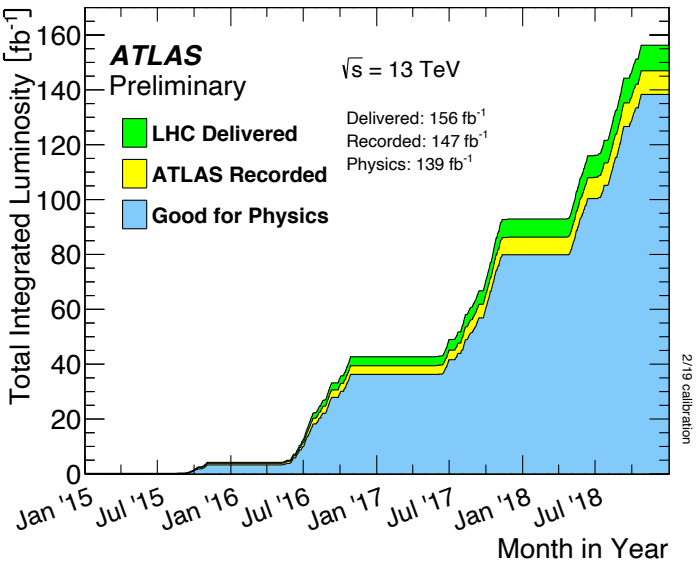

Figure 28: Cumulative luminosity versus time delivered to ATLAS (green), recorded by ATLAS (yellow), and certified to be good quality data (blue) during stable beams for pp collisions at $\sqrt{s}$ =13 TeV in 2015–2018.

candidates were required to satisfy *tight* identification criteria at the HLT, and to have $E_T > 26$ GeV. During Run 2, to avoid efficiency losses due to identification and isolation at high p_T, two additional triggers were also available, selecting medium electrons with $E_T > 60$ GeV at HLT and selecting loose electrons (i.e. without isolation requirement) with $E_T > 120$ GeV in 2015 and $E_T > 140$ GeV in 2016-2018. As for muons, one extra muon trigger without any isolation requirement is available for all three years, selecting loose muons with $E_T > 50$ GeV.

Overlap removal is performed on the data sample, following the recommendations of the top-quark reconstruction working group [50]. An electron sharing a track with a muon is removed in case a muon 'fakes' an electron through the radiation of a hard photon. Jets overlapping with selected electron candidates within an η–ϕ cone of size $\Delta R = 0.2$ are removed from the event to reduce the proportion of electrons being reconstructed as jets. Any electron found close to non-pile-up jet within a cone of radius $\Delta R = 0.4$ is also removed, in order to reduce backgrounds from non-prompt, non-isolated electrons coming from heavy-flavour hadron decays. Any jet with less

than three tracks originating from the primary vertex is removed if found within a cone of radius $\Delta R < 0.2$ from a muon or if it has a muon ID track segment associated to it. This is to reduce fake jets from muons depositing energy in the calorimeters. Finally, muons within a distance $\Delta R < 0.4$ from any of the surviving jets are removed to avoid contamination of non-prompt muons from heavy-flavour hadron decays.

3.1.2 Reconstruction of the E_T^{miss}

The missing transverse momentum, with magnitude E_T^{miss}, is reconstructed from the negative vector sum of energy deposits in the calorimeter projected onto the transverse plane as described in Section 2.3.5. The E_T^{miss} of the event is assumed to correspond to the sum of the transverse momenta of any prompt neutrino (E_T^{miss} = $\equiv \sum_\nu p_{\text{T}}^\nu$). Although it is true that the neutrino is the main contributor to the E_T^{miss} at LO, there are more contributors, such as extra neutrinos (from B-hadrons and τ decays), additional p_T contributions (from ISR/FSR effects and detector energy resolution, etc), miscalibration of E_T^{miss}, etc. If these additional contributions are ignored for the full reconstruction of single top-quark events, the only undetermined quantity is the longitudinal momentum of the neutrino, p_z^ν. Constraining the mass of the lepton-E_T^{miss} system to the W-boson mass constrains this quantity, but with a quadratic ambiguity. If the resulting quadratic equation has two possible real solutions, the solution giving the smallest magnitude of the longitudinal neutrino momentum, $|p_z^\nu|$, is taken. In case of complex solutions, the magnitude of the measured E_T^{miss} is re-scaled (decreased) until a physical solution is obtained. Once this is done, the kinematics of the top-quark candidate is reconstructed by simply combining the four-momentum of the reconstructed W boson and the b-tagged jet. The detailed description of this method can be found in Appendix A.

3.1.3 Reconstruction of the Top Quark and W Boson

Once the four-momentum of the neutrino is fully determined, the four-momentum of the W boson can be reconstructed. Unlike the reconstruction of the top quarks in $t\bar{t}$ events, in single top-quark t-channel events where $t \to Wb$, there is only one possibility to combine the final physics objects to obtain the top quark. Obviously, the reconstructed W boson mass is exactly the W boson pole-mass, which has already been used as a constraint. The actual value of the W-boson decay

width is in fact $\Gamma_W = 2.085 \pm 0.042$ GeV [51].

Finally the top quark is also fully reconstructed from the sum of the four-vectors of the W boson and the uniquely selected b-tagged jet.

3.1.4 Event Simulation

A large number of simulated events are needed for the purpose of predicting and estimating the signal and background contributions using theoretical inputs, and incorportating the responses of ATLAS detector subsystems. This analysis uses MC for constructing fitting templates, estimating the background processes and evaluating systematic uncertainties.

There are several stages of MC simulation of pp collisions at the LHC. A typical workflow proceed by simulating, in order: the parton distribution, the hard scattering process, the parton shower, the hadronization and the particle decay. To start with, partons with momentum fraction x are drawn from a parton distribution function (PDF). Then, the hard scattering process is computed at fixed in perturbation theory, and used to generate the final state particles. At this stage quarks and gluons exist, but no hadrons. These two steps occur within parton-level event generators such as POWHEG-BOX [52][53][54],AMC@NLO [55] and PROTOS [15]. Next, the particles undergo the parton shower process, where bremsstrahlung from QED and gluon radiation from QCD take place, leading to so-called initial state radiation (ISR) and final state radiation (FSR). This process continues until the energy scale is reduced to the hadronization scale, and then colorless hadrons start to form. Packages such as `PYTHIA`[56] and `HERWIG`[57] are dedicated to this phase of simulation: their parameters are calibrated with real experimental data and referred to as "tune". Finally, the hadrons decay into stable final state particles that will interact with the detector, whose effects are simulated using the `GEANT4` simulation toolkit[58] for a full simulation or alternatively the `Atlfast2` fast simulation[59]. The `Atlfast2` simulation framework provides fast simulated events by considering a parametric cell response of the ATLAS calorimeters and `GEANT4` for the rest. The reconstruction of the physical objects follows the same procedure as described above for the experimental data. Furthermore, the MC events are weighted to reproduce the distribution of the average number of interactions per bunch crossing ($\langle\mu\rangle$) observed in the data, referred to as "pile-up reweighting". This is to improve the agreement of the number of reconstructed pri-

mary vertices between data and simulation and reproduces the visible cross section of inelastic pp collisions as measured in the data. A brief overview is illustrated in Figure 29.

In this analysis, samples of events generated using MC simulations were produced for t-channel signal and most of the background processes (multijet background is estimated from data in both the muon and electron channel). A detailed list of the MC datasets is given in Appendix **??**.

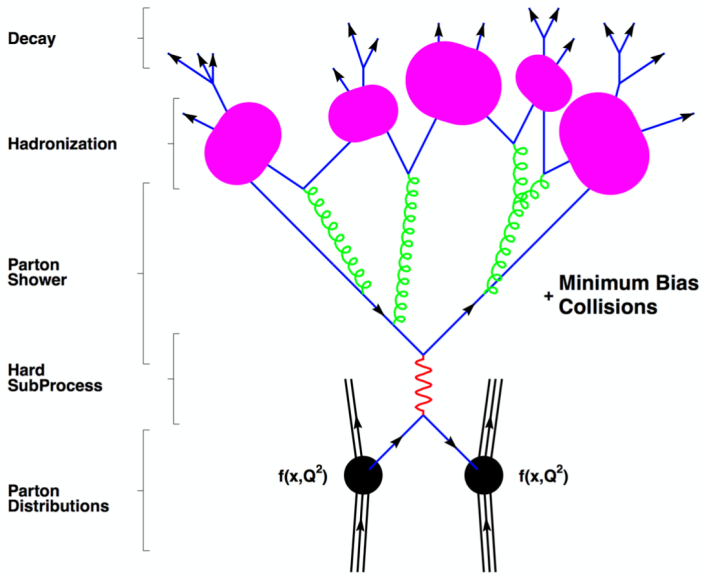

Figure 29: The simplified structure of a generated event, including showering and hadronization, is shown schematically[60].

3.1.4.1 Simulated t-channel Signal Event Samples The baseline sample of the simulated t-channel single top-quark events was produced using the POWHEG-BOX [52] (v2) generator which provides matrix elements (MEs) at NLO in the strong coupling constant α_S in the 4FS with the NNPDF3.0 NLO nf4 PDF set. The functional form of the renormalisation (μ_R) and factorisation (μ_F) scale was set to $\sqrt{m_b^2 + p_{T,b}^2}$ following the recommendation of Ref. [52], where m_b and $p_{T,b}$ are the mass and p_T of the b-quark from the initial gluon splitting, so-called "second b-quark". Top quarks were decayed at LO using MADSPIN [61] to preserve all spin correlations.

Additional samples of simulated t-channel single top-quark events were produced with the LO

PROTOS [1] [15](v2.2b) generator using the CTEQ6L1 PDF sets. The factorization scale is set to $\mu_{\mathrm{F}}^2 = -p_W^2$ for the spectator quark and $\mu_{\mathrm{F}}^2 = p_{\bar{b}}^2 + m_b^2$ for the gluon, where p_W and $p_{\bar{b}}$ are the three-momenta of the exchanged W boson and of the b-antiquark originating from the gluon splitting, respectively. With this LO generator, six event samples with top quarks fully (either positively or negatively) polarized along the three spin axes were produced. These samples are used to build templates for the analysis. Since PROTOS does not have the ability to produce fully polarised event samples, the package POLMANIP was developed in order to introduce arbitrary polarization via a post-processing step. Details of how this procedure is used to build the templates are given in Section 3.5.

In all the above simulated event samples, PYTHIA8 is used to simulate the parton showering (PS), and hadronization. The decays of bottom and charm hadrons are simulated using the EVTGEN (v1.6.0) program [62].

For evaluating the t-channel generator modelling uncertainties, additional single top-quark t-channel simulation samples (or weights within the baseline simulation sample) were produced.

Finally, the POWHEG-BOX samples were passed through the full `GEANT4`-based simulation of the ATLAS detector while the PROTOS were passed through the `Atlfast2` fast simulation of the ATLAS detector. Samples used to estimate the various modelling uncertainties were also processed with the `Atlfast2` simulation. All t-channel simulated event samples were produced considering a top-quark mass of 172.5 GeV and the decay of top quark was assumed to be 100% into $t \to Wb$.

These signal samples were normalised to the predicted single top-quark t-channel production cross-section, which was calculated at NLO in QCD with HATHOR (v2.1) [63]. For pp collisions at $\sqrt{s} = 13$ TeV, this cross-section corresponds to $54.9^{+2.3}_{-1.9}$ pb and $29.7^{+1.7}_{-1.5}$ pb for top quark and antiquark production, respectively, using a top-quark mass of $m_t = 172.5$ GeV. The uncertainties on the cross-section due to PDF choice and α_{S} are also calculated and are added in quadrature to the scale uncertainty.

[1] PROTOS (PROgram for TOp Simulations) is a generator for studying new physics processes involving the top quark. It has generators for single top-quark and top-quark pair production with anomalous *tWb* couplings.

3.1.4.2 Simulated Background Event Samples Various samples of simulated events using MC simulations are used to model the kinematic distributions of the SM background processes. The largest backgrounds to the single top-quark t-channel process in the ℓ+jets channel are:

- Major:
  - Top-quark pair ($t\bar{t}$) production.
  - W+jets production.
- Minor:
  - The single top-quark tW and s-channel productions.
  - Multi-jet production.
  - Z+jets process.
  - Diboson (WW, ZZ and WZ) processes.
  - Other processe such as $t\bar{t}$ and single top-quark productions associated with vector or Higgs bosons ($t\bar{t}Z$, $t\bar{t}W$, $t\bar{t}H$, tZq, tHq and tWZ).

Noted that the multijet background is estimated using either MC- or data-driven techniques. More details will be discusses in Section 3.3.1.

3.2 Event Selection

The signal considered in this analysis are single top quarks produced in the t-channel decaying to ℓ+jets (i.e. $t \to Wb$ where $W \to \ell\nu$, standing ℓ for e, μ and τ). Events in which the W boson decays into a τ lepton (which happens about 30% [51] of the times in the ℓ+jets channel) are included if the τ lepton decays subsequently to an electron or a muon (i.e. $\tau \to e\nu_e\nu_\tau$ or $\tau \to \mu\nu_\mu\nu_\tau$)[2], since the resulting observed final state is similar to the one encountered if the W boson directly decays into an electron or muon. Anyhow, since two additional neutrinos are produced in the leptonic tau decay, the lepton from the tau decay is softer and infrequently reconstructed. Besides firing the appropriate single-lepton trigger and passing the quality criteria defined in the

[2]Tau leptons decay 17.83% in an electron and 17.41% in a muon accordingly to lepton universality [51]. The remaining 64.76%, taus decay hadronically, and therefore may be identified as a jet.

Good Run List (GRL), additional event quality requirements are used to remove mis-reconstructed events and to reject non-collision background events.

The signal event selection in this analysis is done in a two-step procedure. In the first step (which defines the **pre-selection region**), candidate events are selected based on the t-channel signal topology described in Section 2.3. We require one charged lepton (electron or muon), significant $E_{\mathrm{T}}^{\mathrm{miss}}$ and two jets, one of them being b-tagged, in the final state. Additional requirements are applied in a second step (which defines the **selection region**) to further isolate the t-channel signal events from background contamination.

In addition, two alternative event selections are used to define two **control regions** where a given background contribution ($t\bar{t}$/W+jets) is the dominant process in order to evaluate the good modelling of the data by the MC simulated predictions.

3.2.1 Event Preselection Region

This analysis requires exactly one tight and isolated charged lepton (electron or muon) with transverse momentum $p_{\mathrm{T}}(\ell) > 30$ GeV and pseudorapidity $|\eta| < 2.5$. In order to reduce the $t\bar{t}$ dilepton background, events containing an additional non-isolated lepton, identified with less stringent criteria (loose lepton) and with a p_{T} threshold lowered to 10 GeV, are rejected. Exactly one b-tagged jet with $|\eta| < 2.5$ and exactly one untagged jet with $|\eta| < 4.5$ are required, both with $p_{\mathrm{T}} > 30$ GeV. Additionally, in order to remove some mis-modelling in the transition region between the central and forward hadronic calorimeters, the p_{T} threshold is raised to 35 GeV for the jets within $2.7 < |\eta| < 3.5$. The second b-quark coming from gluon splitting as shown in Figure 27(b) can result in an additional b-tagged jet. This additional jet generally has a softer p_{T} spectrum and a broader η distribution compared to the b-tagged jet produced in the top-quark decay [18]. It is often not detected in the experiment and is thus not required in the event selection. The magnitude of the missing transverse momentum must be $E_{\mathrm{T}}^{\mathrm{miss}} > 35$ GeV.

Two additional multijet background rejection criteria are applied. First, the transverse mass of the lepton–$E_{\mathrm{T}}^{\mathrm{miss}}$ system,

$$m_{\mathrm{T}}(\ell E_{\mathrm{T}}^{\mathrm{miss}}) = \sqrt{2p_{\mathrm{T}}(\ell)E_{\mathrm{T}}^{\mathrm{miss}}\left(1 - \cos\Delta\phi(p_{\mathrm{T}}(\ell), E_{\mathrm{T}}^{\mathrm{miss}})\right)}, \tag{66}$$

is required to be larger than 60 GeV. In the previous expression, $\Delta\phi\left(p_{\mathrm{T}}(\ell), E_{\mathrm{T}}^{\mathrm{miss}}\right)$ is the difference in azimuthal angle between the p_{T} of the lepton and the $E_{\mathrm{T}}^{\mathrm{miss}}$. Secondly, a multi-jet veto, which has a more stringent isolation cut on the lepton p_{T}, is applied to events in which the lepton and leading jet, j_1, are back-to-back:

$$p_{\mathrm{T}}(\ell) > 50\left(1 - \frac{\pi - |\Delta\phi(j_1, \ell)|}{\pi - 1}\right)\ GeV \tag{67}$$

where $\Delta\phi(j_1, \ell)$ is the difference in azimuthal angle between the lepton p_{T} and the leading jet in p_{T}. Thus, the closer the jet and the lepton are, the less stringent the requirement is for the lepton to be isolated. This is to further reduce the multi-jet contamination on the low-p_{T} leptons [18]. The mass of the lepton–b-jet system, $m_{\ell b}$, is required to be lower than 155 GeV, to exclude events in which the top quark of the t-channel signal process is off-shell.

This set of preselection requirements defines the so-called pre-selection region. In this region, the expected contribution of the t-channel signal process is about 13% while for the two main backgrounds their contributions are 38% for the $t\bar{t}$ process and 33% for W+heavy-jets (the contribution of W+light-jets is just 2%). The contribution of all processes is shown in Figure 30(a).

3.2.1.1 Event Selection In the Signal Region

In addition to the signal event pre-selection, further discrimination between single top-quark t-channel events and background events is achieved by applying additional criteria listed below. For some requirements of these criteria, the reconstruction of the top quark (denoted as $\ell E_{\mathrm{T}}^{\mathrm{miss}} b$) is needed. The method to reconstruct a top quark in data and MC events is identical to the one described in Section 3.1.3. The additional selection criteria are:

- The reconstructed mass of the top quark, $m_{\ell E_{\mathrm{T}}^{\mathrm{miss}} b}$, is required to be within 120.6–234.6 GeV, to also reject background events from processes not involving top quarks.
- A "trapezoidal" requirement is also imposed in order to reject more background events, which have leptons in the forward region in events with central reconstructed top-quarks. This requirements is:

  $$\eta_j < (4\ \eta_{\ell E_{\mathrm{T}}^{\mathrm{miss}} b} + a) \cap \eta_j > (4\ \eta_{\ell E_{\mathrm{T}}^{\mathrm{miss}} b} - a) \cap \eta_j > (0.44\ \eta_{\ell E_{\mathrm{T}}^{\mathrm{miss}} b} + b) \cup \eta_j < (0.44\ \eta_{\ell E_{\mathrm{T}}^{\mathrm{miss}} b} - b),$$

  where parameters a and b are 10 and 2, respectively, and j represents the spectator jet.

- The mass of the spectator jet–top-quark system, $m_{j\ell E_{\mathrm{T}}^{\mathrm{miss}}b}$, is required to be greater than 320 GeV, to reject also background events from processes not involving top quarks.
- The scalar sum of the p_{T} of all final-state objects, H_{T}, must be larger than 190 GeV, since the H_{T} distributions of the backgrounds peak at lower values than the t-channel signature.

These selection requirements optimize the expected signal significance at $\sqrt{s} = 13$ TeV, taking into account the main systematic uncertainties. These criteria and the basic event selection together define the t-channel signal region of the analysis.

The expected contribution of the t-channel signal process in the signal region is about 47% while for the two main backgrounds their contributions are 26% for the $t\bar{t}$ process and 17% for W+heavy-jets (the contribution of W+light-jets is just $< 1\%$). The contribution of all processes is shown in Figure 30(b).

3.2.2 Event Selection In the Control Regions

Two specific background–enriched control regions are defined in order to estimate the contributions of the most important background processes in the t-channel signal region by computing scale factors for the overall normalization. These two specific background–enriched regions are:

- A control region enriched in $t\bar{t}$ events is defined by considering pre-selection events though requiring two b-tagged jets (i.e. no light-flavour jets). In this control region, the $t\bar{t}$ contribution is expected to represent 74% of the total expectation, being by far the dominant process. The expected contributions of the signal process and W+heavy-jets are just about 7% and 8%, respectively. All contributions are shown in Figure 30(c).
- An enriched control region in W+jets events is defined in order to control the modelling of the W+jets background. This control region has a similar W+jets flavour composition as the signal region (in terms of W+light-jets and W+heavy-jets contribution). Events in this control region are selected by considering the preselection criteria and selecting any event that failed to fulfill the requirements of the signal selection shown in Section 3.2.1.1. Therefore, this region is also referred to as the "anti-selection region". The fraction of W+heavy-jets events is about 35% of the total expectation. The expected contribution of the signal process is about 10% and the contribution of the $t\bar{t}$ is about 39%. All contributions are shown in Figure 30(d).

In Table 9 summarises the selection criteria for defining the preselection and signal regions and the the two control regions used in this analysis.

Preselection region	Signal region	$t\bar{t}$ control region	W+jets control region
=1 charged tight lepton ($p_{\mathrm{T}} > 30$ GeV and $\|\eta\| < 2.5$)			
Veto secondary low-p_{T} charged loose leptons ($p_{\mathrm{T}} > 10$ GeV and $\|\eta\| < 2.5$)			
=2 jets ($p_{\mathrm{T}} > 30$ GeV and $\|\eta\| < 4.5$; $p_{\mathrm{T}} > 35$ GeV within $2.7 < \|\eta\| < 3.5$)			
$E_{\mathrm{T}}^{\mathrm{miss}} > 35$ GeV			
$m_{\mathrm{T}}(\ell E_{\mathrm{T}}^{\mathrm{miss}}) > 60$ GeV			
$p_{\mathrm{T}}(\ell) > 50 \left(1 - \frac{\pi - \|\Delta\phi(j_1,\ell)\|}{\pi - 1}\right)$ GeV			
=1 b-jet ($\|\eta\| < 2.5$; 60%WP)	=2 b-jet ($\|\eta\| < 2.5$; 60%WP)	=1 b-jet ($\|\eta\| < 2.5$; 60%WP)	
	$m_{\ell b} < 153$ GeV		$m_{\ell b} > 153$ GeV or
	$m_{\ell E_{\mathrm{T}}^{\mathrm{miss}} b} \in [120.6, 234.6]$ GeV		$m_{\ell E_{\mathrm{T}}^{\mathrm{miss}} b} \notin [120.6, 234.6]$ GeV or
	trapez. requirement		veto trapez. requirement or
	$m_{j\ell E_{\mathrm{T}}^{\mathrm{miss}} b} > 320$ GeV		$m_{j\ell E_{\mathrm{T}}^{\mathrm{miss}} b} < 320$ GeV or
	$H_{\mathrm{T}} > 190$ GeV		$H_{\mathrm{T}} < 190$ GeV

Table 9: Summary of the selection criteria for defining the preselection and signal regions and the two control regions.

3.2.3 Contribution Of The Signal And Background Processes In The Different Regions

As already mentioned above, Figure 30 shows the donut charts with the expected contribution of the t-channel signal and different background processes in the pre-selection and signal regions and the two control regions, where electron and muon channels are merged together. Here, the term "pre-fit" means that these donut charts are built from the event yields of the MC simulated signal and background processes where each process is normalised to 139.0 fb^{-1} using its corresponding theoretical production cross-section. Very small differences are shown for the relative expected contribution of the different processes between the electron and muon channels.

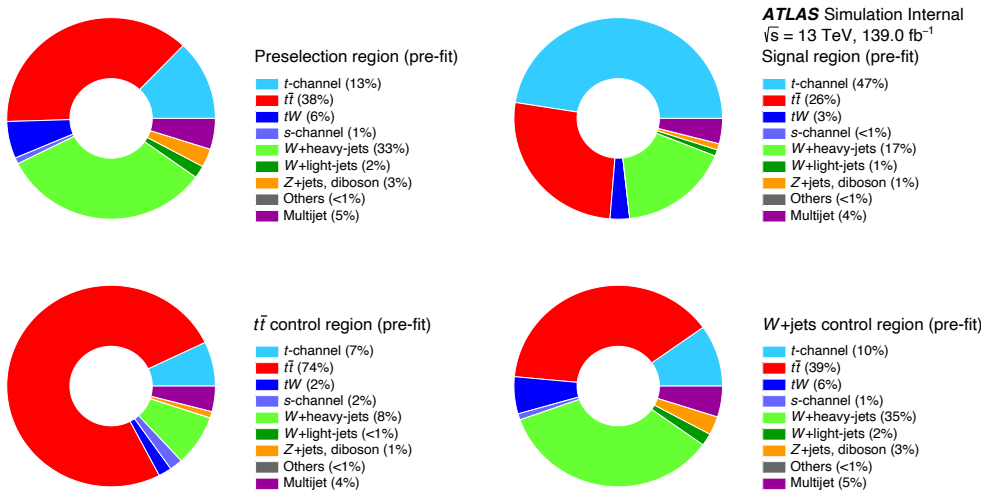

Figure 30: Donut charts showing the relative pre-fit expected contribution of the t-channel signal and different background processes in the pre-selection region, signal region, and in the $t\bar{t}$ and W+jets control regions. Electrons and muons are merged together.

3.3 Background Estimation

The main backgrounds in the t-channel signal region are $t\bar{t}$ production, W-boson production in association with jets and multijet events. Smaller backgrounds originate from aforementioned contributions such as single top-quark s-channel and associated tW production, Z boson production in association with jets, from diboson production and so on. The signal and background contributions are normalized to their theoretical cross-section predictions, except for $t\bar{t}$ and W+jets backgrounds whose normalization is left floating in the template fit discussed in Section 3.5. The normalization of the multijet background is obtained from data-driven techniques. The kinematic distributions are taken from the MC simulation for all signal and background processes except for the multijet events for which either MC simulation or data-derived templates are used.

3.3.1 Multijet Estimation

A significant source of background in hadronic collisions is the QCD-induced multijet production where either a hadronic jet or a non-prompt lepton from the decay of a hadron or electrons from photon conversions are mis-identified as prompt isolated leptons (all these cases are known as fake leptons). The multijet background is characterized by a cross-section of several orders of magnitude above top-quark and vector-boson productions. Considering this overwhelming production rate and a sizeable probability of jet mis-identification or fake leptons, this background turns out to be a non-negligible contribution to the selected t-channel signal events. For the electron channel, a dedicated selection is imposed on MC simulated di-jet events (i.e. jets, γ+jet, W/Z and $t\bar{t}$ events, with EM jet $p_{\mathrm{T}} > 17$ GeV), in order to enrich events with jets that are likely to resemble an electron with a detector signature close to selected "signal" candidate electrons. Such a jet, resembling a lepton, is required to have $E_{\mathrm{T}} > 25$ GeV and the same coverage in η as the selected leptons. The fraction of the energy of the jet deposited in the EM calorimeter, f_{EM}, has to be between 0.8 and 1.0. By demanding that at least four tracks are found in the jet, the probability to select converted photons is reduced. The event is accepted if exactly one "jet–electron" is found. Therefore, such method is called *jet–electron* method to estimate the shape of the multijet contributions in all regions. Table 10 summarizes these applied selections. For the muon channel, event samples are fully derived from data, where a real high-p_{T} muon occurs within a jet due to the ℓ+jets (semileptonic) decay of a heavy-flavour hadron and this muon is mis-measured as an isolated one originating from a W boson decay. Thus, some of the muon identification cuts are inverted or changed, correspondingly, called the *anti-muon* method, resulting in a sample that is highly enriched with muons from multijet events. The resulting sample contains only a small amount of prompt muons from the decays of Z or W bosons.

A binned likelihood fit is performed on the $E_{\mathrm{T}}^{\mathrm{miss}}$ (electron channel) and the $m_{\mathrm{T}}(\ell E_{\mathrm{T}}^{\mathrm{miss}})$ (muon channel) distributions separately for two different multijet-enriched regions to obtain the scale factor of the multijet contribution. These two multijet-enriched regions are defined as the preselection region and the $t\bar{t}$ control region but leaving out in both regions the $E_{\mathrm{T}}^{\mathrm{miss}} > 35$ GeV cut (electron channel) and the $m_{\mathrm{T}}(\ell E_{\mathrm{T}}^{\mathrm{miss}}) > 60$ GeV cut (muon channel). The additional multijet rejecting requirement (i.e. the isolation cut on the lepton p_{T} shown by Eq. (67)) is left out as well.

Variable	Selection
Transverse energy of jet	$E_{\mathrm{T}} > 25$ GeV
η of jet	$\lvert\eta\rvert < 2.47$
EM fraction	$0.8 < f_{\mathrm{EM}} < 1.0$

Table 10: Selection critera imposed on a MC simulated di-jet event sample in order to enrich events with jets that are likely to resemble an electron with a detector signature close to selected "signal" candidate electrons.

In the multijet-enriched $t\bar{t}$ control region, the low contribution coming from W+jets processes are kept fixed to their theoretical predictions. In the multijet-enriched preselction region, both W+jets and top-quark processes contributions are fitted. Figures 31-32 and Figures 33-34 show the full shapes of the $E_{\mathrm{T}}^{\mathrm{miss}}$ and the $m_{\mathrm{T}}(\ell E_{\mathrm{T}}^{\mathrm{miss}})$ when the $E_{\mathrm{T}}^{\mathrm{miss}} > 35$ GeV cut (electron channel) and the $m_{\mathrm{T}}(\ell E_{\mathrm{T}}^{\mathrm{miss}}) > 60$ GeV cut (muon channel) are removed in the multijet-enriched regions, in the multijet-enriched pre-selection region and multijet-enriched $t\bar{t}$ control region, respectively. The differences in the shapes constitute a robustness test of the fit and it can be seen that the shapes of the multijet background are clearly different to those from the W+jets and the $t\bar{t}$ backgrounds for the fitted variables ($E_{\mathrm{T}}^{\mathrm{miss}}$ for the electron channel and $m_{\mathrm{T}}(\ell E_{\mathrm{T}}^{\mathrm{miss}})$ for the muon channel). For the electron channel, as real electrons with a pseudorapidity falling in the EM crack region cannot be faked by the jet-electron model, the multijet normalization estimates are derived separately for events with a central jet-electron ($|\eta| < 1.5$) and for events with a forward jet-electron ($|\eta| > 1.5$). Although the multijet estimates are extracted separately for the electrons and muon channels, the fitted W+jets and top-quark scale factors are constrained to be the same for both channels. The obtained normalization factors, associated with the W+jets and the merged top-quark contributions, are reported in Table 11 with their statistical uncertainties. These normalisation factors do not change when relaxing the constraint of 20% to 50% for the W+jets contribution.

The number of multijet events containing exactly one jet-electron (either central or forward)

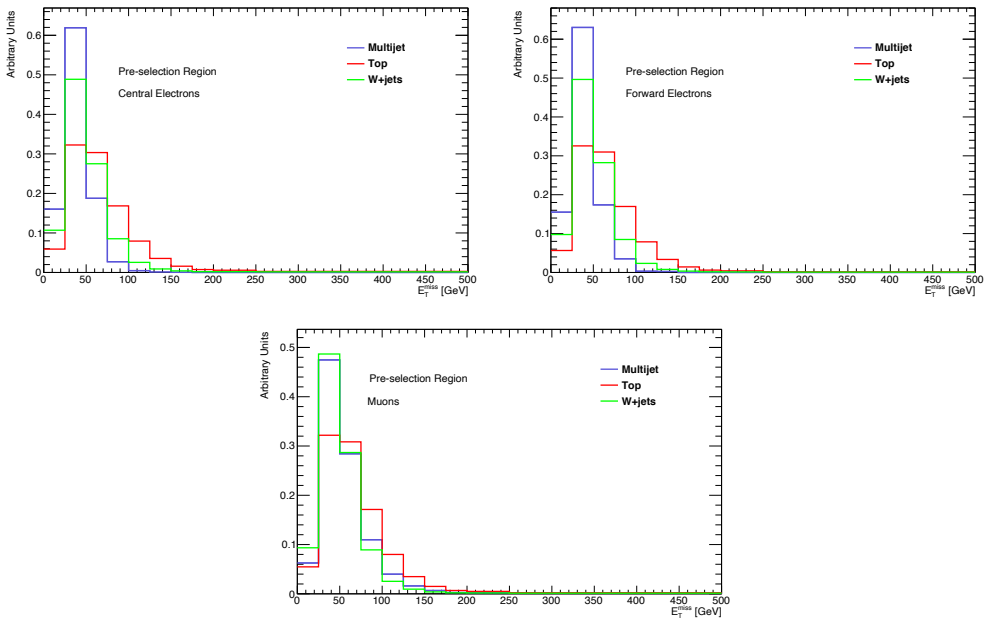

Figure 31: Distributions of the $E_{\mathrm{T}}^{\mathrm{miss}}$ in the multijet-enriched preselection region for the central electron channel, the forward electron channel and the muon channel. The distributions are normalised to the total number of events in order to compare the shapes of the MC templates. The bottom figure shows that the shape of the multijet and W+jets processes is almost the same and therefore there would be no discrimination power between these processes.

or exactly one anti-muon, estimated from the likelihood fit of the $E_{\mathrm{T}}^{\mathrm{miss}}$ distribution in the electron channel and the $m_{\mathrm{T}}(\ell E_{\mathrm{T}}^{\mathrm{miss}})$ distribution in the muon channel, are shown in Table 12 for all regions defined in Section 3.2. The normalization factors obtained from the multijet-enriched pre-selection region are used in the pre-selection and signal regions as well as in the W+jets control region while the normalization factors obtained from the multijet-enriched $t\bar{t}$ control region are just used in the $t\bar{t}$ control region. The fitted distributions of the $E_{\mathrm{T}}^{\mathrm{miss}}$ in the electron channel and the $m_{\mathrm{T}}(\ell E_{\mathrm{T}}^{\mathrm{miss}})$ in the muon channel are shown in Figures 35-36 for the preselection region and for the $t\bar{t}$ control region, respectively. The distributions associated with the central and forward jet-electrons are both fitted and therefore shown separately. The multijet background is renormalised with the normalisation factors derived from the likelihood fit of the data distribution of the $E_{\mathrm{T}}^{\mathrm{miss}}$ (electron

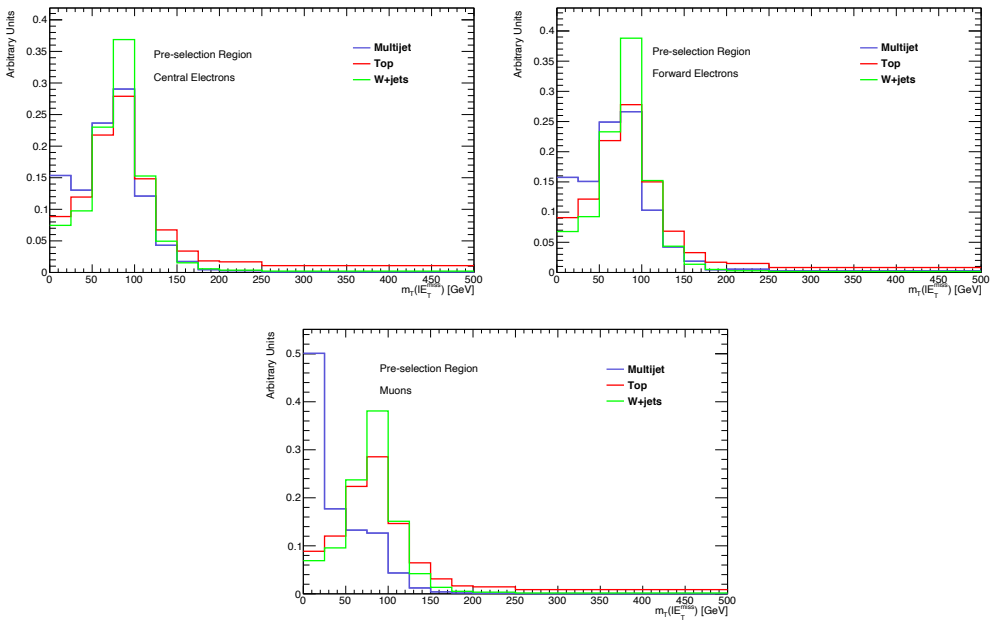

Figure 32: Distributions of the $m_{\mathrm{T}}(\ell E_{\mathrm{T}}^{\mathrm{miss}})$ in the multijet-enriched preselection region for the central electron channel, the forward electron channel and the muon channel. The distributions are normalised to the total number of events in order to compare the shapes of the MC templates. The bottom figure shows a good discrimination power between the multijet and W+jets processes given the large differences in their shapes.

channel) and the $m_{\mathrm{T}}(\ell E_{\mathrm{T}}^{\mathrm{miss}})$ (muon channel). The normalisation factors reported in Table 11 are not propagated to the next steps of the analysis (these are just used to have a realistic estimate of the multijet normalisation).

The fitting methods suffer from systematic uncertainties mainly due to the modelling of the shapes of the fit variables by the different templates. Studies to assess the effect of these uncertainties on the final estimates are based on the use of alternative fit variables or on the use of alternative simulated event samples for the most important background contributing processes. In particular, by comparing the fit results in the multijet-enriched preselection region and in the multijet-enriched $t\bar{t}$ control region (i.e. without the $E_{\mathrm{T}}^{\mathrm{miss}}$ or $m_{\mathrm{T}}(\ell E_{\mathrm{T}}^{\mathrm{miss}})$ cut and without the additional multijet rejecting cut) with the results obtained by fitting an alternative distribution (i.e. the

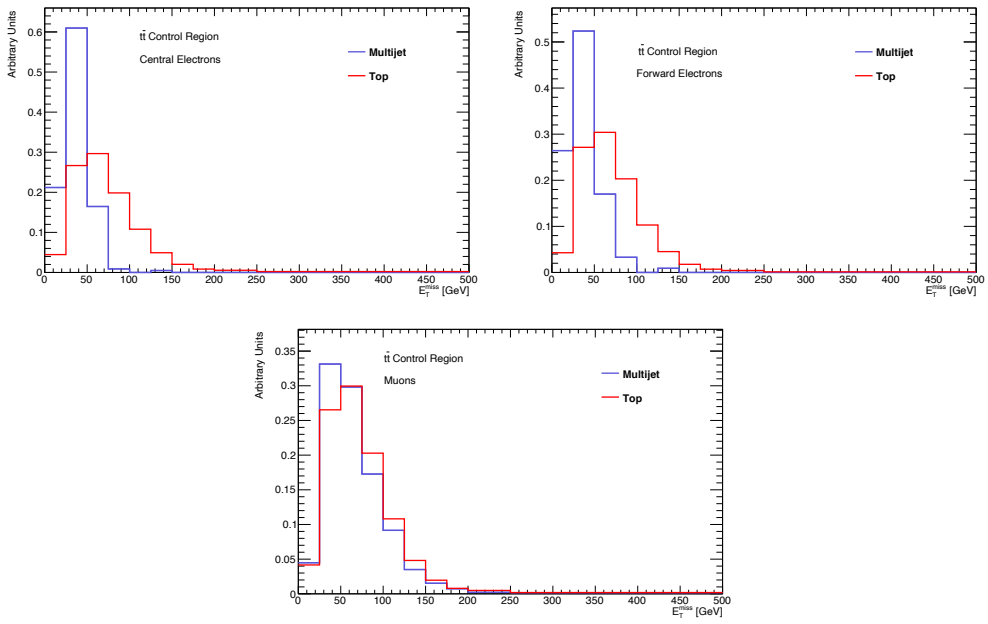

Figure 33: Distributions of the $E_{\mathrm{T}}^{\mathrm{miss}}$ in the multijet-enriched $t\bar{t}$ control region for the central electron channel, the forward electron channel and the muon channel. The distributions are normalised to the total number of events in order to compare the shapes of the MC templates. The bottom figure shows that the shape of the multijet and W+jets processes is almost the same and therefore there would be no discrimination power between these processes.

$m_{\mathrm{T}}(\ell E_{\mathrm{T}}^{\mathrm{miss}})$ distribution for both the electron and the muon channels or the $E_{\mathrm{T}}^{\mathrm{miss}}$ distribution for both the electron and the muon channels) an uncertainty of 100% is obtained for the fake-electron normalization and of 100% for the fake-muon normalization. The choice of MC generator for $t\bar{t}$ processes leads to uncertainties of 50% for fake-electrons and 20% for fake-muons. These studies, together with the comparison of the predictions with data in different distribution shapes, indicate that a systematic uncertainty of 100% in the normalisation of the multijet background is representative of the overall impact of these sources. Such value is therefore used in both channels and in all regions.

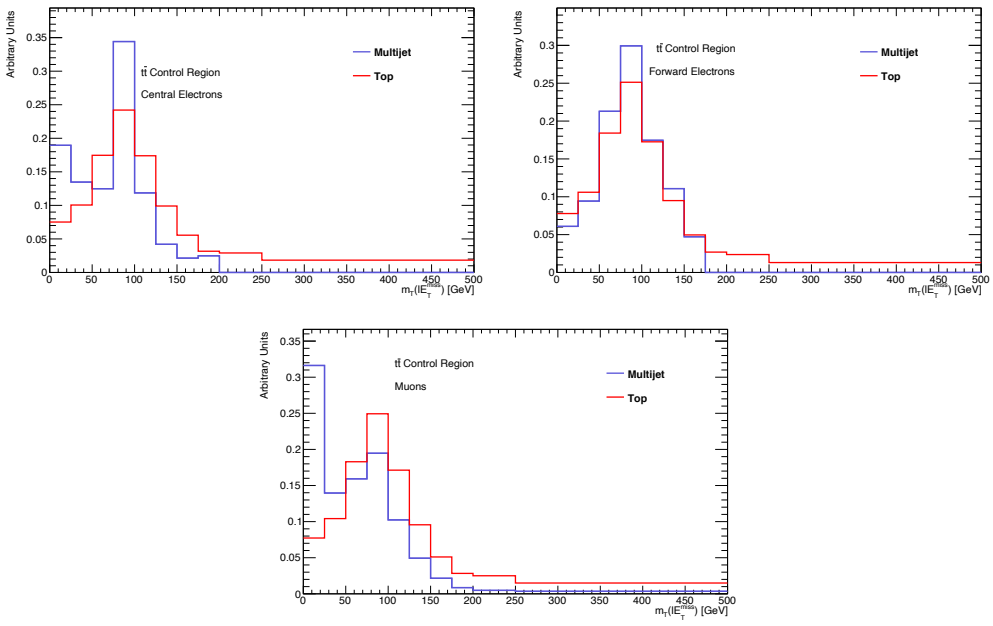

Figure 34: Distributions of the $m_{\mathrm{T}}(\ell E_{\mathrm{T}}^{\mathrm{miss}})$ in the multijet-enriched $t\bar{t}$ control region for the central electron channel, the forward electron channel and the muon channel. The distributions are normalised to the total number of events in order to compare the shapes of the MC templates. The bottom figure shows a good discrimination power between the multijet and W+jets processes given the large differences in their shapes.

3.4 Event Yields and Kinematic Distributions

This section shows the expected and observed event yields in the pre-selection and signal regions and the two control regions. Additionally the kinematic distributions in the signal region as well as the angular distributions in the signal and control regions are shown. For completeness, Appendix B shows additional information, as yields split into the electron and muons channels and for the top-quark and top-anti-quark channels or kinematic and angular distributions in the pre-selection region and in the two control regions.

Process	Fakes-enriched $t\bar{t}$ CR	Fakes-enriched PR
W+jets	fixed	1.320 ± 0.009
$t\bar{t}$,t-channel,tW,s-channel	1.014 ± 0.004	0.919 ± 0.005

Table 11: Normalisation factors extracted for the W+jets and merged top-quark contributions from the maximum-likelihood fit of the distributions of the $E_{\mathrm{T}}^{\mathrm{miss}}$ (electron channel) and $m_{\mathrm{T}}(\ell E_{\mathrm{T}}^{\mathrm{miss}})$ (muon channel) observed in the multijet-enriched $t\bar{t}$ Control Region (CR) and in the multijet-enriched Pre-selection Region (PR). The uncertainties correspond to the statistical uncertainties provided from the likelihood fit.

Channel	W+jets control region	$t\bar{t}$ control region	Preselection region	Signal region
Electron	29945	3372	32071	2126
Muon	12207	2113	13439	1233

Table 12: Multijet event yields estimated in the electron and muon channel with the jet-electron and anti-muon models. They are given for the W+jets and $t\bar{t}$ control regions as well as for the preselection and signal regions.

3.4.1 Event Yields

In Section 3.2.3, pie charts showing the relative expected contributions of the t-channel signal and their different background processes in the pre-selection and signal regions and in the two control regions are shown in Figure 30. The charts do not take into account the re-adjustment of $t\bar{t}$, W+jets cross sections that occur in the final fit, described in Section 3.5. Here, the total expected and observed "pre-fit" event yields for the pre-selection and signal regions and the $t\bar{t}$ and W+jets control regions are shown in Table 13 for the combined electron and muon channels, where the uncertainties are statistical uncertainties only. Additionally, the signal-to-background ratio (S/B) and the data-to-expected-MC-events ratio (Data/MC) are also shown for each region.

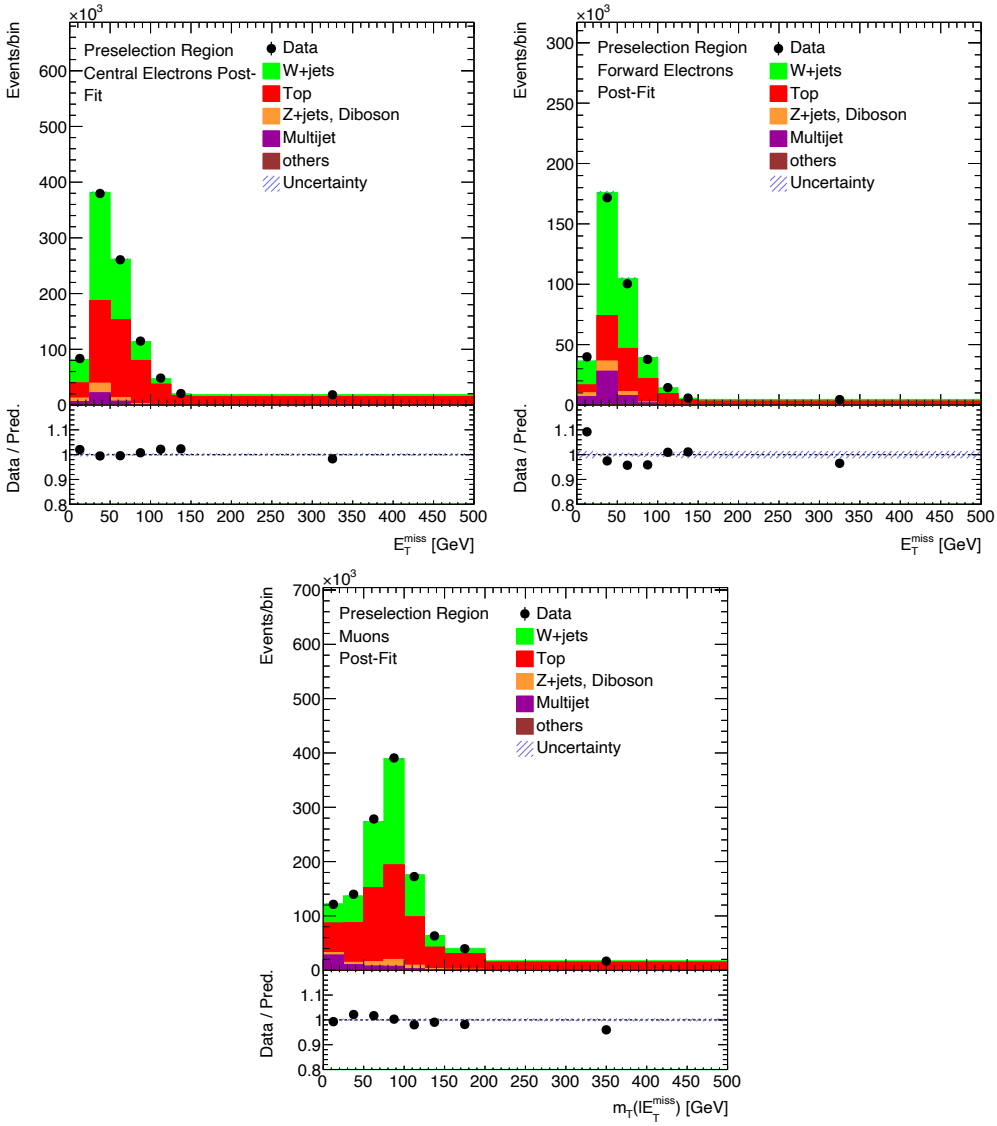

Figure 35: Distributions of the post-fit $E_{\mathrm{T}}^{\mathrm{miss}}$ in the pre-selection region for the central electron channel and the forward electron channel, and distribution of the post-fit $m_{\mathrm{T}}(\ell E_{\mathrm{T}}^{\mathrm{miss}})$ in the pre-selection region for the muon channel. The predicted distributions are re-scaled using the fitted normalisation factors. The uncertainty bands that correspond to the statistical fluctuations together with the top-quark backgrounds and W+jets normalisation uncertainties. The lower plots show the ratio of data to prediction in each bin.

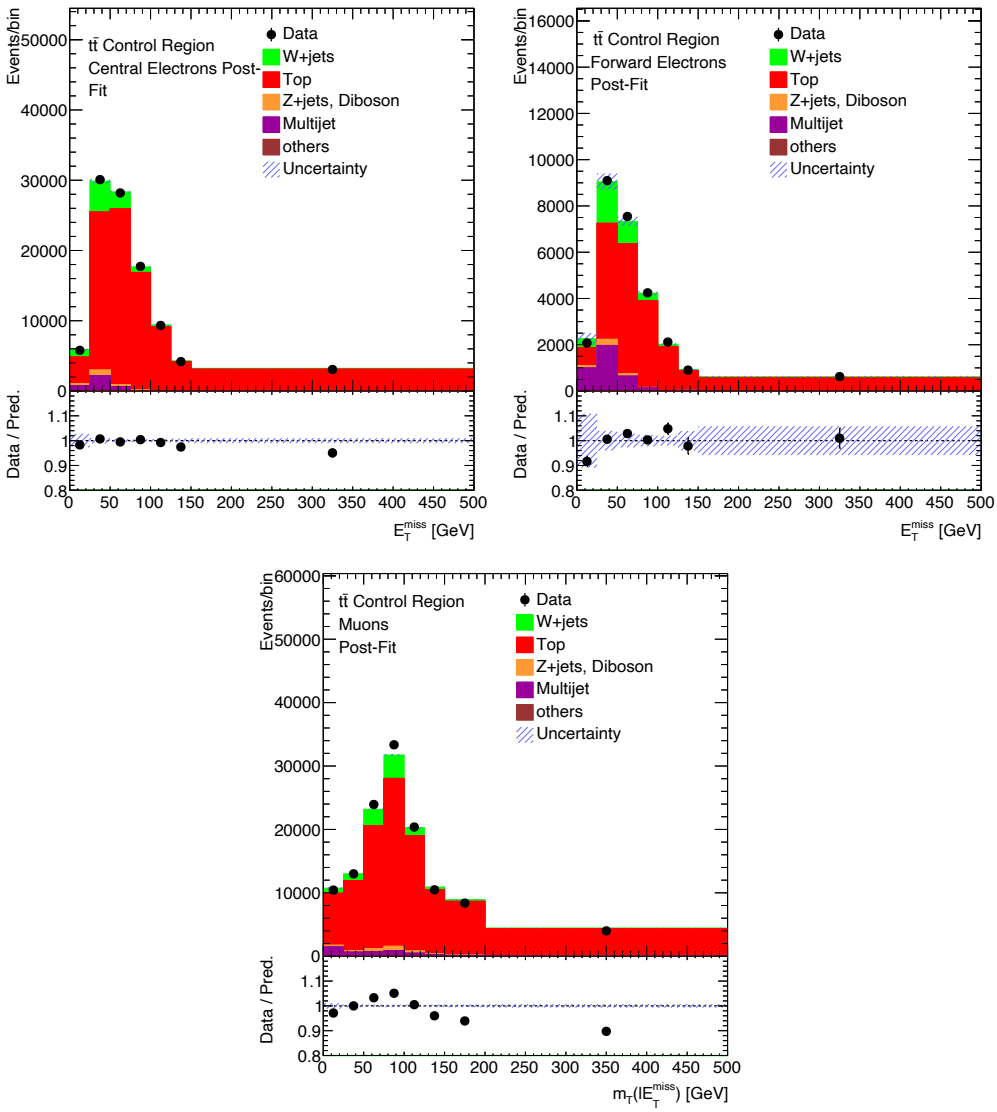

Figure 36: Distributions of the post-fit $E_{\mathrm{T}}^{\mathrm{miss}}$ in the $t\bar{t}$ control region for the central electron channel and the forward electron channel, and distribution of the post-fit $m_{\mathrm{T}}(\ell E_{\mathrm{T}}^{\mathrm{miss}})$ in the $t\bar{t}$ control region for the the muon channel. The predicted distributions are re-scaled using the fitted normalisation factors. The uncertainty bands that correspond to the statistical fluctuations together with the top-quark backgrounds and W+jets normalisation uncertainties. The lower plots show the ratio of data to prediction in each bin.

In Appendix B.1 further detailed pre-fit event yield tables can be found.

Process	Preselection region	Signal region	$t\bar{t}$ control region	W+jets control region
t-channel	218752 ± 259	70601 ± 147	13479 ± 65	148150 ± 213
$t\bar{t}$	633384 ± 314	38544 ± 78	139757 ± 146	594839 ± 304
tW	94267 ± 165	4265 ± 35	4510 ± 36	90002 ± 161
s-channel	8791 ± 17	368 ± 3	3507 ± 11	8424 ± 17
W+heavy-jets	558232 ± 1891	24949 ± 490	15733 ± 160	533284 ± 1826
W+light-jets	32464 ± 1062	1205 ± 228	386 ± 82	31259 ± 1037
Z+jets, diboson	52906 ± 334	2121 ± 68	2617 ± 38	50785 ± 327
Others	528 ± 3	31 ± 1	91 ± 1	497 ± 3
Multijet	88708 ± 1300	6643 ± 283	8266 ± 473	82064 ± 1268
Total expected	1688031 ± 2587	148727 ± 636	188346 ± 533	1539303 ± 2507
Data	1750918 ± 1323	154361 ± 392	188326 ± 433	1596557 ± 1263
S/B	0.15	0.90	0.08	0.11
Data/MC	1.04	1.04	1.00	1.04

Table 13: Pre-fit event yields in the pre-selection and signal regions and in the $t\bar{t}$ control and W+jets control regions for the combined electron and muon channels. The predictions are derived from simulated event samples together with their theoretical cross-section except multijet which normalisation is estimated from a data-driven likelihood fit. No overall normalisation scale factors are considered to compute these event yields. The uncertainties shown are statistical only. Yields and uncertainties of less than 0.5 events appear as zero. Individual predictions are rounded to integers while "Total expected" corresponds to the rounding of the sum of full precision individual predictions. The expected S/B and Data/MC ratios are also given.

3.4.2 Kinematic Distributions In the Signal Region

In this section, kinematic distributions of a selected variables in the signal region are presented. In all these distributions, the electrons and muon channels are combined, as well as the top quarks and anti-quarks. The uncertainty bands shown on the prediction correspond to the uncertainties due to the limited size of the simulated event samples (so-called 'statistical uncertainty') added in quadrature with the data-driven normalization uncertainty of 100% estimated for the multijet

contribution. Figures 37-38 demonstrate the pre-fit kinematic distributions of the p_{T}, η and ϕ in the signal region of the reconstructed spectator jet and b-jet. Figure 39 shows the pre-fit kinematic distributions of the p_{T}, charge, η and ϕ of the lepton. Figure 40 shows the pre-fit kinematic distributions of the $E_{\mathrm{T}}^{\mathrm{miss}}$, $\phi(E_{\mathrm{T}}^{\mathrm{miss}})$, $m_{\mathrm{T}}(\ell E_{\mathrm{T}}^{\mathrm{miss}})$, and the p_{T}, η and ϕ of the reconstructed W boson. Figure 41 shows several pre-fit kinematic distributions of variables that appeared in the event selection criteria, such asH_{T}, $\Delta p_{\mathrm{T}}(W, jb\text{-jet})$, $m_{\ell b}$, $m_{j\ell E_{\mathrm{T}}^{\mathrm{miss}}b}$ and m_{jb}. More distributions can be found in Appendix B.

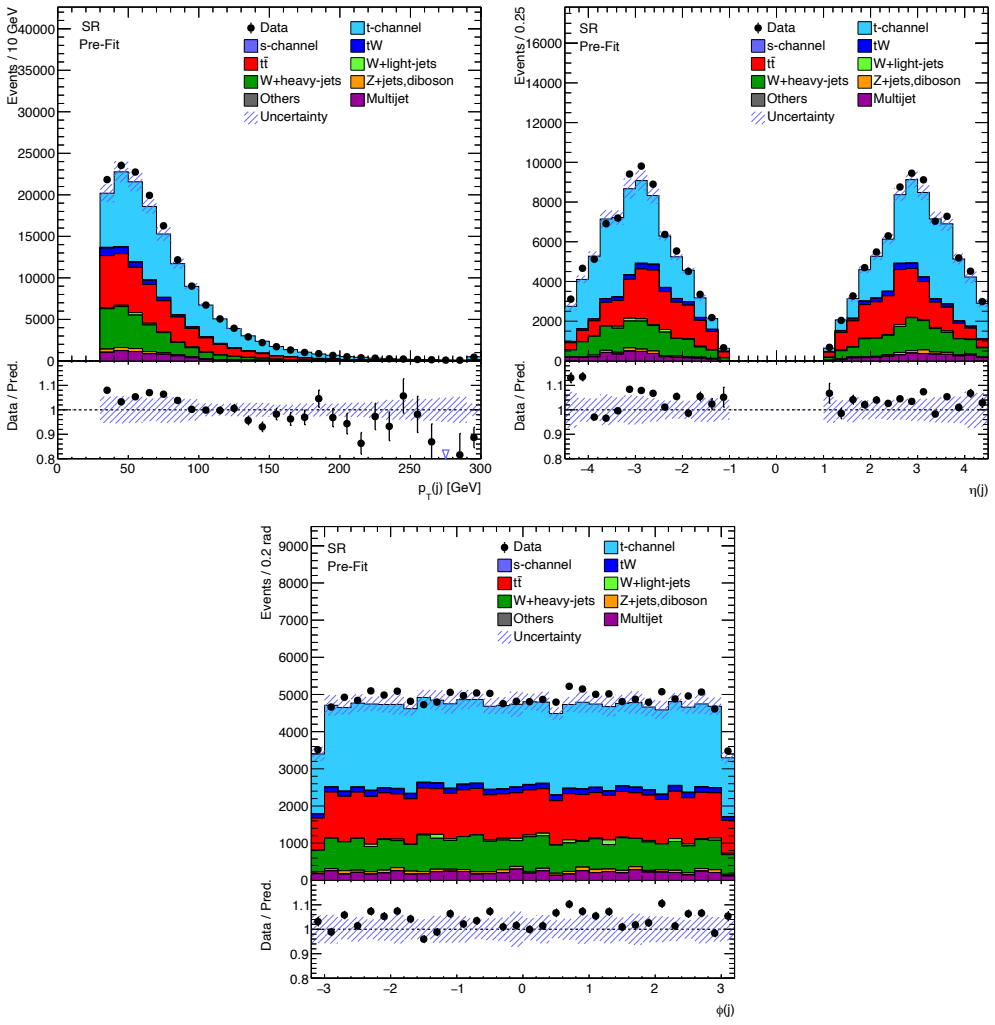

Figure 37: Distributions of the spectator jet p_{T}, η and ϕ in the signal region. The prediction is compared to data, shown as the black points with statistical uncertainties. No overall normalisation scale factors are considered at this stage. The uncertainty bands correspond to the uncertainties due to the size of the simulated event samples added in quadrature with the data-driven normalisation uncertainty of 100% estimated for the multijet contribution. The lower plots show the ratio of data to prediction in each bin.

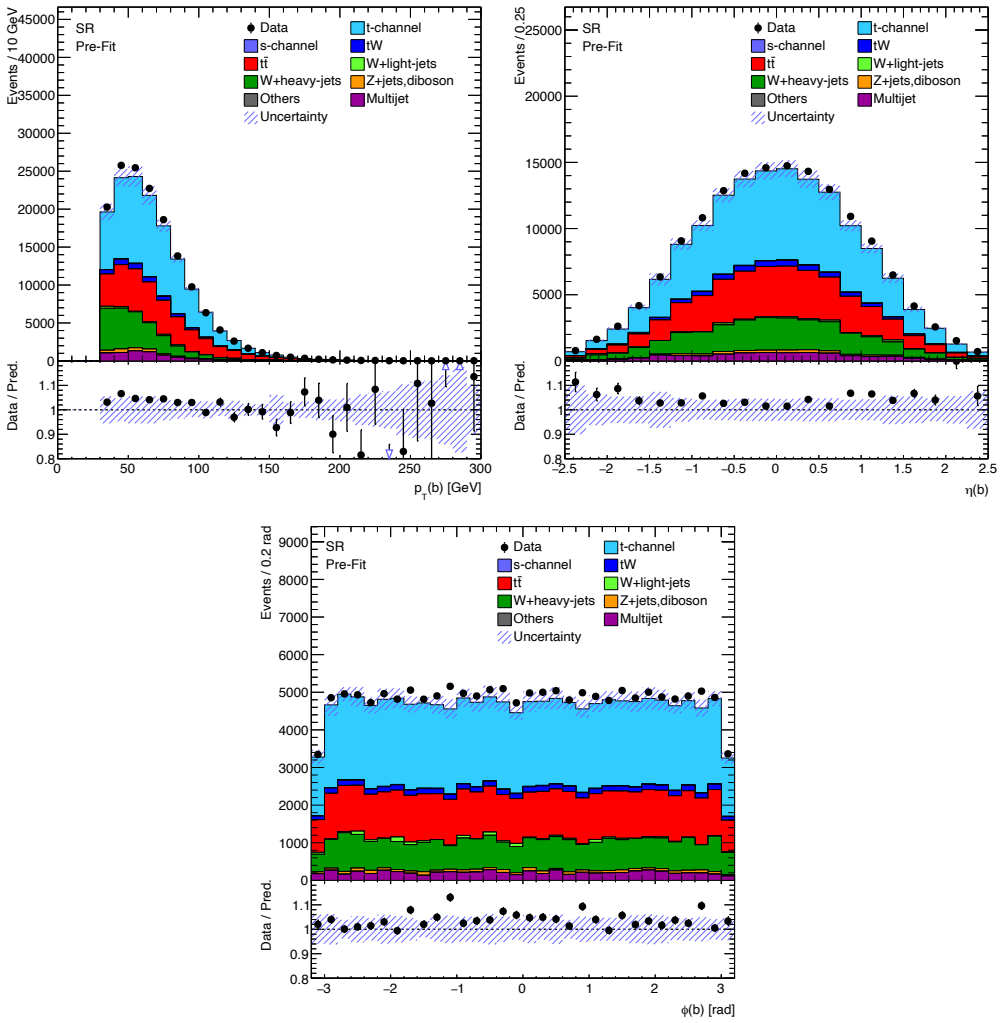

Figure 38: Distributions of the b-jet p_{T}, η and ϕ in the signal region. The prediction is compared to data, shown as the black points with statistical uncertainties. No overall normalisation scale factors are considered at this stage. The uncertainty bands correspond to the uncertainties due to the size of the simulated event samples added in quadrature with the data-driven normalisation uncertainty of 100% estimated for the multijet contribution. The lower plots show the ratio of data to prediction in each bin.

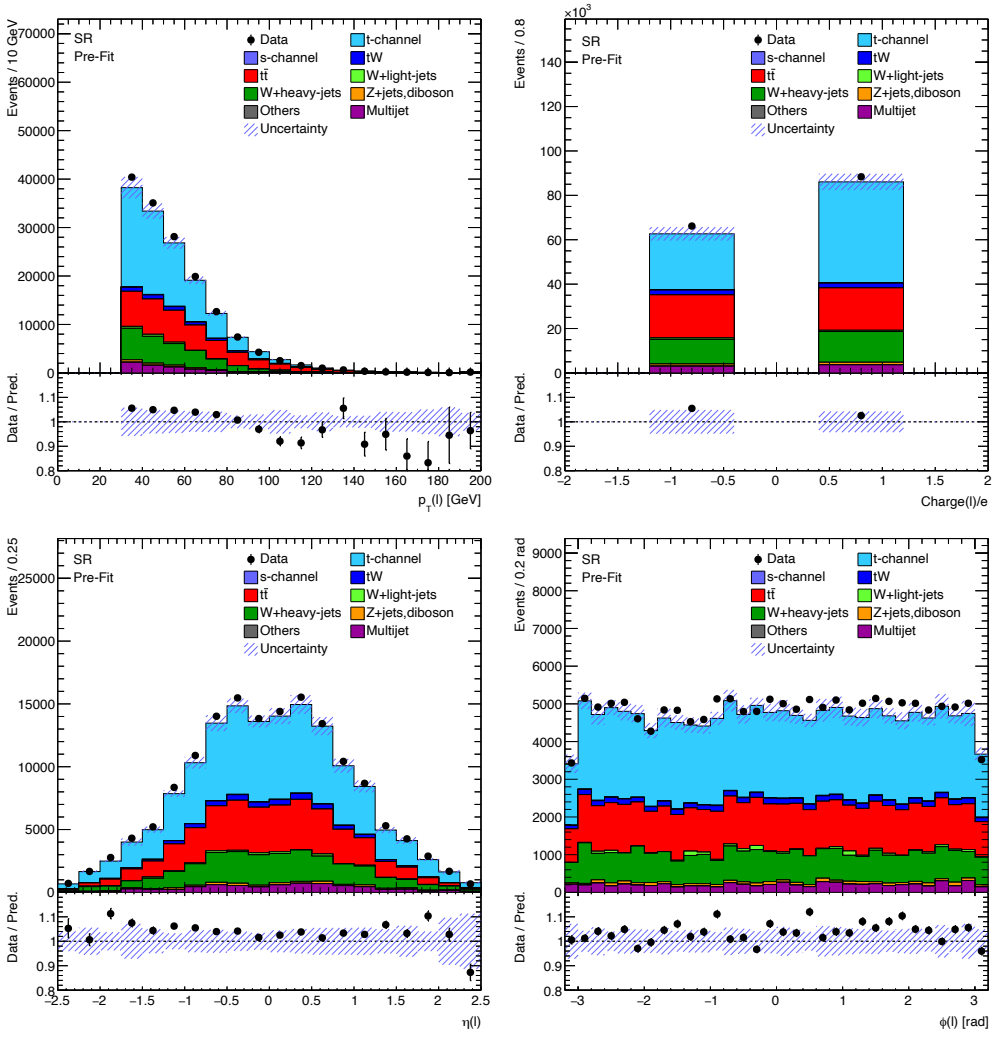

Figure 39: Distributions of the lepton p_{T}, charge, η and ϕ in the signal region. The prediction is compared to data, shown as the black points with statistical uncertainties. No overall normalisation scale factors are considered at this stage. The uncertainty bands correspond to the uncertainties due to the size of the simulated event samples added in quadrature with the data-driven normalisation uncertainty of 100% estimated for the multijet contribution. The lower plots show the ratio of data to prediction in each bin.

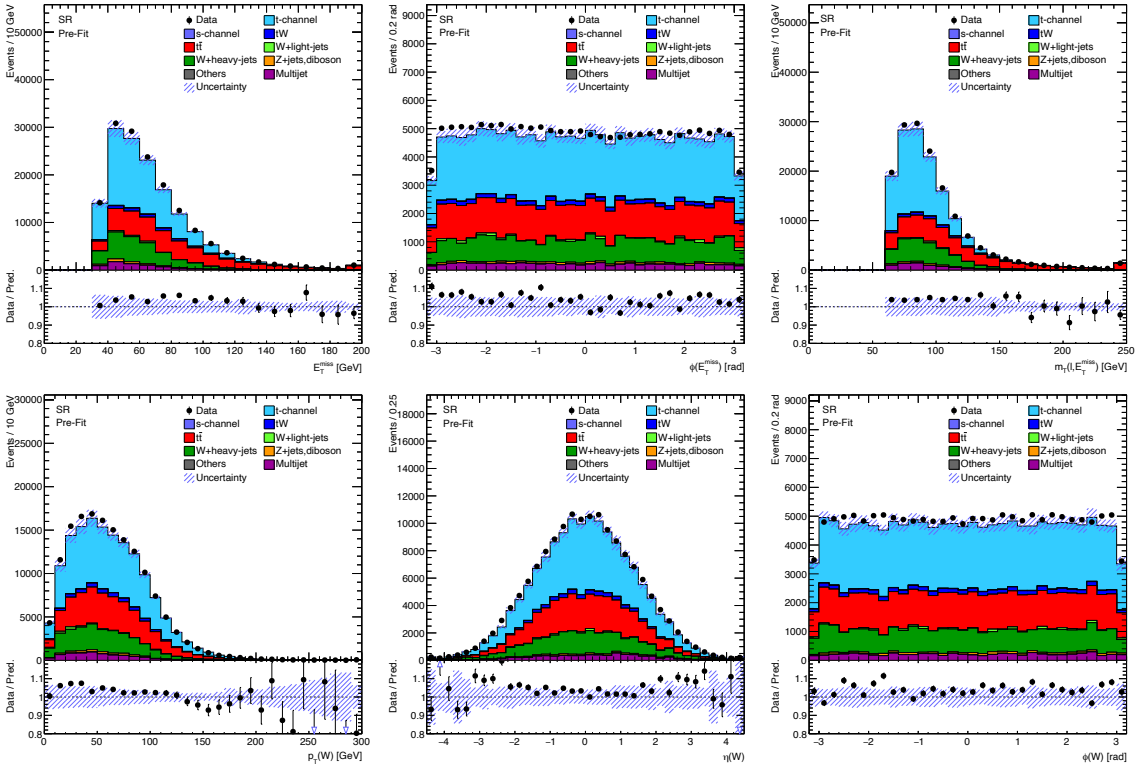

Figure 40: Distributions of the $E_{\mathrm{T}}^{\mathrm{miss}}$, $\phi(E_{\mathrm{T}}^{\mathrm{miss}})$, $m_{\mathrm{T}}(\ell E_{\mathrm{T}}^{\mathrm{miss}})$, as well as, the reconstructed W boson p_{T}, η and ϕ in the signal region. The prediction is compared to data, shown as the black points with statistical uncertainties. No overall normalisation scale factors are considered at this stage. The uncertainty bands correspond to the uncertainties due to the size of the simulated event samples added in quadrature with the data-driven normalisation uncertainty of 100% estimated for the multijet contribution. The lower plots show the ratio of data to prediction in each bin.

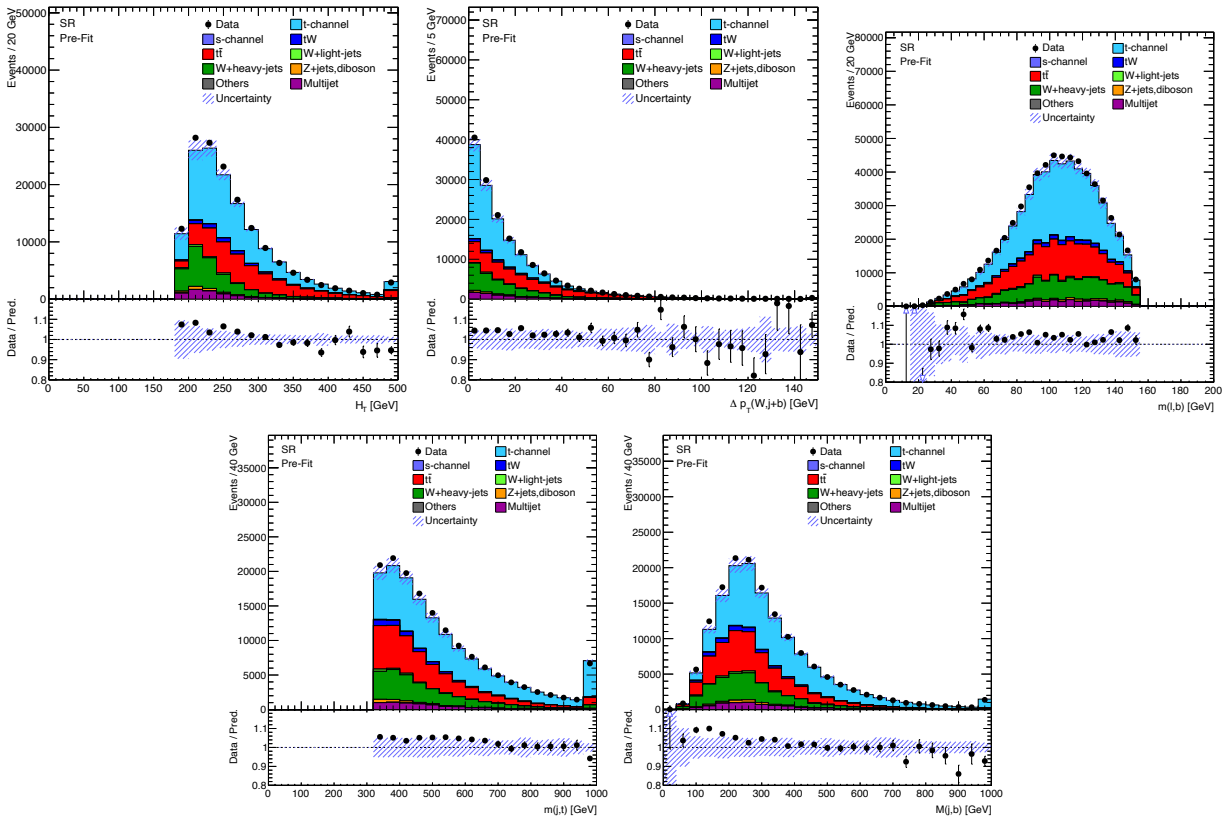

Figure 41: Distributions of H_{T} and $\Delta p_{\mathrm{T}}(W, jb\text{-jet})$, $m_{\ell b}$, $m_{j\ell E_{\mathrm{T}}^{\mathrm{miss}} b}$ and m_{jb} in the signal region. The prediction is compared to data, shown as the black points with statistical uncertainties. No overall normalisation scale factors are considered at this stage. The uncertainty bands correspond to the uncertainties due to the size of the simulated event samples added in quadrature with the data-driven normalisation uncertainty of 100% estimated for the multijet contribution. The lower plots show the ratio of data to prediction in each bin.

3.4.3 Angular Distributions In the Signal And Control Regions

Since this analysis is based upon the angular distributions, a set of plots are generated to visualize the angular observables. Figures 42-44 show the pre-fit angular distributions of $\cos\theta_{\ell x}$, $\cos\theta_{\ell y}$ and $\cos\theta_{\ell z}$ in the signal and control regions.

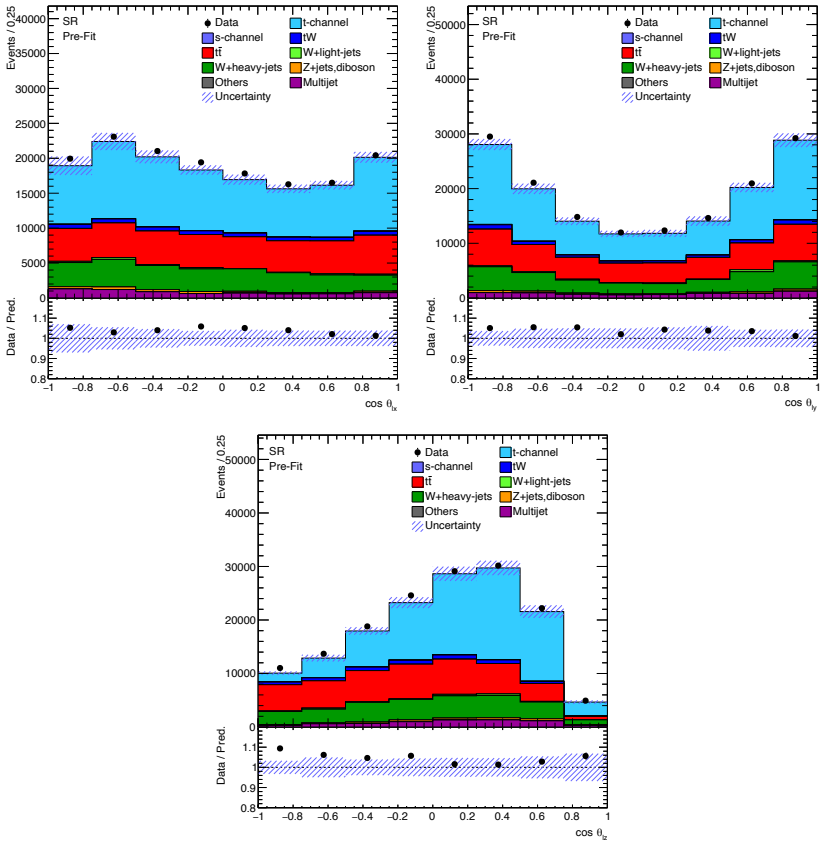

Figure 42: Distributions of $\cos\theta_{\ell x}$, $\cos\theta_{\ell y}$ and $\cos\theta_{\ell z}$ in the signal region. The prediction is compared to data, shown as the black points with statistical uncertainties. No overall normalisation scale factors are considered at this stage. The uncertainty bands correspond to the uncertainties due to the size of the simulated event samples added in quadrature with the data-driven normalisation uncertainty of 100% estimated for the multijet contribution. The lower plots show the ratio of data to prediction in each bin.

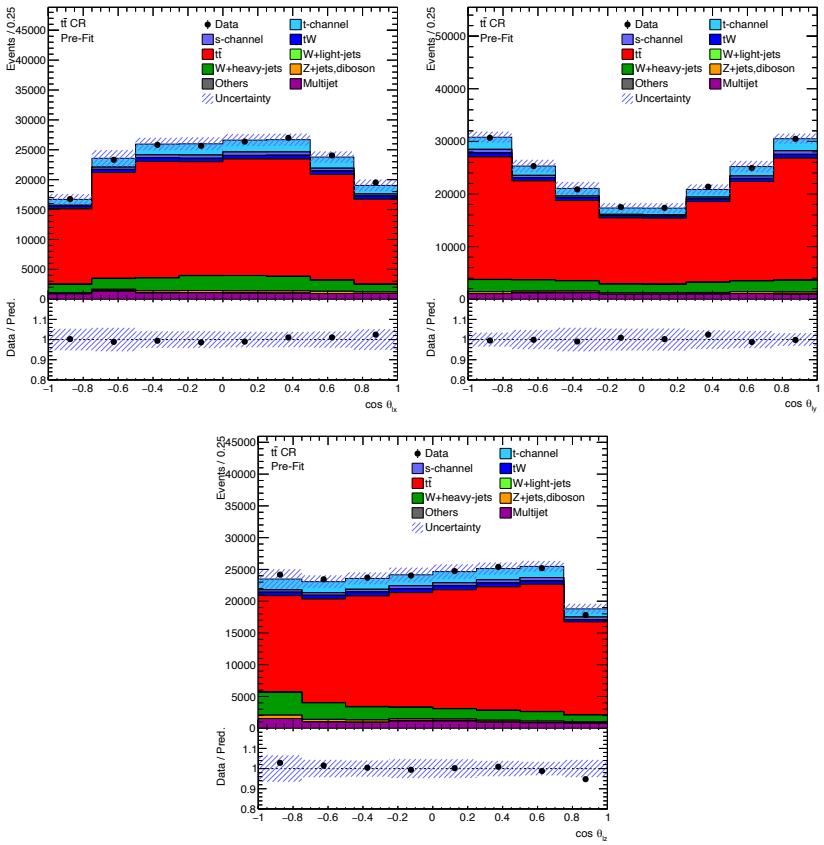

Figure 43: Distributions of $\cos\theta_{\ell x}$, $\cos\theta_{\ell y}$ and $\cos\theta_{\ell z}$ in the $t\bar{t}$ control region. The prediction is compared to data, shown as the black points with statistical uncertainties. No overall normalisation scale factors are considered at this stage. The uncertainty bands correspond to the uncertainties due to the size of the simulated event samples added in quadrature with the data-driven normalisation uncertainty of 100% estimated for the multijet contribution. The lower plots show the ratio of data to prediction in each bin.

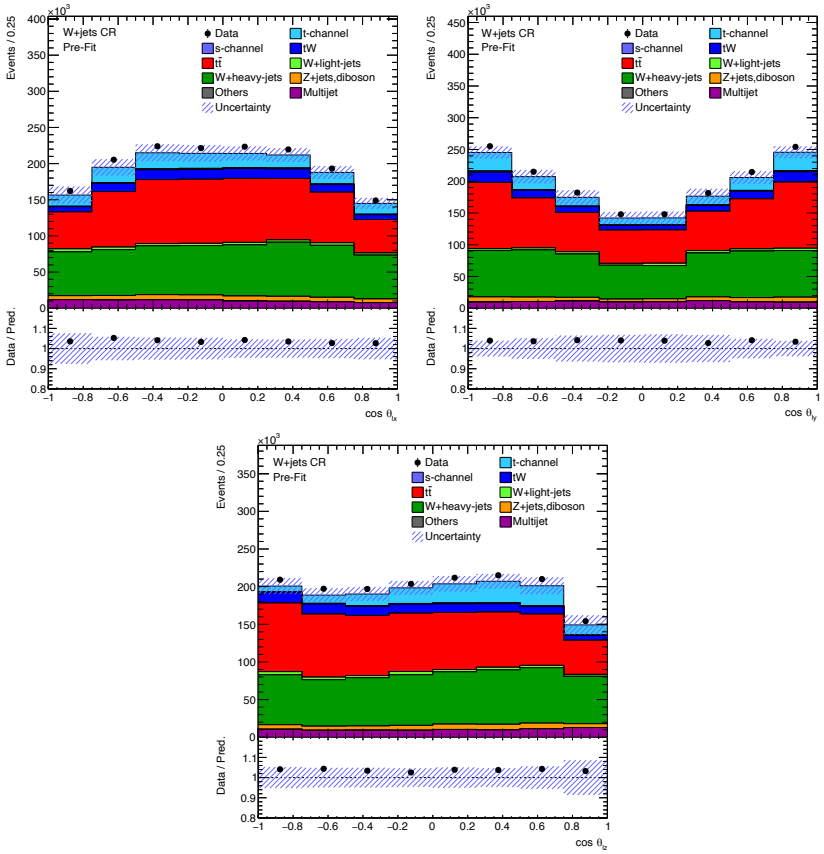

Figure 44: Distributions of $\cos\theta_{\ell x}$, $\cos\theta_{\ell y}$ and $\cos\theta_{\ell z}$ in the W+jets control region. The prediction is compared to data, shown as the black points with statistical uncertainties. No overall normalisation scale factors are considered. The uncertainty bands correspond to the uncertainties due to the size of the simulated event samples added in quadrature with the data-driven normalisation uncertainty of 100% estimated for the multijet contribution. The lower plots show the ratio of data to prediction in each bin.

3.5 Analysis Method

The method used to measure the polarisation vector of an ensemble of top quarks or antiquarks passing the event selection, defined in Section 3.2, is discussed in this section. The unit vector in the direction of the reconstructed lepton momentum in the top-(anti)quark reference frame is first determined, in the coordinate system described in Section 1.2.2. From this, the octant in which the unit vector falls is determined. The variable Q (also called the 'octant variable') is constructed by slicing the tri-dimensional phase space in eight parts, according to the signs of three angular variables $\cos\theta_{\ell x}$, $\cos\theta_{\ell y}$, $\cos\theta_{\ell z}$ as illustrated in Figure 45. This is done separately for both the top quarks and the top anti-quarks, so that sixteen bins are fitted simultaneously to a linear combination of templates for signal and background. A two-bin averaging procedure is used in order to reduce the statistical fluctuation of the W+jets and multijet samples — the content of the $2 \cdot i$-th and the $2 \cdot i + 1$-th bins, which differ in the sign of $\cos\theta_{\ell y}$, are averaged, under the SM assumption that the background processes do not depend on the sign of θ_y. Parameters of the fit are $\vec{P} = (P_x, P_y, P_z)$, both for top quarks and for top anti-quarks (i.e. six parameters in total), the overall scale factors for t-channel, $t\bar{t}$, and W+jet production rates, in addition to numerous nuisance parameters. The two control regions, namely $t\bar{t}$ control region and W+jets control region, are included in the fit and the normalizations of the t-channel, $t\bar{t}$ and W+jets are determined as well. The two control regions are two two-bin histograms containing the event yield split by the lepton charge. This allows to better control the most important backgrounds in the t-channel signal region (SR), namely the $t\bar{t}$ and W+jets processes, and more clearly distinguish the multijet contamination by exploiting the charge asymmetry which is a feature of the W+jets process, but not the multijet background.

The fitting function is a projection of the joint probability density of Eq. (51), sculpted by detector efficiency and event selection criteria and smeared by the simulation and reconstruction procedures, onto the octant variable Q. The joint probability enters at the generator level as described in Section 3.5.1, while the smearing and sculpting is the result of downstream simulation and reconstruction procedures. The fitting functions are constructed, in the usual way, by filling histograms to construct four templates:

- The template $\mathcal{T}_{z+}(Q)$, derived from the generator-level function $\mathcal{F}_{z+}(\theta, \phi, \theta^*, \phi^*)$, is estimated from MC simulation samples of top-(anti)quark events fully polarized along the $+z$ direction.

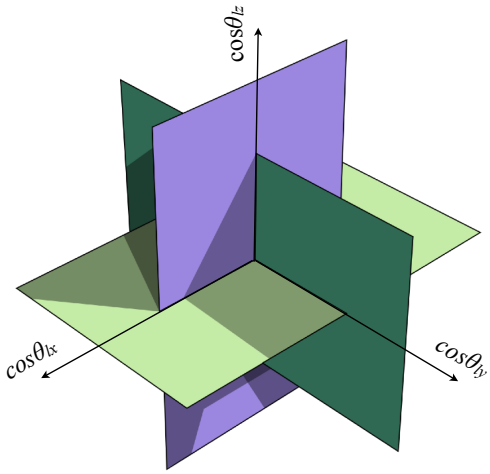

Figure 45: Representation of the octant variable Q, constructed by slicing the tri-dimensional phase space in eight parts, in terms of the signs of three angular variables $\cos\theta_{\ell x}$, $\cos\theta_{\ell y}$, $\cos\theta_{\ell z}$.

- The template $\mathcal{T}_{z-}(Q)$, derived from the generator-level function $\mathcal{F}_{z-}(\theta, \phi, \theta^*, \phi^*)$, is estimated from MC simulation samples of top-(anti)quark events fully polarized along the $-z$ direction.
- The template $\mathcal{T}_x(Q)$, derived from the generator-level function $\mathcal{F}_x(\theta, \phi, \theta^*, \phi^*)$, is estimated from MC simulation samples of top-(anti)quark events fully polarized along the $+x$ direction, as well as the $-x$ direction. Histograms of the octant variable Q for each of the polarization states are taken, and the **difference** is taken to form $\mathcal{T}_x(Q)$.
- The template $\mathcal{T}_y(Q)$, derived from the generator-level function $\mathcal{F}_y(\theta, \phi, \theta^*, \phi^*)$, is estimated from MC simulation samples of top-(anti-)quark events fully polarized along the $+y$ direction, as well as the $-y$ direction. Histograms of the octant variable Q for each of the polarization states are taken, and the **difference** is taken to form $\mathcal{T}_y(Q)$.

The fitting function for the signal is combined with the fitting function for the background (also estimated from histograms of reconstructed quantities) to form the fitting function for the data, consisting of a superposition of templates:

$$\frac{1}{\Gamma}\frac{d\Gamma}{d\Omega d\Omega^*} = \frac{1}{N(\vec{P})}\left\{\frac{1+P_z}{2}\mathcal{T}_{z+}(Q) + \frac{1-P_z}{2}\mathcal{T}_{z-}(Q) + \frac{P_x}{2}\mathcal{T}_x(Q) + \frac{P_y}{2}\mathcal{T}_y(Q)\right\} + \mathcal{T}_{\text{bkg}}(Q)\ , \quad (68)$$

where the normalization factor $N(\vec{P})$ takes into account the different acceptance effects of the four templates and normalizes the integrated cross-section to the SM expected value, predicted by the nominal POWHEG-BOX+PYTHIA8 t-channel simulation sample. Here, $\mathcal{T}_{\text{bkg}}(Q)$ is the template for the background, consisting of a sum over all of the backgrounds. The shape of all templates (i.e. $P_z = \pm 1$, $P_y = \pm 1$ and $P_x = \pm 1$) in the signal region for top quarks and top anti-quarks are found in Figure 46 while the different templates for the background processes in the W+jets and $t\bar{t}$ control regions as well as in the signal region for top quarks and top anti-quarks are shown in Figures 47-50.

The fit strategy allows to simultaneously determine the polarizations of both the top quarks and antiquarks. The signal region is split by lepton charge in two subregions: the top-quark region with a positively charged lepton and the top-antiquark region with a negatively charged one. The events in control regions are correspondingly divided into two bins each region based on the lepton charge.

The statistical analysis of the data uses a binned likelihood function $\mathcal{L}(\vec{P}^t, \vec{P}^{\bar{t}}, \vec{\theta})$, which is constructed from a product of Poisson probability terms, to estimate the polarizations. A maximum-likelihood fit is performed on the two regions simultaneously to extract six components of $\vec{P}^t = \{P_x^t, P_y^t, P_z^t\}$ and $\vec{P}^{\bar{t}} = \{P_x^{\bar{t}}, P_y^{\bar{t}}, P_z^{\bar{t}}\}$ for top quarks and anti-quarks, respectively.

$$L(\mathbf{n}, \theta^{\mathbf{0}}|\mu, \theta) = \Pi_{i \in bins} P(n_i|\mu S(\theta) + B(\theta)) \tag{69}$$

The significance/uncertainty of parameters of interest is given by the profile likelihood ratio. The expected polarisation vector of top quarks and antiquarks in t-channel events at leading order and at next-to-leading order can be extracted from fully simulated PROTOS+PYTHIA8 and POWHEG-BOX+PYTHIA8, respectively, and are shown in Table 14. More details about the extraction of the theoretical predictions can be found in Appendix C. Depolarization from NLO effects are too small to be seen within the statistical uncertainties of these samples.The polarization estimated using POWHEG-BOX+PYTHIA8 furnishes an expectation of the polarization of top quarks and anti-quarks for the ensemble of signal events passing selection criteria: the P_y components are consistent with 0 within the statistical uncertainty and the top anti-quark shows a non-zero polarisation along the x direction, as predicted by Refs. [14, 19].

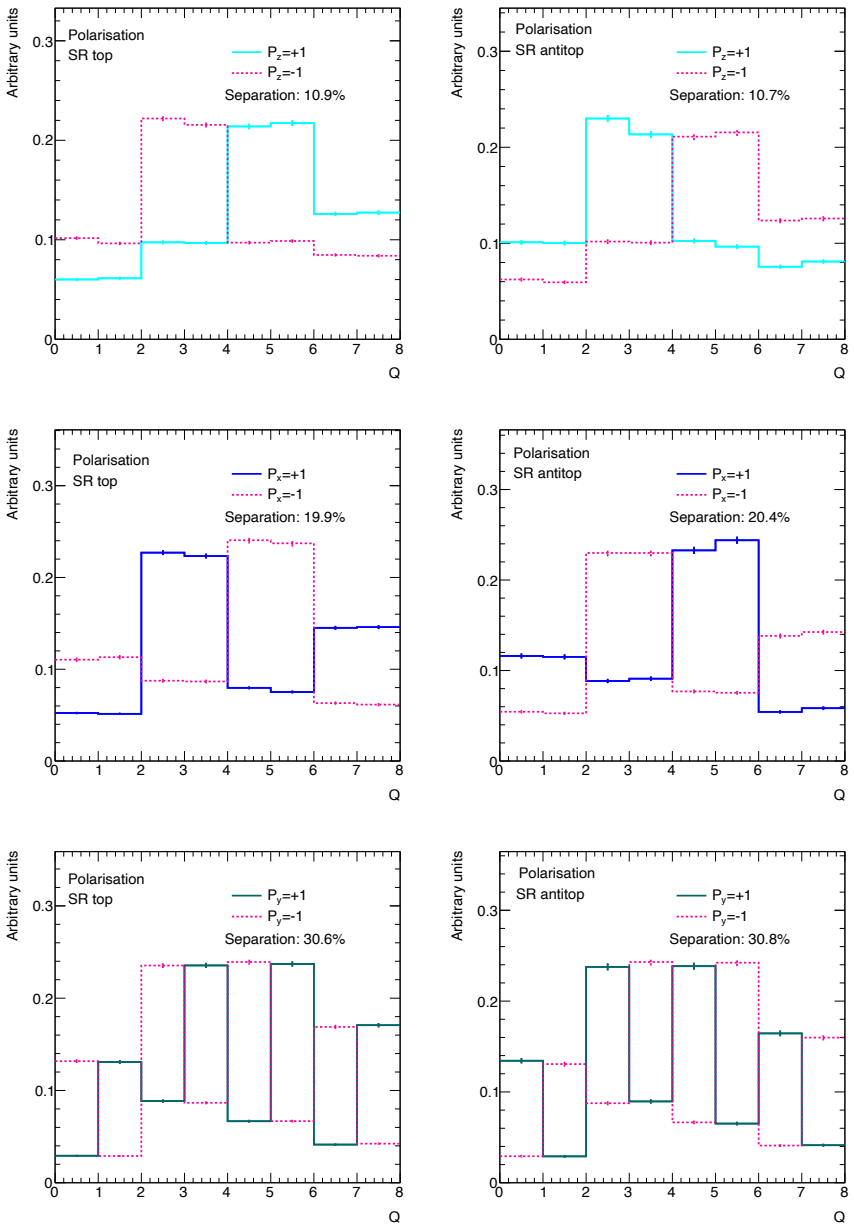

Figure 46: Separated t-channel process for $P_z = +1$ and $P_z = -1$ is shown in the signal region for top quarks and top anti-quarks while for $P_x = \pm 1 (P_y = \pm 1)$ this is also shown in the signal region for top quarks and top anti-quarks.

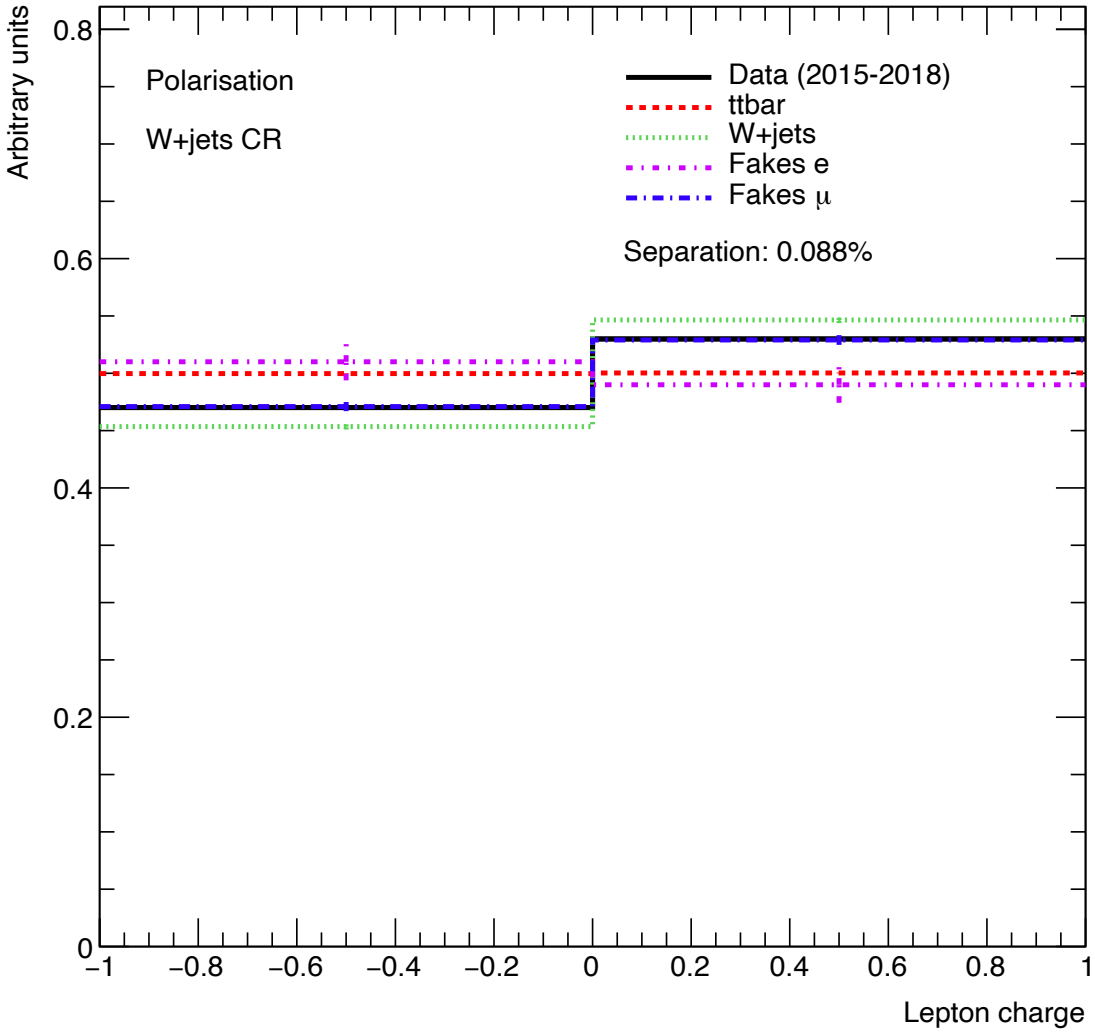

Figure 47: Separated $t\bar{t}$, W+jets, Multijet processes are shown in the W+jets control region, in which the W+jets accounts for 37% of the event yield, and $t\bar{t}$ and t-channel make up for 39% and 10%, respectively. A clear charge asymmetry can be observed here for W+jets process.

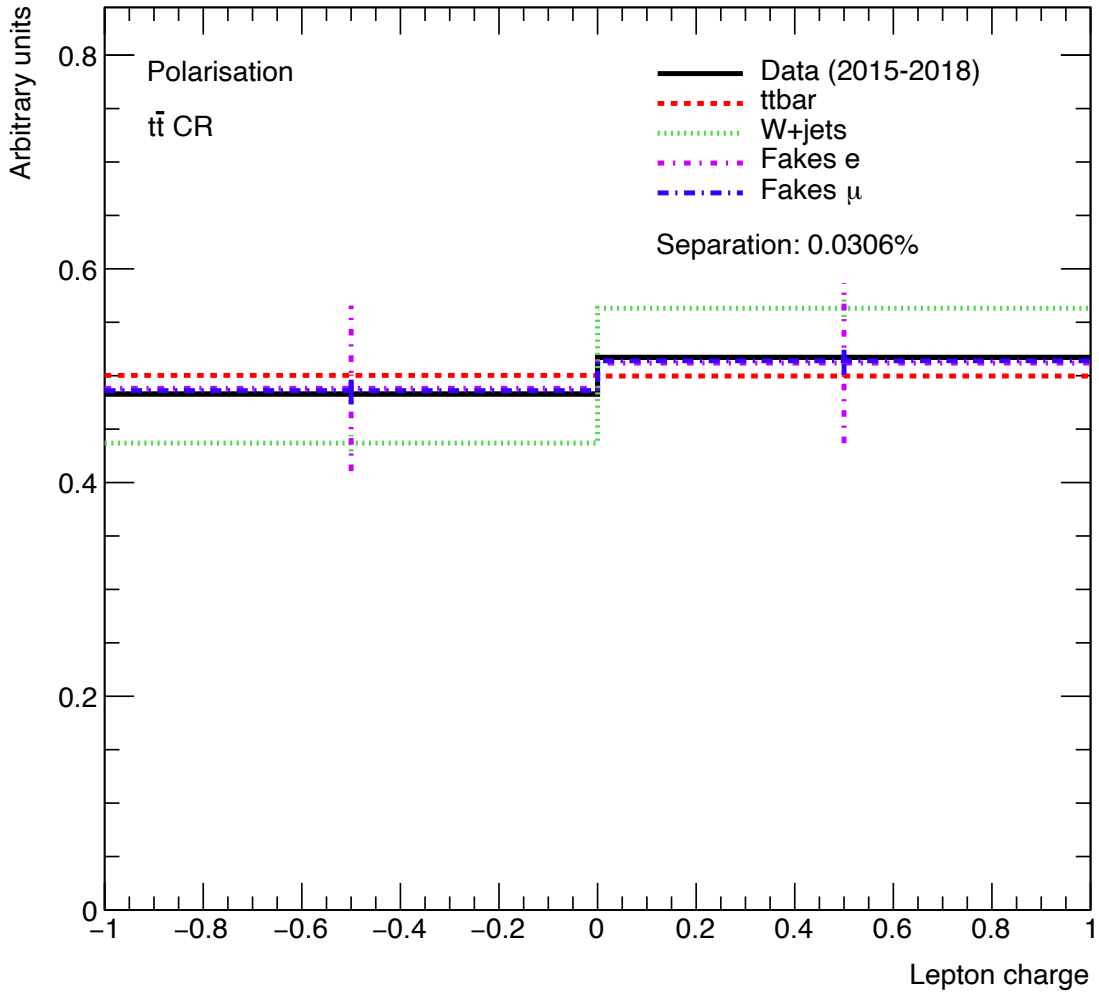

Figure 48: Separated $t\bar{t}$, W+jets, Multijet processes are shown in the $t\bar{t}$ control region, in which the $t\bar{t}$ accounts for 74% of the events, and W+jets and t-channel make up for 9% and 7%, respectively. A clear charge asymmetry can be observed in both CRs for only W+jets process.

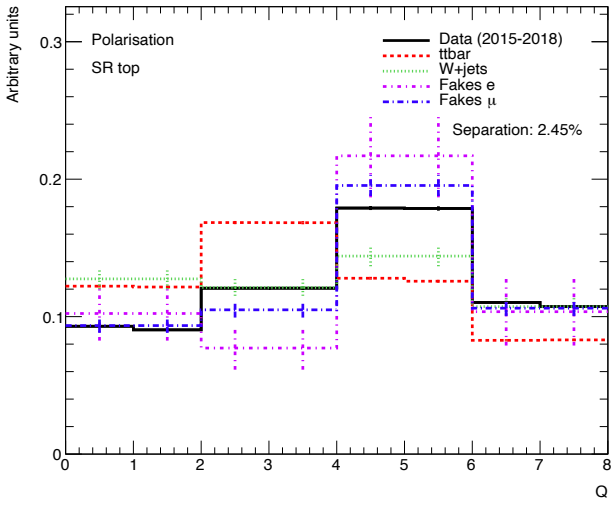

Figure 49: Separated $t\bar{t}$, W+jets, Multijet processes are shown in the SR with the postive lepton charge (top quark).

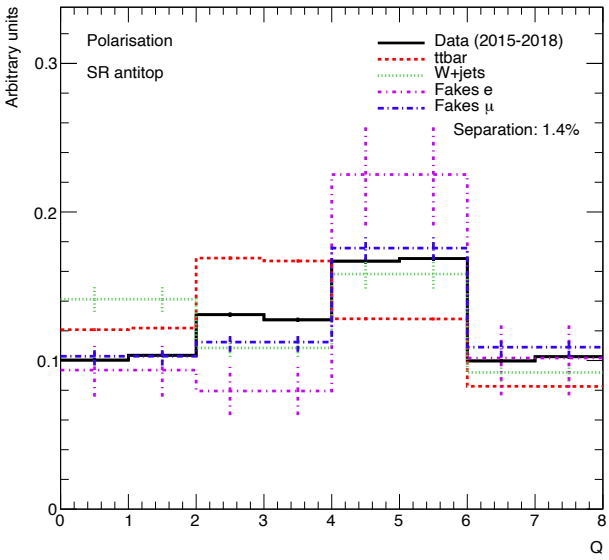

Figure 50: Separated $t\bar{t}$, W+jets, Multijet processes are shown in the SR with the negative lepton charge (top anti-quark).

SM sample	P Component	Extracted value + stat. (t)	Extracted value + stat. ($\bar{t}$)
POWHEG-BOX+PYTHIA8	P_x	0.040 ± 0.0120	-0.070 ± 0.0157
	P_y	-0.008 ± 0.0076	0.000 ± 0.0080
	P_z	1.024 ± 0.0150	-0.967 ± 0.0200
PROTOS+PYTHIA8	P_x	0.038 ± 0.0135	-0.068 ± 0.0018
	P_y	0.004 ± 0.0087	-0.015 ± 0.0112
	P_z	0.983 ± 0.0170	-0.944 ± 0.0230

Table 14: Polarisation of the top quark and antiquark samples estimated using POWHEG-BOX (NLO) and PROTOS (LO) generators. The statistical error only is quoted. The measurements are performed on the signal solely.

3.5.1 The PolManip Package

The template fit method described above requires samples of simulated data in which the polarization is varied. In MC computations of top-quark production and decay, the polarization cannot be varied directly; instead, typical event generators only allow users to vary fundamental parameters such as coupling constants, which modify not only the polarization, but also the differential production cross-section, and differential decay rates. A C++ program called POLMANIP was developed in order to modify the polarization of top quarks produced by the PROTOS generator. It works by removing all of the decay products of the top quark, and re-decaying the top quark according to a user-specified polarization state. The differential rates used in the decay model are the LO expressions of Eq. (49) from Ref. [24]. The procedure is used in conjunction with the PROTOS generator to produce templates used in a fit to polarization, as shown in Figure 51. The coordinate system is the same as described in Section 1.2.2.

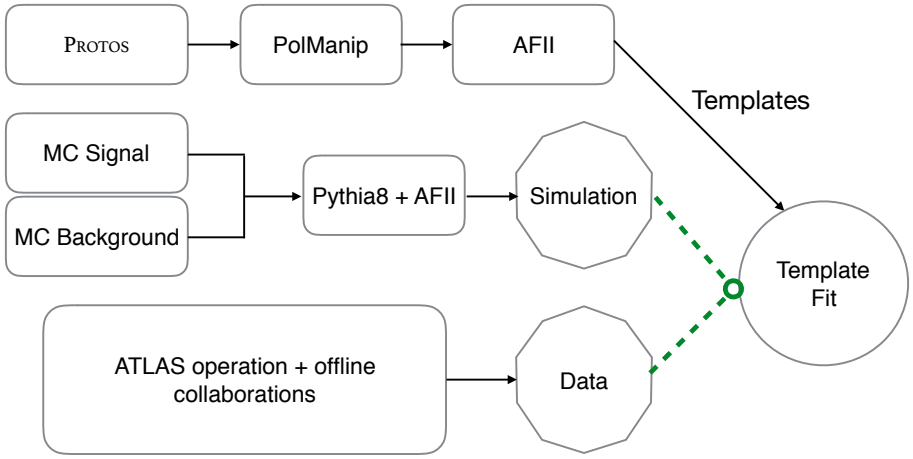

Figure 51: A simple flow chart overviewing the template fit method. The switch on the block "template fit" is either pointed at simulation or data.

The PROTOS generator produces a file of events in ASCII format, in which the four-momentum of the beam particles and all of the final-state particles are recorded. POLMANIP accepts the x, y, and z components of polarization as configuration options, reads in PROTOS output, and writes an output file in the same format as PROTOS. Histograms of kinematic quantities are also produced and recorded in a ROOT file, for parton-level studies. POLMANIP was employed to generate four

templates containing six pure ensembles of top quarks with P_x, P_y, or P_z equal to ± 1, in addition to reference samples with its polarization fixed to the $\vec{P} = (0.0, 0.0, +0.9)$ for top quarks, and $\vec{P} = (-0.14, 0.0, -0.86)$ for top anti-quarks as calculated in Ref. [14]. The POLMANIP procedure is extensively validated. Prior to the official ATLAS production of the template simulation samples, a total of 36 million events, 5 million for each polarisation configuration and 6 million as reference, were generated for validation studies. Figure 52 shows the effect on the observable $\cos\theta_{\ell z}$, the observable most strongly correlated to the polarisation of the top quark.

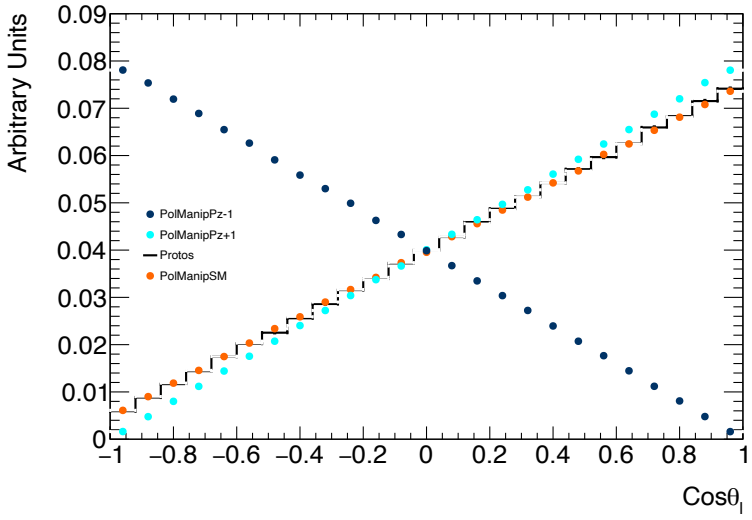

Figure 52: A comparison of the templates generated by POLMANIP. The cyan and indigo dots represent the $P_z = +1$, $P_z = -1$ respectively. The black histogram refers to the original SM sample without modification, and the orange dots represent the POLMANIP generated sample with an imposed polarisation that resembles the SM expectation at $\sqrt{s} = 13$ TeV. The orange sample agrees well with the original SM sample, where the purely polarized samples behave just as expected.

3.6 Sources of Systematic Uncertainty

Various sources of systematic uncertainty are considered in this analysis following the top-quark working group standard prescriptions. All signal and background processes have systematic uncertainties, some of which are process-dependent (e.g. generator specific) and others generic (e.g. Jet Energy Scale (JES)). These systematic uncertainties, have either an impact on the rate of the individual contributions or on the shape of their associated kinematic and angular distributions. The systematic uncertainties are included as nuisance parameters (NPs) in the fit, considering simultaneously the signal and the two control regions, as discussed in Section 3.5.

A list of systematic uncertainties and the procedure to evaluate each of them is discussed in this section. They are grouped into two main categories: experimental and theoretical modelling uncertainties. The effect due to the statistics of the simulated event samples is also taken into account when evaluating the total uncertainty.

3.6.1 Experimental Uncertainties

3.6.1.1 Luminosity The individual uncertainty in the 2015, 2016, 2017 and 2018 integrated luminosities are 2.1%, 2.2%, 2.4% and 2.0, respectively. These uncertainties are derived from the calibration of the luminosity scale using x-y beam-separation scans, following a methodology similar to that detailed in Ref. [64], and using the LUCID-2 detector for the baseline luminosity measurements [65]. The luminosity uncertainty is applied to each MC simulated process in order to scale them to match the expected number of events at the given luminosity for each year. The impact of this uncertainty is estimated by varying accordingly the overall normalizations of all simulated event samples.

3.6.1.2 Pile-up Reweighting All MC simulated event samples are re-weighted to match the observed distribution of the average number of interactions per bunch-crossing in data [66]. The re-weighting procedure is basically having the hard-scattering events overlaid by the MC simulated events, then trying to re-weight the MC events to reproduce the distribution of the average number of interactions per bunch crossing ($\langle\mu\rangle$). To account for the difference in pile-up distributions

between data and MC simulations, an uncertainty related to the data scale factors is applied. Up and down variations of these uncertainties related to the pile-up scale factors are propagated.

3.6.1.3 Charged Lepton Reconstruction, Identification, Isolation and Trigger For charged leptons (i.e. electrons and muons), the reconstruction, identification, isolation and trigger performances can all lead to differences between data and MC. To correct for these differences, scale factors are applied. They are estimated with the "tag-and-probe" method with electrons and muons from Z boson, W boson and J/ψ decays using methods similar to those from Refs. [67]. The method basically relies on experimental information from well-known resonance decays to electrons (or other leptons) such as $Z \to ee$, and then apply the information later for electron pre-identification. The uncertainties are evaluated by varying up and down by 1σ the predicted event yields and re-applying the event selection to the signal and backgrounds.

3.6.1.4 Charged Lepton Momentum Scale and Resolution The precision of the charged lepton momentum scale and resolution may be different between the simulated events and the observed data. The simulation is inspected with reconstructed distributions of $Z \to \ell^+\ell^-$ and $J/\psi \to \ell^+\ell^-$ masses using methods similar to the ones used in Ref. [68]. In the case of electrons, also events with $W \to e\nu$ are used. Observed discrepancies between data and simulation are corrected by applying recommended corrections from the combined performance groups. For muons, corrections to momentum scale and resolution are applied only to the simulation. Uncertainties on momentum scale and resolution of muons originating from the ID and the muon spectrometer are considered and varied separately. The impact on the measurement of the electron (muon) energy (momentum) and resolution uncertainties are evaluated by scaling or smearing up and down the charged lepton transverse energy/momentum by 1σ and re-applying the object and event selections to the simulated event samples.

3.6.1.5 Jet Vertex Tagger (JVT) Efficiency The JVF variable is defined as the scalar transverse momentum (p_T) sum of the tracks that are associated with the jet and originate from the hard-scatter vertex divided by the scalar p_T sum of all associated tracks. JVF is bound between 0 and 1, but a value of 1 is assigned to jets with no associated tracks[69]. Scale factors, used

to account for differences between the JVT efficiency in simulation and data, are derived using $Z(\rightarrow \mu\mu)$+jets events. A control region is used to estimate the pile-up contamination in the signal region. The contribution from hard-scatter jets in the control region is subtracted and a conservative uncertainty of 30% is used to cover a potential mis-modelling.

3.6.1.6 Jet Energy Scale To determine the jet energy scale (JES) and its associated uncertainty, information from test-beam data, LHC collision data and simulation are used. Data taken at $\sqrt{s} = 13$ TeV is used to calibrate the residual uncertainty on the JES [70]. Events with a vector boson and additional jets are used to calibrate jets in the central region. Di-jet events are exploited to calibrate forward jets against the jets in the central region of the detector. Multijet events are used to calibrate high p_{T} jets. In this analysis, the "CategoryReduction" uncertainty set [71] is used. This results in a set of 29 NPs (from nearly 100 NPs), each with an up/down variation, which can have different jet p_{T} and η dependencies.

3.6.1.7 Jet Energy Resolution In our analysis, this systematic is projected to have the most impact. The jet energy resolution (JER) can be parametrized with a stochastic term, a noise term and a constant term. It is extracted from di-jet events by measuring the width of the di-jet asymmetry distribution across p_{T} and η [71]. Measurements using zero-bias data with random cones are used to constrain the noise term. The performed fit gives about 117 NPs. An eigenvector decomposition is used which gives a smaller set with 7 NPs. First, nominal smearing is applied on jets. If the JER in MC is found to be smaller than in data, the MC is smeared to match the average resolution in data. If the JER is lower in data, nothing is done because one would not want to degrade the data to match a given MC. The uncertainties of the JER are then propagated by smearing the jets in the MC with a Gaussian with $\sigma^2_{\text{smear}} = (\sigma_{\text{nominal}} - \sigma_{\text{NP}})^2 - \sigma^2_{\text{nominal}}$ where σ_{nominal} is the nominal JER after the previous smearing and σ_{NP} is the 1σ variation of the JER uncertainty component. Finally, if the JER in data is lower than in the MC, the difference is taken as an additional uncertainty. Therefore, in total 8 NPs are used for the JER uncertainty, in this analysis ("SimpleJER" uncertainty set):

- A data/MC comparison term (`DataVsMC`).
- Seven modelling/theory component (`EffectiveNP`).

3.6.1.8 Heavy- and Light-flavour Tagging The b-tagging algorithm needs to be calibrated in order to have a match between the performance in simulation and in data. Therefore, corrective scale factors are derived from data [72]. The b-tag and c-tag efficiencies and the mis-tag rate for light-flavour jets are measured and scale factors are calculated as the ratio of the efficiencies (or mis-tag rates) in data and simulation. In general, the scale factors depend on jet p_{T} and η. Uncertainties are propagated into the analysis via 9 NPs for b-jets (`bTagSF_B`, `bTagSF_extrapolation` and `bTagSF_extrapolation_from_charm`), 4 NPs for c-jets (`bTagSF_C`) and 17 NPs for light-flavour jets (`bTagSF_Light`), respectively. Extrapolation uncertainties are not provided when using pseudo-continuous b-tagging.

3.6.1.9 Missing Transverse Momentum Uncertainties of the soft-track component are derived from the level of agreement between data and MC simulation of the p_{T} balance between the hard and soft $E_{\mathrm{T}}^{\mathrm{miss}}$ components. Three different uncertainties are considered: an offset along the p_{T} (hard) axis (`SoftTrk_Scale`), as well as the smearing resolution along and perpendicular to the p_{T} (hard) axis (`SoftTrk_ResoPara` and `SoftTrk_ResoPerp`, respectively). These effects are estimated by varying the scales and resolutions up and down by 1σ before re-doing the selection of the simulated event samples.

3.6.1.10 MC Generator and PS Modelling The uncertainties due to the choice of the MC event generator, PS and hadronisation models, scales, etc is evaluated for the t-channel signal and for the top-quark backgrounds by considering alternative generators or varied parameters of the baseline event generators. These uncertainties are estimated by varying one by one the different processes (i.e. uncorrelated).

- **Matrix Element (ME) Modelling (t-channel and top-quark backgrounds):** To assess the uncertainty due to the choice of the matching scheme in the t-channel ME generation, the nominal MC generator POWHEG-BOX is compared to AMC@NLO. The parton showering and hadronization are simulated with PYTHIA8 in both cases.
- **PS and Hadronization Model (t-channel and top-quark backgrounds):** To describe the impact of the uncertainty coming from the chosen PS and hadronization model, the nominal

sample which uses PYTHIA8 is compared to another sample using HERWIG7. The ME generator for both samples is POWHEG-BOX.

- **ISR/FSR (t-channel and Top-quark Backgrounds):** To estimate the uncertainty originating from ISR modelling, weights are used in the ME and in the PS within the baseline POWHEG-BOX+PYTHIA8 sample. To simulate higher parton radiation, the factorization and renormalization scales are varied by a factor of 0.5 in the ME while using the Var3c up variation from the A14 tune. For lower parton radiation, μ_R and μ_F are varied by a factor of 2.0 while using the Var3c down variation in the PS. The impact of FSR is evaluated using PS weights which vary the renormalisation scale for QCD emission in the FSR by a factor of 0.5 and 2.0, respectively.

3.6.1.11 PDF PDF uncertainties are evaluated using the PDF4LHC15 uncertainty set which consists of 30 NPs. Internal re-weighting in the nominal POWHEG-BOX+PYTHIA8 sample is used. It is re-weighted to the PDF4LHC15 PDF and its uncertainty set, and the symmetrized uncertainties are propagated to various distributions used in the template fit.

3.6.1.12 Multijet Normalization The multijet background is normalized through a data-driven analysis based on the techniques described in Section 3.3. A relative systematic uncertainty of $\pm 40\%$ is assigned to this data-driven overall normalization through a separate template fit in the QCD-enriched preselection region and ttbar control region.

3.6.1.13 Multijet Shape To evaluate the systematic uncertainty on the shape of the multijet templates, as mentioned in Section 3.3, additional MC simulation samples were produced varying some parameters and therefore modifying the templates of the multijet background. These alternative multijet templates are normalized to the nominal yields and compare to the nominal multijet templates.

3.6.2 Statistical Uncertainty

Statistical fluctuations in the MC simulated event samples contribute to the overall systematic uncertainty. These uncertainties arise from the statistics of background MC on one hand, and from the statistics of signal MC on the other.

3.7 Treatment of the Systematic Uncertainty

In this section we describe the procedure in which systematic uncertainties described in Section 3.6.1 are incorporated into the analysis and propagated into uncertainties on the measured parameters P_x,P_y, P_z for both the top quarks and anti-quarks.

A systematic uncertainty is estimated through varying a certain nuisance parameter (i.e. the energy scale of measured jets) up and down by one standard deviation of its nominal value, assuming a Gaussian behavior. The uncertainty of the parameter is provided by other analyses or a dedicated performance measurement. This results in the templates to differ in both their shape and normalization. These nuisance parameters then enter the fit by multiplying the corresponding Gaussian terms into the likelihood function.

$$L(\mathbf{n}, \theta^{\mathbf{0}}|\mu, \theta) = \Pi_{i\in bins} P(n_i|\mu S(\theta) + B(\theta)) \times \Pi_{j\in n.p.} G(\theta_j^0|\theta_j) \tag{70}$$

Afterwards the likelihood function will be minimized numerically. For a better computational performance, the shape and normalization of certain variations that are below 5 per mille in every bin are dropped (or so-called "pruned"). The extracted polarizations are shown in Table 16. The total uncertainty is completely dominated by the systematic uncertainty.

Figures 57-58 show the ranking of the NPs in terms of their impact on the fitted P_x^t, P_y^t, P_z^t, $P_x^{\bar{t}}$, $P_y^{\bar{t}}$ and $P_z^{\bar{t}}$. Several features can be seen from these plots. First, none of the systematic variations considered in this analysis can induce a shift in the value of P_y, which can only arise from CP violating effects. Therefore the apparent uncertainties in P_y come from two sources; first, the limited statistics of the samples used to predict the data ("the γ's"), and second, the limited statistics of the samples used to evaluate the uncertainty. The γ's are assumed Poisson priors, and a single γ is assigned to the total prediction (signal and background) in each bin. It is gratifying to see that these effects are an order of magnitude or so smaller than the very real effects of the variations upon P_x and P_z. Also, in this regard, it is natural to see the γ's rank high for P_y and generally low for the P_x and P_z.

The extraction of polarization depends upon the measured angle of the electron or the muon *in the rest frame of the top quark*. Both the energy of the lepton and its direction are extremely well measured; however the reconstructed angles depend critically on the reconstruction of the

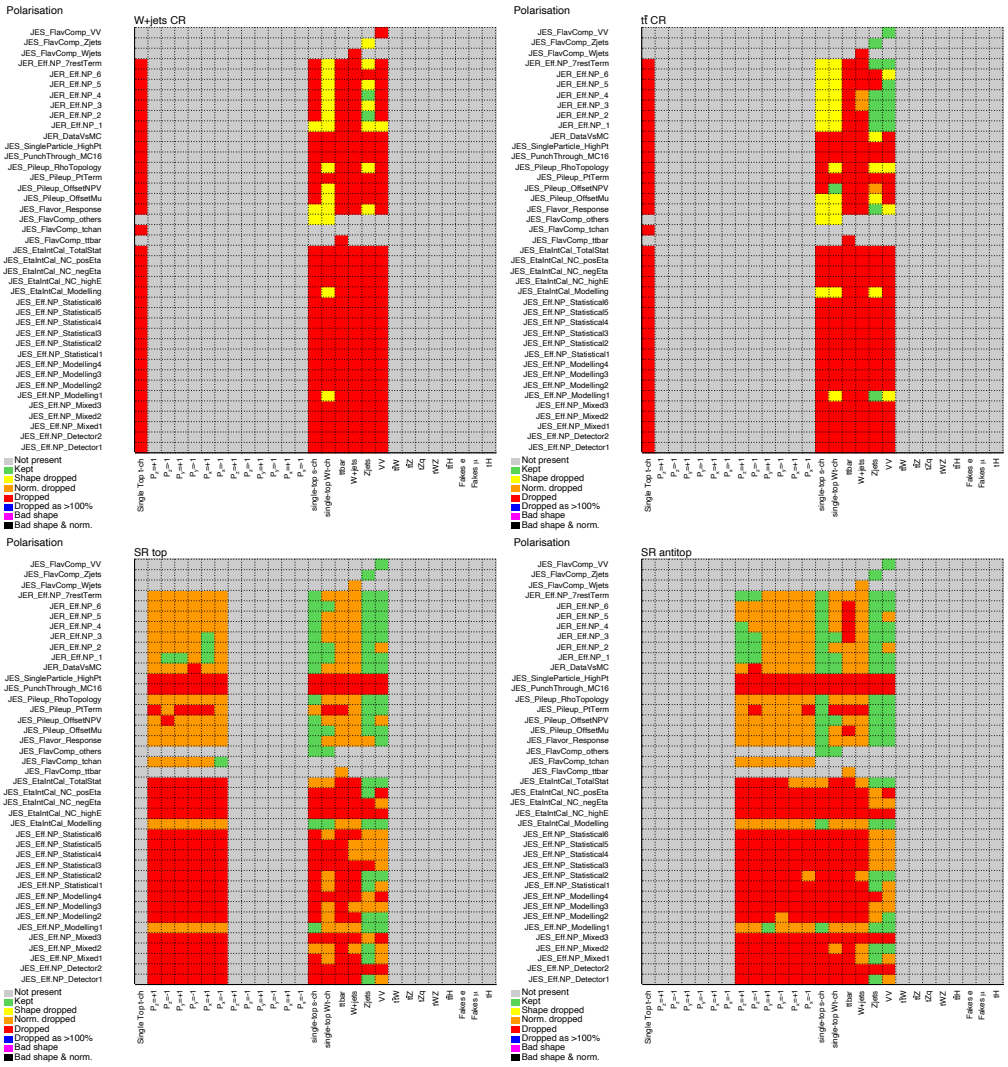

Figure 53: An overview of the JES and JER systematic uncertainties included in the fit before and after the pruning stage in the W+jets control region, the $t\bar{t}$ control region and the signal region for top quarks and top anti-quarks. The pruning threshold used is 5 per mille, i.e. the shape and normalisation variations (per sample, per region) which are below 5 per mille in each bin are dropped. The single top-quark t-channel templates (i.e $P_z = +1$) are divided into two SRs by the different lepton charge.

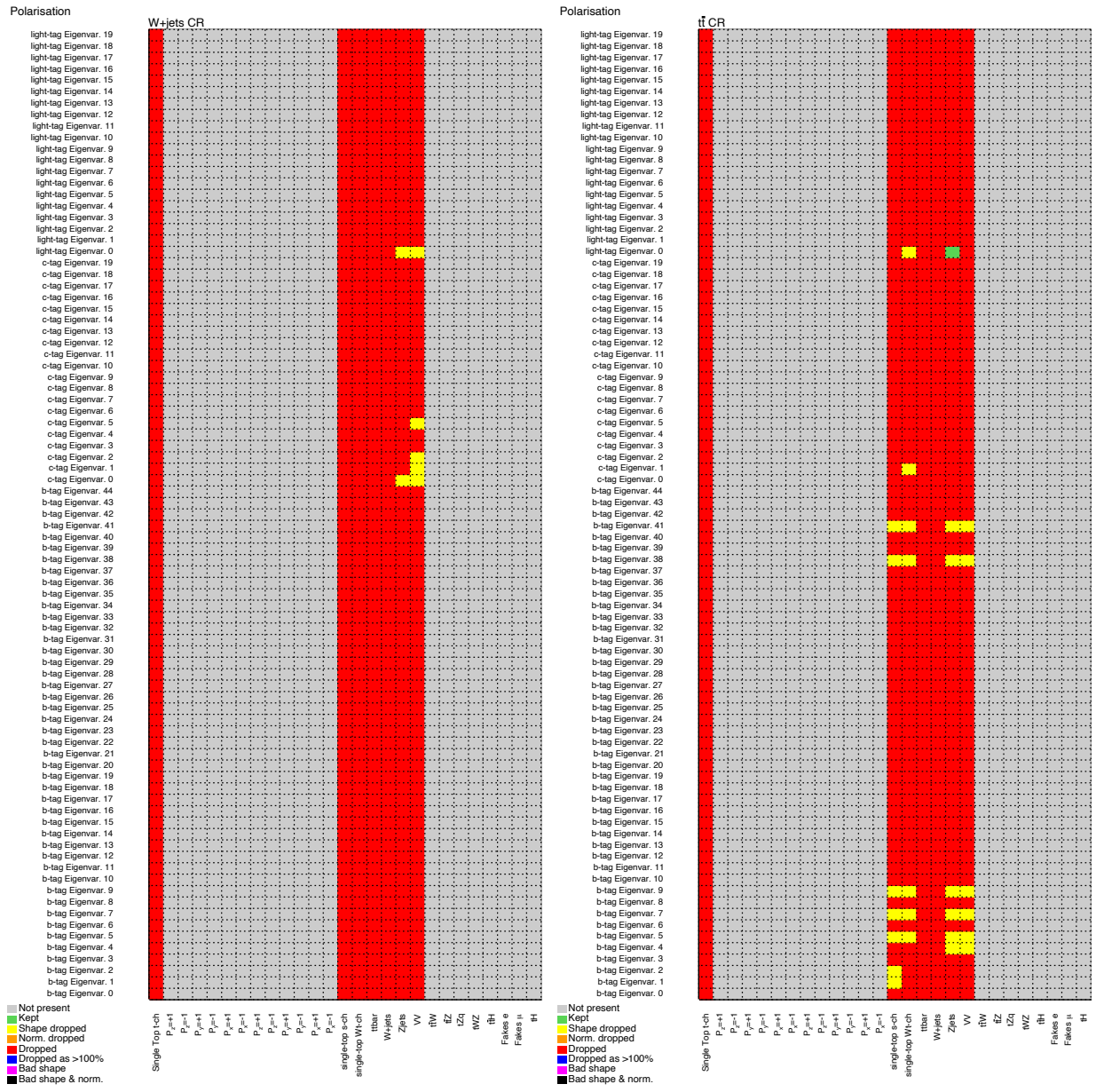

Figure 54: An overview of the Flavoring TAGging(FTAG) systematic uncertainties included in the fit before and after the pruning stage in the W+jets control region and the $t\bar{t}$ control region. The pruning threshold used is 5 per mille, i.e. the shape and normalisation variations (per sample, per region) which are below 5 per mille in each bin are dropped. Most FTAG systematics are shown to be dropped here.

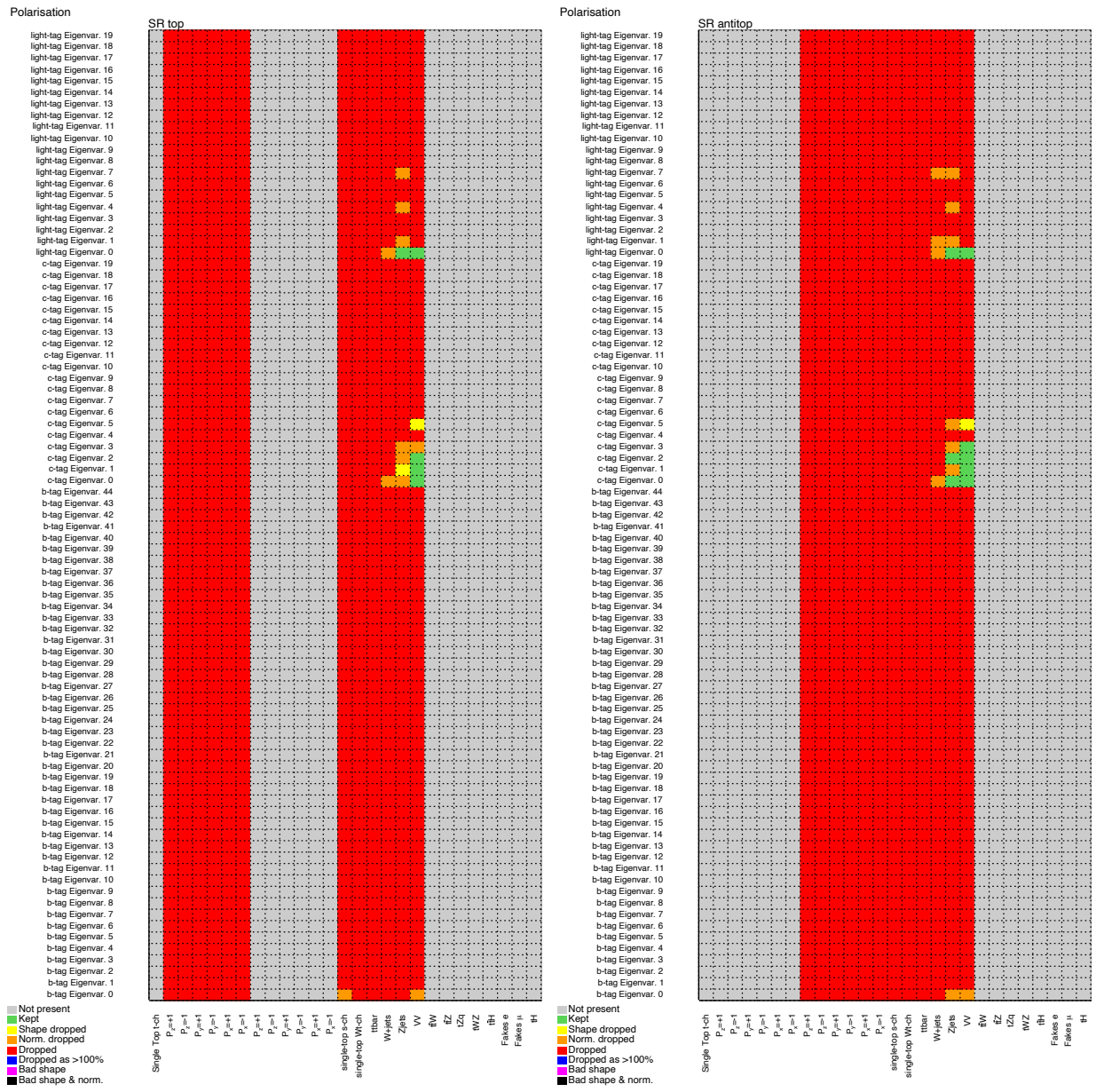

Figure 55: An overview of the FTAG systematic uncertainties included in the fit before and after the pruning stage in the signal region for top quarks and top antiquarks. The pruning threshold used is 5 per mille, i.e. the shape and normalisation variations (per sample, per region) which are below 5 per mille in each bin are dropped. Most FTAG systematics are shown to be dropped here.

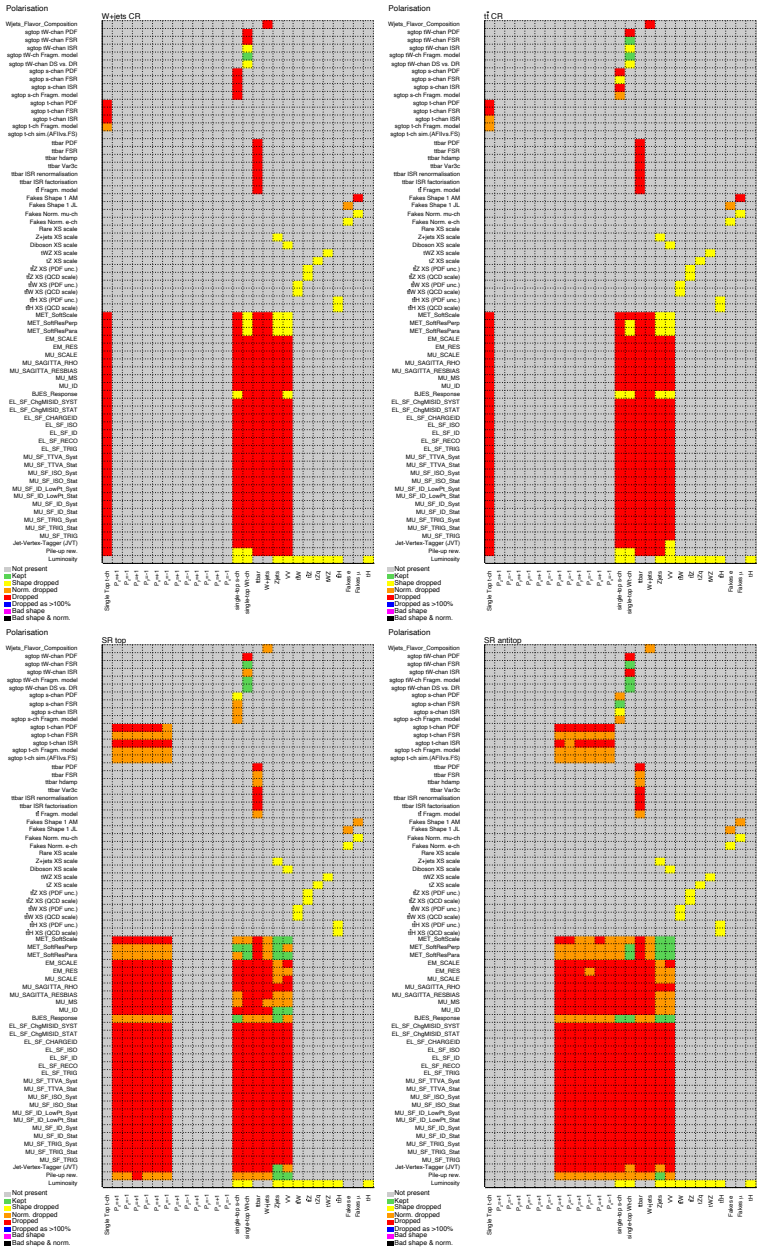

Figure 56: An overview of the other systematic uncertainties included in the fit before and after the pruning stage in the W+jets control region, the $t\bar{t}$ control region and the signal region for top quarks and top antiquarks. The pruning threshold used is 5 per mille, i.e. the shape and normalisation variations (per sample, per region) which are below 5 per mille in each bin are dropped.

top-quark reference frame, which in turn depends upon the reconstruction of jets on one hand and the neutrino on the other. Not surprisingly, the JER and JES uncertainties are the main sources of systematic uncertainty in this analysis.

The most important sources of systematic uncertainties in P_x and P_z are those related the measurement of jets (mainly JES and JER), of the effect of using either full or AFII simulated event samples, of $E_{\mathrm{T}}^{\mathrm{miss}}$ effects, and of t-channel and $t\bar{t}$ fragmentation and hadronisation models. For P_y, the most important sources of systematic uncertainties are also the ones related the measurement of jets (JES and JER), the limited statistics of background samples from MC, the $E_{\mathrm{T}}^{\mathrm{miss}}$ effects.

Figure 59 shows the full list of NPs and γ factors fitted values after the fit, grouped by categories. It can be seen from these plots that the data constraints the Multijet normalization nuisance parameters. This constraint arises from the ditribution of events in different signal and control regions, and in particular in the W+jets control region. This region, as one can see from Figure 30, has large contributions from $t\bar{t}$ and from W+jets, Multijet backgrounds and other backgrounds. The other backgrounds are constrained from simulation. The $t\bar{t}$, in our fit, is constrained from the $t\bar{t}$ control region. Since the Multijet background is charge-symmetric while the W+jets background is charge asymmetric, the absolute contribution of each background source is constrained by the event yields in the positive and negative W+jets control region.

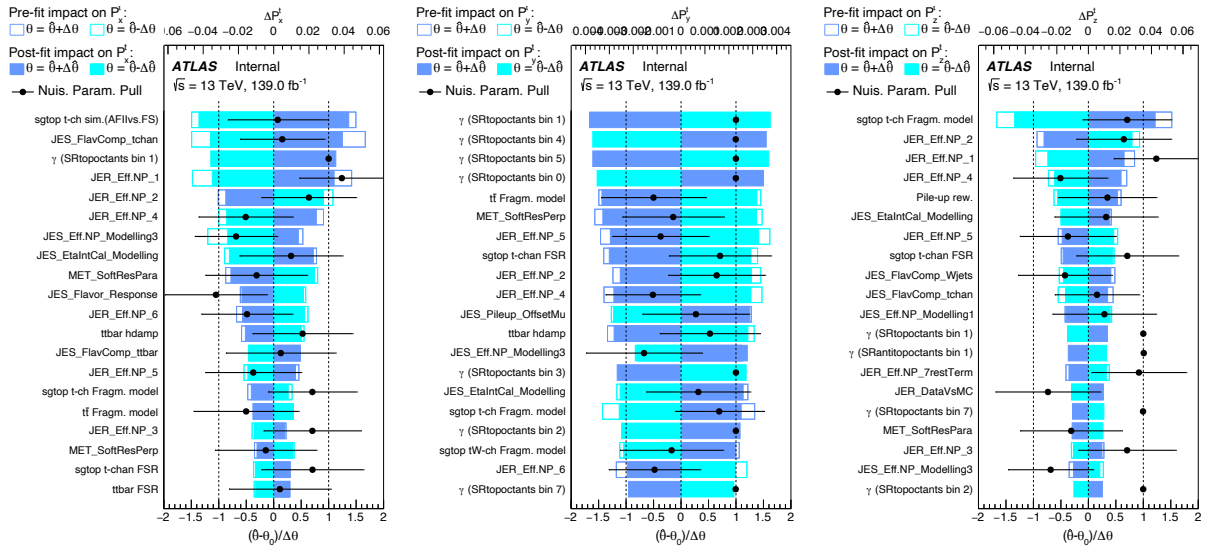

Figure 57: Impact of systematic uncertainties on the fitted parameters $\hat{P_x}^t$, $\hat{P_y}^t$ and $\hat{P_z}^t$. The systematic uncertainties are listed in decreasing order of their impact on $\hat{P}_i^t$ on the y-axis. The blue boxes show the variations of $\hat{P}_i^t$ with respect to the total uncertainty on P_i^t, $\sigma_{P_i^t}$, referring to the upper x-axis, when fixing the corresponding individual NP, θ, to its post-fit value $\hat{\theta}$ modified upwards or downwards by its post-fit uncertainty, and repeating the fit. The filled circles, which refer to the lower x-axis, show the pulls of the fitted NPs. The black lines show the post-fit uncertainties of the NPs, relative to their nominal uncertainties, which are indicated by the dotted line.

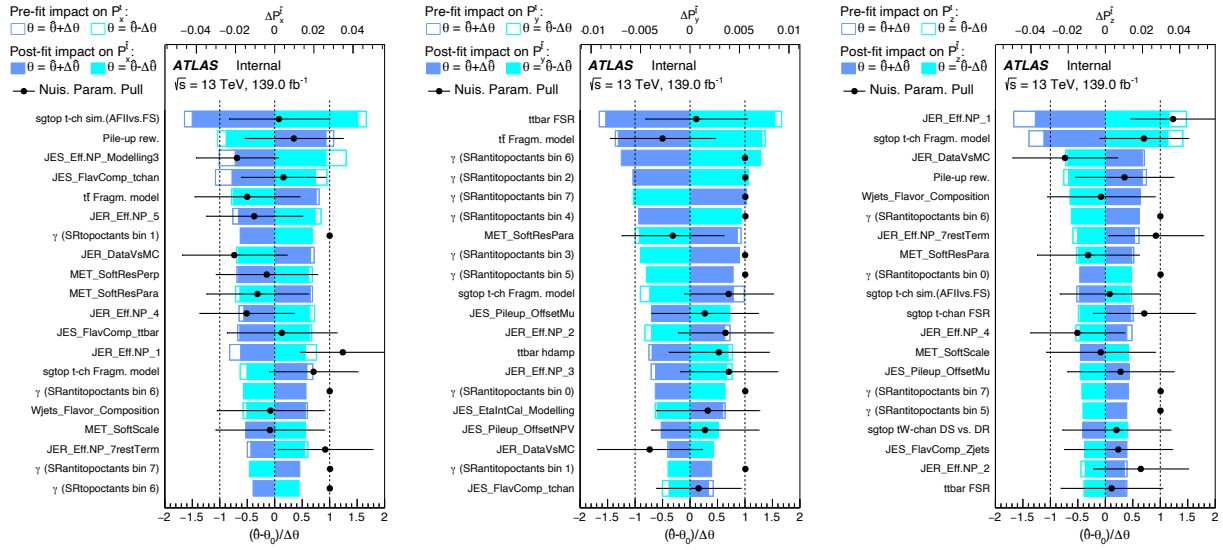

Figure 58: Impact of systematic uncertainties on the fitted parameter $\hat{P}_x^{\bar{t}}$, $\hat{P}_y^{\bar{t}}$ and $\hat{P}_z^{\bar{t}}$. The systematic uncertainties are listed in decreasing order of their impact on $\hat{P}_i^{\bar{t}}$ on the y-axis. The blue boxes show the variations of $\hat{P}_i^{\bar{t}}$ with respect to the total uncertainty on $P_i^{\bar{t}}$, $\sigma_{P_i^{\bar{t}}}$, referring to the upper x-axis, when fixing the corresponding individual NP, θ, to its post-fit value $\hat{\theta}$ modified upwards or downwards by its post-fit uncertainty, and repeating the fit. The filled circles, which refer to the lower x-axis, show the pulls of the fitted NPs. The pulls are obtained by comparing the most likely parameter value ($\hat{\theta}$) through the profile likelihood fit, and the nominal value (considered as 'true') (θ_0) provided by the dedicated experiment. The black lines show the post-fit uncertainties of the NPs, relative to their nominal uncertainties, which are indicated by the dotted line.

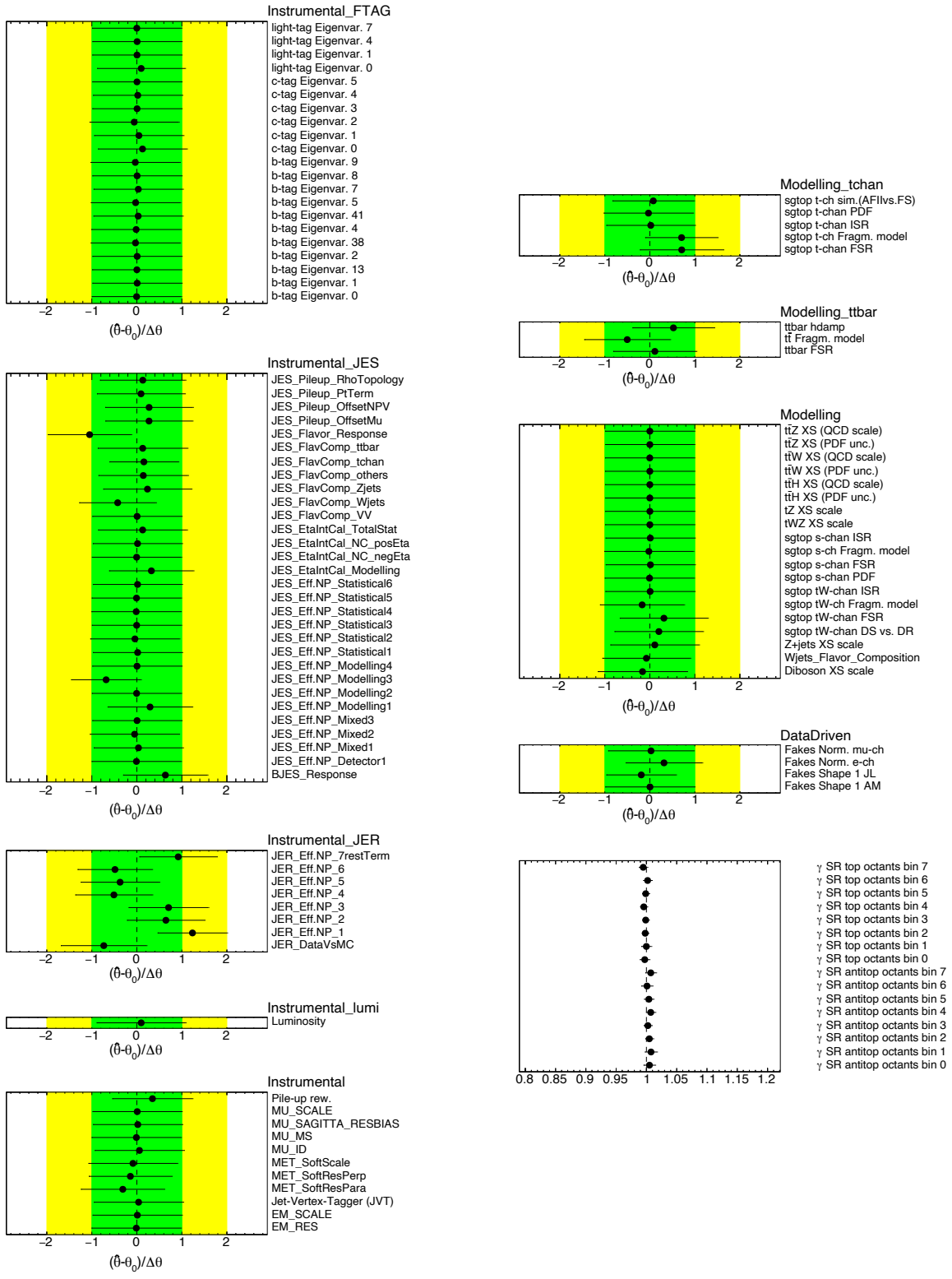

Figure 59: Nuisance parameters and γ's pulls split by categories. $\hat{\theta}$ represents the maximum likelihood estimator, and θ_0 represents the nominal value of each nuisance parameter. The pre-fit value of each NPs corresponds to $0 \pm 1\sigma$ (in green) and $\pm 2\sigma$ (in yellow) on the x-axis.

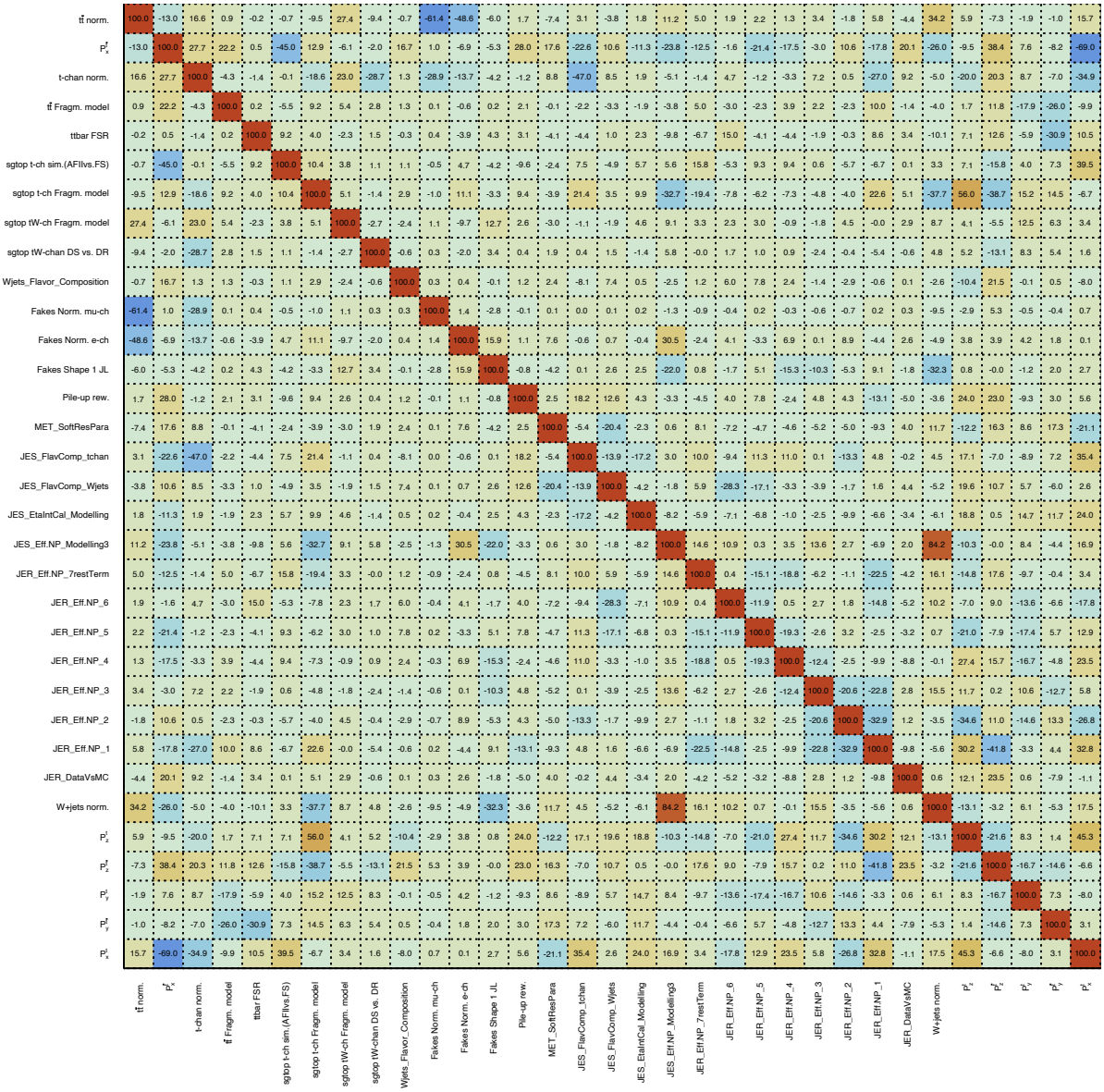

Figure 60: Matrix of correlations between fitted parameters, including both parameters of interest (P_x^t,P_y^t,P_z^t,$P_x^{\bar{t}}$,$P_y^{\bar{t}}$,$P_x^{\bar{t}}$) and nuisance parameters. Not all parameters are included in the plot, where the cutoff threshold is 25%.

3.8 Results

The observed best-fit values of the scale factors used to adjust the theoretical predictions of $t\bar{t}$, W+jets, and single top t-channel production rates using this data are shown in Table 15. Figures 61-62 show the distributions used in the fit, before and after performing the fit. In Tables 17-18 the pre- and post-fit yields are shown. Finally, Figure 63, displaying 68% and 95% confidence level (CL) contours in the space of the parameters P_x and P_z, for both top quark and top anti-quark, summarizes the measurement.

Contribution	Extracted value: stat.+syst. (stat.)
t-channel	1.04 +0.02 / -0.02
W+jets	1.12 +0.03 / -0.04
$t\bar{t}$	1.00 +0.01 / -0.01

Table 15: The data/MC scale factors of the t-channel, W+jets and $t\bar{t}$ events. They are measured from a fit on data from signal and control regions, with full statistical and systematic uncertainties included. Note that these fitted values recovered the values from Table 13, acquired from an independent fit.

The impact of the most important groups of systematic uncertainties on the measured value of all polarisation parameters are shown in Tables 19-24. The uncertainties with the largest impact are those on the jet energy scale and resolution, followed by the t-channel modelling, the simulation statistics and the $t\bar{t}$+jets modelling. The small difference between the sum in quadrature of the individual groups and the total uncertainty is due to rounding effects and small correlations between the individual groups.

P component	Extracted value: stat.+syst. (stat.)
P_x^t	0.13 +0.11 / -0.11 ($\pm$ 0.02)
P_y^t	-0.03 +0.02 / -0.02 ($\pm$ 0.01)
P_z^t	0.93 +0.08 / -0.08 ($\pm$ 0.02)
$P_x^{\bar{t}}$	-0.12 +0.09 / -0.10 ($\pm$ 0.03)
$P_y^{\bar{t}}$	-0.01 +0.03 / -0.03 ($\pm$ 0.02)
$P_z^{\bar{t}}$	-0.84 +0.09 / -0.09 ($\pm$ 0.03)

Table 16: Polarization of the top quark and anti-quark extracted from the Run 2 dataset, from a fit with full statistical and systematic uncertainties included, as well as statistical only.

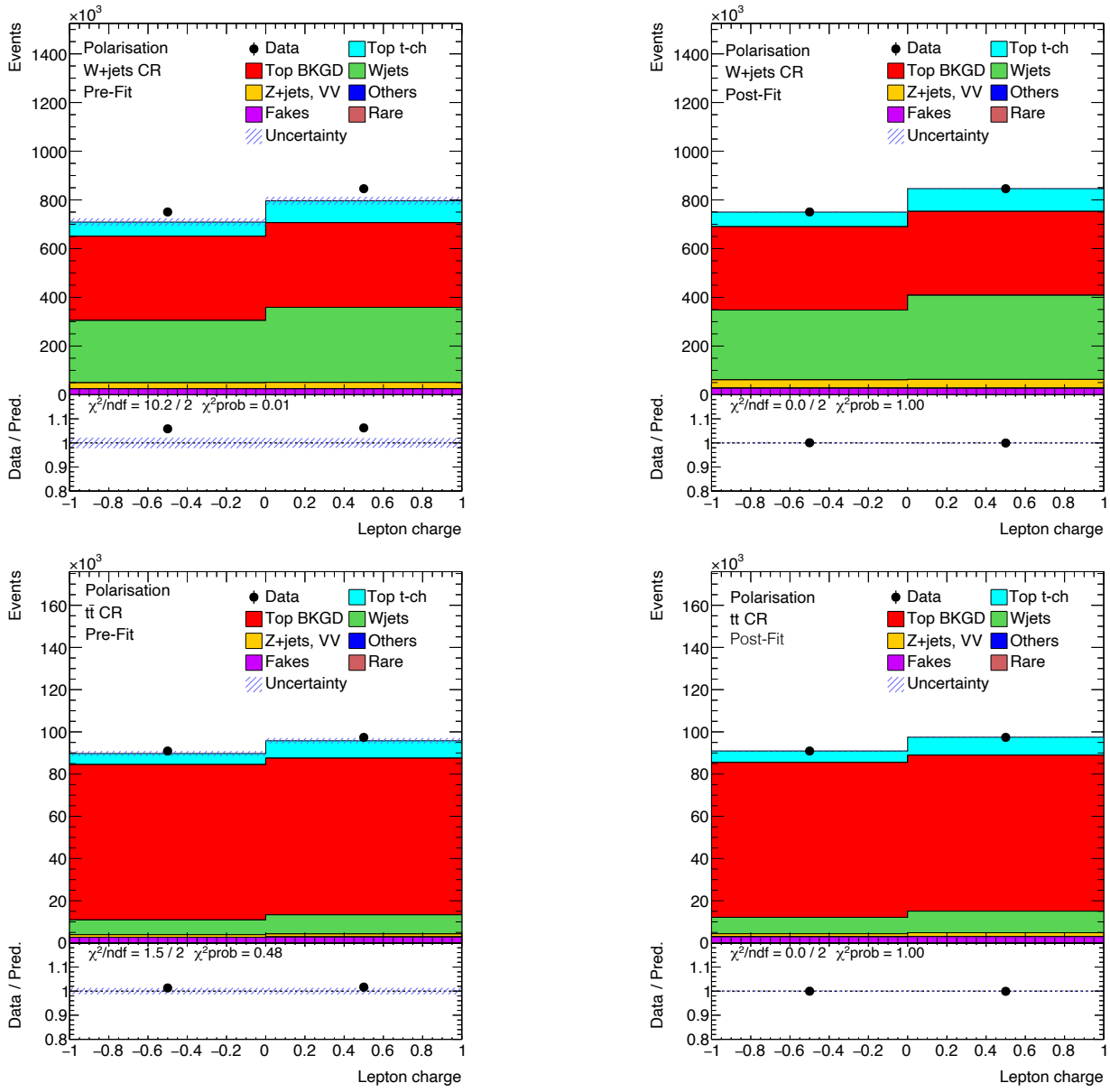

Figure 61: Observed (points with uncertainty bars) and expected (histograms) number of events separated by the lepton charge in the W+jets (a), $t\bar{t}$ (b) control regions, pre- (left) and post-fit (right). The background contributions after the global fit are shown as filled histograms. The t-channel signal (for different polarisations hypotheses) is shown as a filled histogram on top of the fitted backgrounds scaled according to the results of the fit. The size of the combined statistical and systematic uncertainty on the sum of the signal and fitted background is indicated by the blue hatched band. The ratio of the data to the sum of the signal and fitted background is shown in the lower panel.

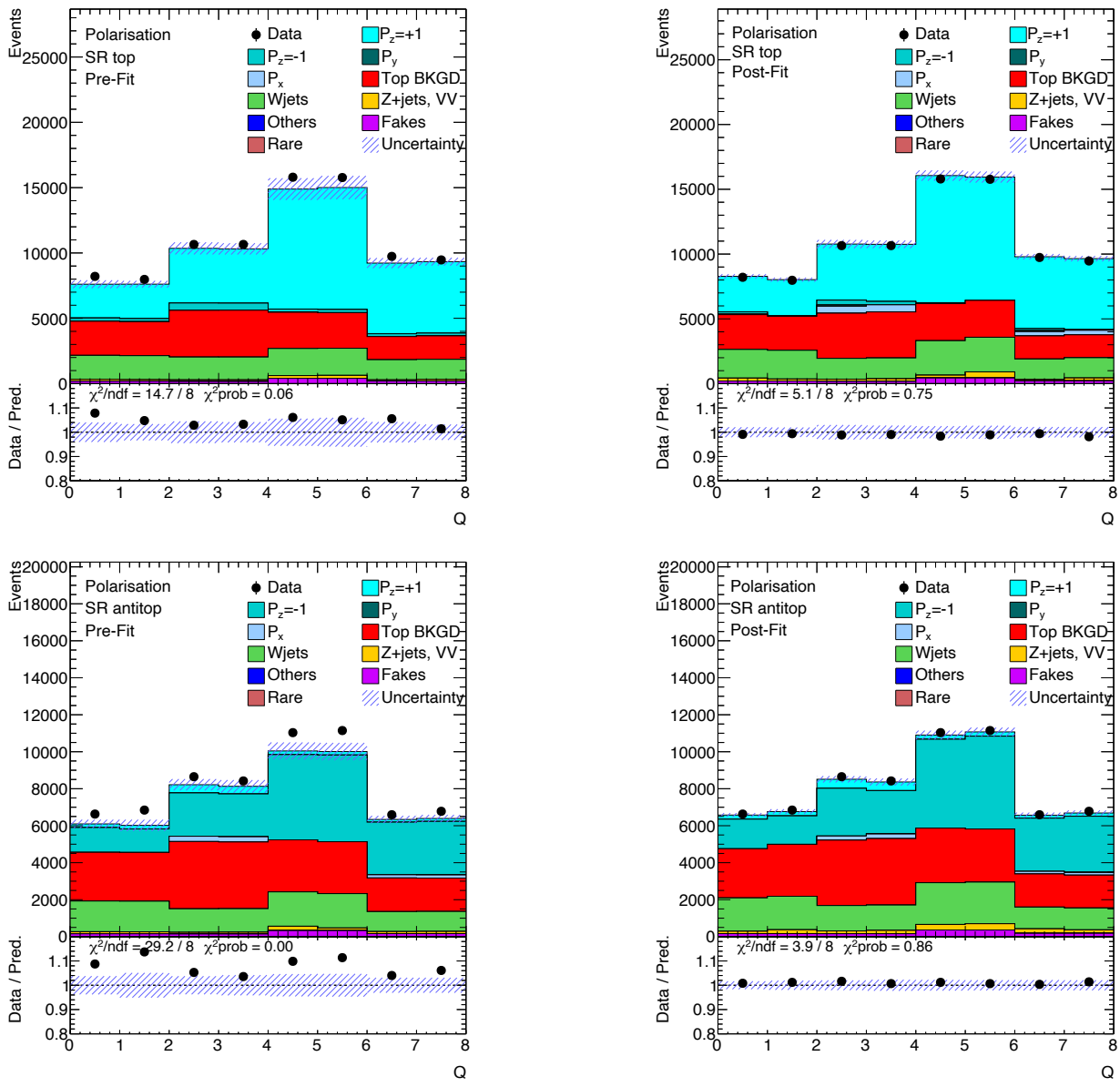

Figure 62: Observed (points with uncertainty bars) and expected (histograms) distribution of the discriminant variables in the (a) top-quark and (b) top-antiquark signal regions, pre- (left) and post-fit (right). The background contributions after the global fit are shown as filled histograms. The t-channel signal (for different polarization hypotheses) is shown as a filled histogram on top of the fitted backgrounds scaled according to the results of the fit. The size of the combined statistical and systematic uncertainty on the sum of the signal and fitted background is indicated by the blue hatched band. The ratio of the data to the sum of the signal and fitted background is shown in the lower panel.

	W+jets CR	$t\bar{t}$ CR	SR (top quark)	SR (top antiquark)
t-channel	148 150(210)	13 480(60)	0(0)	0(0)
$P_z = +1$	0(0)	0(0)	42 900(400)	1920(34)
$P_z = -1$	0(0)	0(0)	2529(35)	23 000(400)
P_y	0(0)	0(0)	0(0)	0(0)
P_x	0(0)	0(0)	0(0)	195(22)
s-channel	8420(300)	3510(250)	180(21)	187(14)
tW	90 000(6000)	4500(600)	2120(270)	2140(240)
$t\bar{t}$	594 840(300)	139 760(150)	19 120(50)	19 420(60)
W+jets	564 300(9000)	16 100(500)	14 400(900)	11 700(900)
Z+jets	41 000(4000)	1620(180)	930(180)	840(200)
Diboson	9900(3000)	990(310)	200(60)	160(50)
Multijet (electrons)	36 000(15000)	3400(1400)	1200(5000)	1000(400)
Multijet (muons)	12 000(9000)	2100(1500)	700(500)	500(400)
Total expected	1 505 000(21000)	185 500(2300)	84 300(1300)	61 200(1200)
Data	1596557	188326	88263	66098
Data/MC	1.040(39)	1.000(32)	1.030(31)	1.050(35)

Table 17: Pre-fit background, signal and observed yields in the four analysis regions in 139.0 fb^{-1} of data at $\sqrt{s} = 13$. Uncertainties in the background expectations due to systematic effects and MC statistics are shown. Multijet (electrons) and multijet (muons) refer to the data-driven background estimates. Rare processes (tZ, tW, tWZ, $t\bar{t}WW$, triboson production, $t\bar{t}t$, $t\bar{t}t\bar{t}$, tH) and processes with very small yields ($t\bar{t}Z$, $t\bar{t}W$ and $t\bar{t}H$) are not shown as a separate column but are included in the total expected background estimate.

	W+jets CR	$t\bar{t}$ CR	SR (top quark)	SR (top antiquark)
t-channel	148 150(210)	13 480(60)	0(0)	0(0)
$P_z = +1$	0(0)	0(0)	42 900(400)	1920(34)
$P_z = -1$	0(0)	0(0)	2530(40)	23 000(400)
$P_y = +1$	0(0)	0(0)	0(0)	0(0)
$P_x = +1$	0(0)	0(0)	0(0)	195(45)
s-channel	8420(300)	3510(250)	180(21)	187(14)
tW	90 000(6000)	4500(600)	2120(270)	2140(240)
$t\bar{t}$	594 840(300)	139 760(150)	19 120(50)	19 420(60)
W+jets	564 000(9000)	16 100(500)	14 400(900)	11 700(900)
Z+jets	41 000(4000)	1620(180)	930(180)	840(200)
Diboson	9900(2900)	990(300)	200(60)	160(50)
Multijet (electrons)	36 000(15000)	3400(1400)	1200(500)	1000(400)
Multijet (muons)	12 000(9000)	2100(1500)	700(500)	500(400)
Total	1 505 000(21000)	185 500(2300)	84 300(1300)	61 200(1200)
Data	1596557	188326	88263	66098
Data/MC	1.040(1)	1.000(3)	1.030(5)	1.050(4)

Table 18: Post-fit background, signal and observed yields in the four analysis regions in 139.0 fb^{-1} of data at $\sqrt{s} = 13$. Uncertainties in the background expectations due to systematic effects and MC statistics are shown. The uncertainty on the total background estimation is smaller than for the pre-fit values due to anti-correlations between the NPs obtained during the fit.

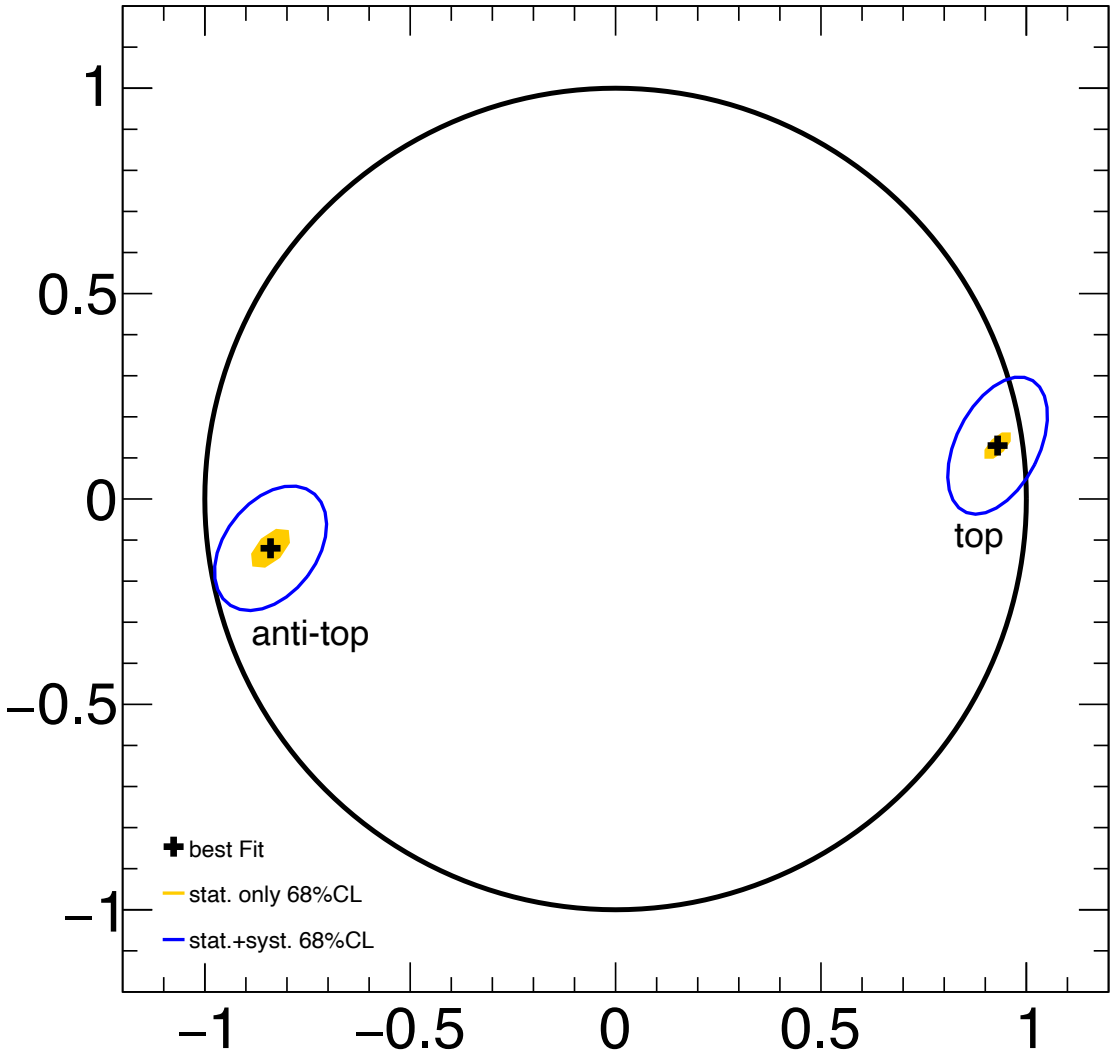

Figure 63: Summary of the measured polarizations with their statistical and systematic contours at 68% CL, plotted on the two-dimensional polarization phase space (P_z, P_x). The interior of the black circle represents the physically allowed region of parameter space.

Uncertainty source	ΔP_z^t	
t-channel modelling (cross-section, FS vs. AFII)	+0.046	-0.046
Jet energy scale	+0.046	-0.044
Jet energy resolution	+0.041	-0.038
Non-prompt light-lepton estimates	+0.003	-0.003
Jet flavour tagging	+0.006	-0.006
$t\bar{t}$+jets modelling	+0.007	-0.006
Other background modelling	+0.010	-0.009
Luminosity	+0.002	-0.002
Other experimental uncertainties	+0.023	-0.021
Simulation statistics	+0.026	-0.025
Total systematic uncertainty	+0.08	-0.08

Table 19: Summary of the effects of the most important groups of systematic uncertainties in P_z^t. Due to rounding effects and small correlations between the different sources of uncertainties, the total systematic uncertainty can be different from the sum in quadrature of the individual sources.

Uncertainty source	$\Delta P_z^{\bar{t}}$	
t-channel modelling (cross-section, FS vs. AFII)	+0.036	-0.037
Jet energy scale	+0.025	-0.024
Jet energy resolution	+0.043	-0.045
Non-prompt light-lepton estimates	+0.005	-0.005
Jet flavour tagging	+0.011	-0.010
$t\bar{t}$+jets modelling	+0.017	-0.016
Other background modelling	+0.024	-0.023
Luminosity	+0.001	-0.001
Other experimental uncertainties	+0.027	-0.027
Simulation statistics	+0.032	-0.033
Total systematic uncertainty	+0.09	-0.09

Table 20: Summary of the effects of the most important groups of systematic uncertainties in $P_z^{\bar{t}}$. Due to rounding effects and small correlations between the different sources of uncertainties, the total systematic uncertainty can be different from the sum in quadrature of the individual sources.

Uncertainty source	ΔP_x^t	
t-channel modelling (cross-section, FS vs. AFII)	+0.048	-0.044
Jet energy scale	+0.071	-0.062
Jet energy resolution	+0.063	-0.062
Non-prompt light-lepton estimates	+0.003	-0.003
Jet flavour tagging	+0.003	-0.003
$t\bar{t}$+jets modelling	+0.023	-0.023
Other background modelling	+0.011	-0.011
Luminosity	+0.002	-0.002
Other experimental uncertainties	+0.027	-0.028
Simulation statistics	+0.045	-0.042
Total systematic uncertainty	+0.11	-0.11

Table 21: Summary of the effects of the most important groups of systematic uncertainties in P_x^t. Due to rounding effects and small correlations between the different sources of uncertainties, the total systematic uncertainty can be different from the sum in quadrature of the individual sources.

Uncertainty source	$\Delta P_x^{\bar{t}}$	
t-channel modelling (cross-section, FS vs. AFII)	+0.046	-0.048
Jet energy scale	+0.045	-0.049
Jet energy resolution	+0.049	-0.051
Non-prompt light-lepton estimates	+0.010	-0.008
Jet flavour tagging	+0.006	-0.008
$t\bar{t}$+jets modelling	+0.022	-0.023
Other background modelling	+0.017	-0.018
Luminosity	+0.005	-0.005
Other experimental uncertainties	+0.038	-0.038
Simulation statistics	+0.031	-0.034
Total systematic uncertainty	+0.09	-0.10

Table 22: Summary of the effects of the most important groups of systematic uncertainties in $P_x^{\bar{t}}$. Due to rounding effects and small correlations between the different sources of uncertainties, the total systematic uncertainty can be different from the sum in quadrature of the individual sources.

Uncertainty source	ΔP_y^t	
t-channel modelling (cross-section, FS vs. AFII)	+0.004	-0.003
Jet energy scale	+0.006	-0.006
Jet energy resolution	+0.008	-0.008
Non-prompt light-lepton estimates	+0.001	-0.002
Jet flavour tagging	+0.001	-0.001
$t\bar{t}$+jets modelling	+0.004	-0.004
Other background modelling	+0.003	-0.003
Luminosity	+0.001	-0.001
Other experimental uncertainties	+0.004	-0.004
Simulation statistics	+0.008	-0.009
Total systematic uncertainty	+0.02	-0.02

Table 23: Summary of the effects of the most important groups of systematic uncertainties in P_y^t. Due to rounding effects and small correlations between the different sources of uncertainties, the total systematic uncertainty can be different from the sum in quadrature of the individual sources.

Uncertainty source	$\Delta P_y^{\bar{t}}$	
t-channel modelling (cross-section, FS vs. AFII)	+0.005	-0.005
Jet energy scale	+0.008	-0.007
Jet energy resolution	+0.006	-0.006
Non-prompt light-lepton estimates	+0.001	-0.001
Jet flavour tagging	+0.001	-0.001
$t\bar{t}$+jets modelling	+0.012	-0.012
Other background modelling	+0.003	-0.003
Luminosity	+0.001	-0.001
Other experimental uncertainties	+0.005	-0.006
Simulation statistics	+0.014	-0.014
Total syst ematic uncertainty	+0.03	-0.03

Table 24: Summary of the effects of the most important groups of systematic uncertainties in $P_y^{\bar{t}}$. Due to rounding effects and small correlations between the different sources of uncertainties, the total systematic uncertainty can be different from the sum in quadrature of the individual sources.

3.8.1 Likelihood Curves

The likelihood profiles as a function of P_x^t, P_y^t, P_z^t, $P_x^{\bar{t}}$, $P_y^{\bar{t}}$ and $P_z^{\bar{t}}$ for the fit to data are shown in Figure 64. The distributions are smooth and show no irregularities.

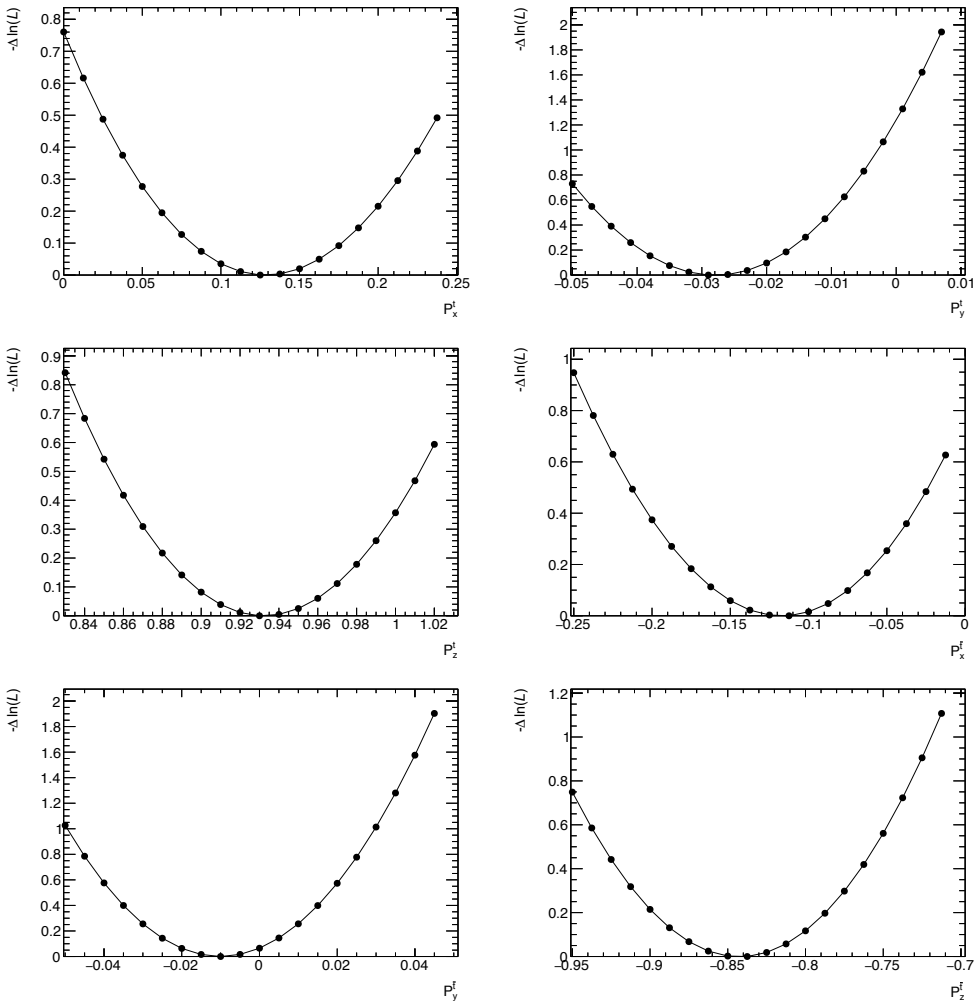

Figure 64: Logarithmic likelihood scans as a function of P_x^t, P_y^t, P_z^t, $P_x^{\bar{t}}$, $P_y^{\bar{t}}$ and $P_z^{\bar{t}}$ for the fit to data.

3.9 Conclusion

The analysis presented in this thesis uses the template fit method to perform the measurement of the top quark and anti-quark polarization in the single top t-channel. The fitting templates are obtained from a new decay model which permits us to modify the spin of the top quark prior to decay. This measurement extracts the polarization of reconstructed top quarks and anti-quarks produced within our acceptance for the first time, using an integrated luminosity 139 fb^{-1} of proton-proton collisions at 13 TeV, collected by the ATLAS detector. The selected events contain one isolated electron or muon, large $E_{\mathrm{T}}^{\mathrm{miss}}$ and exactly two jets, with one of them identified as likely to contain a b-hadron. A cut-based analysis is used to discriminate the signal events from background, with electron and muon channels merged. From the angular distribution of top quark decay products, we obtain all three components of the polarization of both top quarks and top anti-quarks. The top quark is measured to be polarized as $P_z = (0.85, 1.01)$, $P_x = (0.02, 0.24)$, and $P_y = (-0.05, -0.01)$ with 68% confidence level (C.L.), while the top anti-quark is polarized as $P_z = (-0.93, -0.75)$, $P_x = (-0.22, -0.03)$, $P_y = (-0.04, 0.02)$ with 68% C.L.. All of the measurements are under fine agreement with the SM expectations.

In terms of the BSM effects — more specifically, the top anomalous couplings and four-fermion interactions, limits of their contributions in the fiducial region can be calculated from this result. For now, the P_x and P_y polarizations including systematic uncertainties are consistent with zero, indicating little evidence for the g_R anomalous coupling. The P_z polarization is within the expectation of the SM values, suggesting a low probability of observing four-fermion interactions incorporated by a right-handed top quark.

Appendix A Determination of the Longitudinal Momentum of the Neutrino

The four-momentum conservation law for the leptonic W boson decay (i.e. $W \to \ell\nu$, standing ℓ for a lepton) gives the following expression:

$$(p^W)^2 = (p^\ell + p^\nu)^2 \quad \to \quad m_W^2 = m_\ell^2 + 2(E^\ell, \mathbf{p}^\ell)(E^\nu, \mathbf{p}^\nu) = m_\ell^2 + 2(E^\ell E^\nu - \mathbf{p}^\ell \cdot \mathbf{p}^\nu) \,, \quad (71)$$

where p, m, E and $\mathbf{p}$ represent the four-momentum, the mass, the energy and the momentum of a given particle. In addition, the superscripts W, ℓ and ν represent the W boson, the lepton (either electron, muon or tau) and the neutrino. Note that in Eq. (71) the neutrino mass has been neglected ($m_\nu = 0$). Now, using the hypothesis that transverse energy in the centre-of-mass of the collision is equal to zero, then the E_T^{miss} in the detector can be approximated as due just to the neutrino, i.e. $E_T^{\text{miss}} = p_T^\nu$. Following with the kinematics, the neutrino energy can be expressed as:

$$(E^\nu)^2 = (p_x^\nu)^2 + (p_y^\nu)^2 + (p_z^\nu)^2 = (p_T^\nu)^2 + (p_z^\nu)^2 \,,$$

$$E^\nu = \sqrt{(E_T^{\text{miss}})^2 + (p_z^\nu)^2} \,,$$

and its transverse momentum components are given by:

$$p_x^\nu = E_T^{\text{miss}} cos\phi_{\,E_T^{\text{miss}}} \quad \text{and} \quad p_y^\nu = E_T^{\text{miss}} sin\phi_{\,E_T^{\text{miss}}} \,, \quad (72)$$

therefore the m_W^2 expression from Eq. (71) becomes:

$$m_W^2 = m_\ell^2 + 2E^\ell E^\nu - 2\left(p_x^\ell p_x^\nu + p_y^\ell p_y^\nu + p_z^\ell p_z^\nu\right) \quad (73)$$

$$= m_\ell^2 + 2E^\ell \sqrt{(E_T^{\text{miss}})^2 + (p_z^\nu)^2} - 2\left(E_T^{\text{miss}}\left(p_x^\ell \cos\phi_{\,E_T^{\text{miss}}} + p_y^\ell \sin\phi_{\,E_T^{\text{miss}}}\right) + p_z^\ell p_z^\nu\right) \,. \quad (74)$$

Since the neutrino stems from an on-shell W boson, one can use its pole-mass of 80.399 $\pm$ 0.023 GeV [51] as a reference mass value for m_W, and therefore the only unknown quantity left

in Eq. (74) is the neutrino longitudinal momentum (p_z^ν). Working out p_z^ν from Eq. (74) a quadratic expression is found:

$$a(p_z^\nu)^2 + bp_z^\nu + c = 0 \;\; \rightarrow \;\; \begin{cases} a = (E^\ell)^2 - (p_z^\ell)^2 \; . \\ \\ b = p_z^\ell \left(-m_W^2 + m_\ell^2 - 2(p_x^\ell p_x^\nu + p_y^\ell p_y^\nu)\right) \; . \\ \\ c = (E^\ell)^2 (E_T^{\text{miss}})^2 - \frac{1}{4}\left(m_W^2 - m_\ell^2 + 2(p_x^\ell p_x^\nu + p_y^\ell p_y^\nu)\right)^2 \; . \end{cases}$$

Being the solutions:

$$p_z^\nu = \frac{-p_z^\ell \left(-m_W^2 + m_\ell^2 - 2(p_x^\ell p_x^\nu + p_y^\ell p_y^\nu)\right) \pm \sqrt{\Delta}}{2\left((E^\ell)^2 - (p_z^\ell)^2\right)} \; , \tag{75}$$

where Δ the discriminant defined as:

$$\Delta \equiv (E^\ell)^2 \left[\left(m_W^2 - m_\ell^2 + 2(p_x^\ell p_x^\nu + p_y^\ell p_y^\nu)\right)^2 + 4(E_T^{\text{miss}})^2(-(E^\ell)^2 + \left(p_z^\ell\right)^2)\right] \; .$$

On the one hand, if the two solutions are real, the solution giving the smallest magnitude of the longitudinal neutrino momentum is taken. On the other hand, sometimes $\Delta < 0$. This is due to the fact that the assumption that the neutrino is the only contributor to the E_T^{miss} is not valid and therefore p_z^ν is overestimated. If that happens, there are several options to solve the problem:

- If a complex solution is found one could claim that this solution is unphysical, assume $\Delta = 0$ and then choose the single p_z^ν value.
- Another solution is decreasing the E_T^{miss} (i.e. p_T^ν) step by step until a real pair of solutions is found. This decreasing can be done within the E_T^{miss} resolution using the MC information as done in Ref. [73] or using the restriction that m_t^W has to remain below 90 GeV [74].

- Finally, another option is finding for which values of the E_T^{miss} the Δ term becomes positive. By doing so, one just scales E_T^{miss} but preserves its direction $(\cos\phi_{E_T^{\text{miss}}}, \sin\phi_{E_T^{\text{miss}}})$. To do this one can solve the discriminant equation (i.e. $\Delta = 0$) in terms of E_T^{miss}, and denoted as $E_T^{\prime\text{miss}}$. Of course, two solutions are obtained from this equation as follows:

$$E_T^{\text{miss}} = \frac{-(-m_W^2 + m_\ell^2)(p_x^\ell \cos\phi_{\ E_T^{\text{miss}}} + p_y^\ell \sin\phi_{\ E_T^{\text{miss}}}) \pm (-m_W^2 + m_\ell^2)\sqrt{(E^\ell)^2 - (p_z^\ell)^2}}{2\left[(E^\ell)^2 - (p_z^\ell)^2 - (p_x^\ell \cos\phi_{\ E_T^{\text{miss}}} + p_y^\ell \sin\phi_{\ E_T^{\text{miss}}})^2\right]} \,. \tag{76}$$

  If just one solution for $E_T^{\prime\text{miss}}$ is positive, this is the one which is chosen. If the two solutions for $E_T^{\prime\text{miss}}$ are positive, the one closer to the initial E_T^{miss} is taken. Once this new $E_T^{\prime\text{miss}}$ is calculated it is increased by a few eV in order to have $\Delta > 0$ and it is used in Eq. (75) to finally compute the p_z^ν solutions. Now the two solutions for p_z^ν are real and therefore the solution giving the smallest magnitude of the longitudinal neutrino momentum is taken.

Appendix B Event Yields and Distributions

B.1 Event Yields

The pre-fit total expected and observed event yields for the preselection and signal regions and for the two control regions for electrons and muons combined together are shown in Table 25, where each physics processes is listed. The uncertainties are statistical uncertainties only.

Table 26 shows the pre-fit total expected and observed event yields for the pre-selection and signal regions and in the two control regions for electrons and muons separately, where the uncertainties are statistical uncertainties only.

Table 27 shows the pre-fit total expected and observed event yields for the preselection and signal regions and in the two control regions for top-quarks and top-antiquarks separately, where the uncertainties are statistical uncertainties only.

Process	Preselection region	Signal region	$t\bar{t}$ control region	W+jets control region
t-channel	218752 ± 259	70601 ± 147	13479 ± 65	148150 ± 213
$t\bar{t}$	633384 ± 314	38544 ± 78	139757 ± 146	594839 ± 304
tW	94267 ± 165	4265 ± 35	4510 ± 36	90002 ± 161
s-channel	8791 ± 17	368 ± 3	3507 ± 11	8424 ± 17
W+b-jets	372994 ± 849	13298 ± 180	15162 ± 137	359696 ± 829
W+c-jets	185238 ± 1689	11651 ± 456	571 ± 84	173587 ± 1627
W+light-jets	28069 ± 1061	1181 ± 228	234 ± 82	26888 ± 1037
W+mixed-jets	4396 ± 27	24 ± 2	152 ± 5	4371 ± 26
Z+jets	42697 ± 331	1768 ± 67	1624 ± 36	40930 ± 324
Diboson	10209 ± 48	353 ± 9	993 ± 11	9855 ± 47
tZq	32 ± 0	7 ± 0	1 ± 0	25 ± 0
$t\bar{t}Z$	226 ± 2	11 ± 1	41 ± 1	214 ± 2
$t\bar{t}W$	182 ± 1	7 ± 0	26 ± 0	175 ± 1
tHq	22 ± 1	4 ± 0	5 ± 1	18 ± 1
$t\bar{t}H$	62 ± 0	2 ± 0	18 ± 0	60 ± 0
tWZ	5 ± 0	0 ± 0	0 ± 0	4 ± 0
Multijet	88708 ± 1300	6643 ± 283	8266 ± 473	82064 ± 1268
Total expected	1688031 ± 2587	148727 ± 636	188346 ± 533	1539303 ± 2507
Data	1750918 ± 1323	154361 ± 392	188326 ± 433	1596557 ± 1263
S/B	0.15	0.90	0.08	0.11
Data/MC	1.04	1.04	1.00	1.04

Table 25: Pre-fit event yields in the preselection and signal regions and in the $t\bar{t}$ control and W+jets control regions. The predictions are derived from simulated event samples together with their theoretical cross-section except multijet which normalisation is estimated from a data-driven likelihood fit. No overall normalisation scale factors are considered to compute these event yields. The uncertainties shown are statistical only. Yields and uncertainties of less than 0.5 events appear as zero. Individual predictions are rounded to integers while "Total expected" corresponds to the rounding of the sum of full precision individual predictions. The expected S/B and Data/MC ratios are also given.

Process	Preselection region	Signal region	$t\bar{t}$ control region	W+jets control region
t-channel	111508 ± 187	37354 ± 109	6969 ± 47	74154 ± 152
$t\bar{t}$	334389 ± 230	21048 ± 58	73806 ± 107	313341 ± 223
tW	49695 ± 121	2302 ± 26	2387 ± 27	47393 ± 118
s-channel	4375 ± 12	186 ± 2	1782 ± 8	4190 ± 12
W+heavy-jets	289398 ± 1324	13550 ± 365	8431 ± 112	275848 ± 1273
W+light-jets	14881 ± 745	633 ± 167	230 ± 65	14248 ± 726
Z+jets, diboson	25296 ± 230	1079 ± 50	1137 ± 23	24231 ± 225
Others	285 ± 2	17 ± 1	49 ± 1	268 ± 2
Multijet	55029 ± 1113	3555 ± 227	3634 ± 387	51474 ± 1089
Total expected	884856 ± 1923	79724 ± 480	98425 ± 425	805146 ± 1863
Data	916369 ± 957	83416 ± 288	99205 ± 314	832953 ± 912
S/B	0.14	0.88	0.08	0.10
Data/MC	1.04	1.05	1.01	1.03

Process	Preselection region	Signal region	$t\bar{t}$ control region	W+jets control region
t-channel	107243 ± 180	33247 ± 99	6510 ± 44	73996 ± 150
$t\bar{t}$	298994 ± 213	17496 ± 51	65884 ± 99	281498 ± 207
tW	44572 ± 112	1963 ± 24	2123 ± 24	42609 ± 110
s-channel	4416 ± 12	182 ± 2	1724 ± 8	4234 ± 12
W+heavy-jets	268834 ± 1350	11398 ± 327	7302 ± 115	257436 ± 1309
W+light-jets	17583 ± 757	572 ± 156	156 ± 51	17011 ± 741
Z+jets, diboson	27595 ± 242	1042 ± 46	1481 ± 30	26553 ± 238
Others	243 ± 2	14 ± 0	42 ± 1	229 ± 2
Multijet	33679 ± 187	3089 ± 57	4632 ± 86	30591 ± 178
Total expected	803160 ± 1605	69002 ± 386	89853 ± 191	734157 ± 1558
Data	834549 ± 913	70945 ± 266	89121 ± 298	763604 ± 873
S/B	0.15	0.93	0.08	0.11
Data/MC	1.04	1.03	0.99	1.04

Table 26: Event yields for the electron (top) and muon (bottom) channels in the preselection and signal regions and in the $t\bar{t}$ control and W+jets control regions. The predictions are derived from simulated event samples together with their theoretical cross-section except multijet which normalisation is estimated from a data-driven likelihood fit. No overall normalisation scale factors are considered to compute these event yields. The uncertainties shown are statistical only. Yields and uncertainties of less than 0.5 events appear as zero. Individual predictions are rounded to integers while "Total expected" corresponds to the rounding of the sum of full precision individual predictions. The expected S/B and Data/MC ratios are also given.

Process	Preselection region	Signal region	$t\bar{t}$ control region	W+jets control region
t-channel	135263 ± 222	45454 ± 127	8250 ± 55	89809 ± 181
$t\bar{t}$	316703 ± 222	19122 ± 55	69836 ± 103	297581 ± 215
tW	47187 ± 117	2120 ± 25	2280 ± 26	45066 ± 114
s-channel	5259 ± 15	180 ± 3	2080 ± 9	5079 ± 14
W+heavy-jets	304153 ± 1373	13856 ± 359	8818 ± 115	290297 ± 1325
W+light-jets	18770 ± 785	553 ± 171	243 ± 67	18218 ± 766
Z+jets, diboson	27165 ± 235	1129 ± 48	1424 ± 29	26037 ± 230
Others	285 ± 2	17 ± 1	47 ± 1	267 ± 2
Multijet	45078 ± 914	3636 ± 210	4243 ± 331	41442 ± 889
Total expected	899862 ± 1871	86066 ± 473	97219 ± 377	813796 ± 1810
Data	934315 ± 966	88263 ± 297	97397 ± 312	846052 ± 919
S/B	0.18	1.12	0.09	0.12
Data/MC	1.04	1.03	1.00	1.04

Process	Preselection region	Signal region	$t\bar{t}$ control region	W+jets control region
t-channel	83488 ± 134	25148 ± 73	5229 ± 34	58341 ± 113
$t\bar{t}$	316681 ± 222	19422 ± 55	69921 ± 103	297258 ± 215
tW	47080 ± 117	2145 ± 25	2231 ± 25	44936 ± 114
s-channel	3532 ± 10	187 ± 2	1426 ± 6	3345 ± 9
W+heavy-jets	254080 ± 1300	11093 ± 334	6915 ± 112	242986 ± 1257
W+light-jets	13694 ± 715	653 ± 151	143 ± 48	13041 ± 699
Z+jets, diboson	25740 ± 238	992 ± 48	1193 ± 24	24748 ± 233
Others	243 ± 2	14 ± 0	44 ± 1	230 ± 2
Multijet	43630 ± 924	3008 ± 190	4024 ± 338	40623 ± 903
Total expected	788168 ± 1786	62661 ± 426	91126 ± 376	725507 ± 1735
Data	816603 ± 903	66098 ± 257	90929 ± 301	750505 ± 866
S/B	0.12	0.67	0.06	0.09
Data/MC	1.04	1.05	1.00	1.03

Table 27: Event yields for the top-quark (top) and top-antiquark (bottom) channels in the preselection and signal regions and in the $t\bar{t}$ control and W+jets control regions. The predictions are derived from simulated event samples together with their theoretical cross-section except multijet which normalisation is estimated from a data-driven likelihood fit. No overall normalisation scale factors are considered to compute these event yields. The uncertainties shown are statistical only. Yields and uncertainties of less than 0.5 events appear as zero. Individual predictions are rounded to integers while "Total expected" corresponds to the rounding of the sum of full precision individual predictions. The expected S/B and Data/MC ratios are also given.

Appendix C Template Fit with Custom Asimov Dataset

This section shows the fit results on custom Asimov datasets constructed by the nominal POWHEG-BOX+PYTHIA8, and the LO generator PROTOS+PYTHIA8. The backgrounds are all removed from the dataset and templates for a clean extraction. Only statistical uncertainties are included in these fits.

The expected polarizations are shown in Table 28.

SM sample	P Components	Extracted value + stat. (t)	Extracted value + stat. ($\bar{t}$)
POWHEG-BOX+PYTHIA8	P_x	0.040 ± 0.0120	-0.070 ± 0.0157
	P_y	-0.008 ± 0.0076	0.000 ± 0.0080
	P_z	1.024 ± 0.0150	-0.967 ± 0.0200
PROTOS+PYTHIA8	P_x	0.038 ± 0.0135	-0.068 ± 0.0018
	P_y	0.004 ± 0.0087	-0.015 ± 0.0112
	P_z	0.983 ± 0.0170	-0.944 ± 0.0230

Table 28: Polarisation of the top quark and antiquark samples estimated using POWHEG-BOX (NLO) and PROTOS (LO) generators. The measurements are performed on the signal solely.

C.1 Fit on POWHEG-BOX+PYTHIA8

The pre-fit and post-fit summary plots of the four regions are shown in Figure 65. Figures 66-67 show instead the distributions used in the fit, before and after performing the fit.

C.1.1 Likelihood Curves

The logarithmic likelihood scans as a function of P_x^t, P_y^t, P_z^t, $P_x^{\bar{t}}$, $P_y^{\bar{t}}$ and $P_z^{\bar{t}}$ for the fit to data are shown in Figure 68. The distributions are smooth and show no irregularities. The intersections

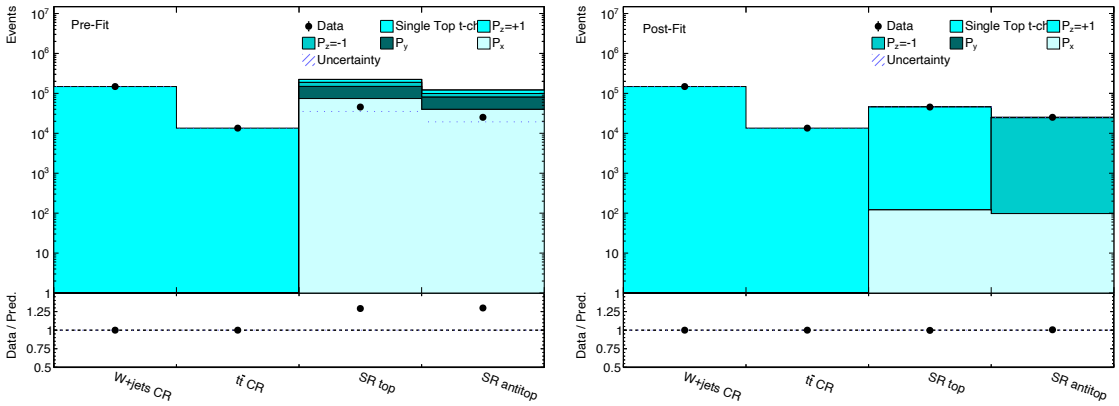

Figure 65: Comparison of the pre-fit and post-fit prediction to data in the four regions entering the profile likelihood fit. The statistical-only uncertainties on the predicted yields are indicated by the hashed blue bands.

of the curve with the horizontal dashed line at $-\Delta log(L) = 0.5$ correspond to the $\pm 1\sigma$ uncertainty on P_i.

C.2 Fit on PROTOS+PYTHIA8

The pre- and post-fit summary plots of the four regions are shown in Figure 69. Figures 70-71 show instead the distributions used in the fit, before and after performing the fit.

C.2.1 Likelihood Curves

The logarithmic likelihood scans as a function of P_x^t, P_y^t, P_z^t, $P_x^{\bar{t}}$, $P_y^{\bar{t}}$ and $P_z^{\bar{t}}$ for the fit to data are shown in Figure 68. The distributions are smooth and show no irregularities. The intersections of the curve with the horizontal dashed line at $-\Delta log(L) = 0.5$ correspond to the $\pm 1\sigma$ uncertainty on P_i.

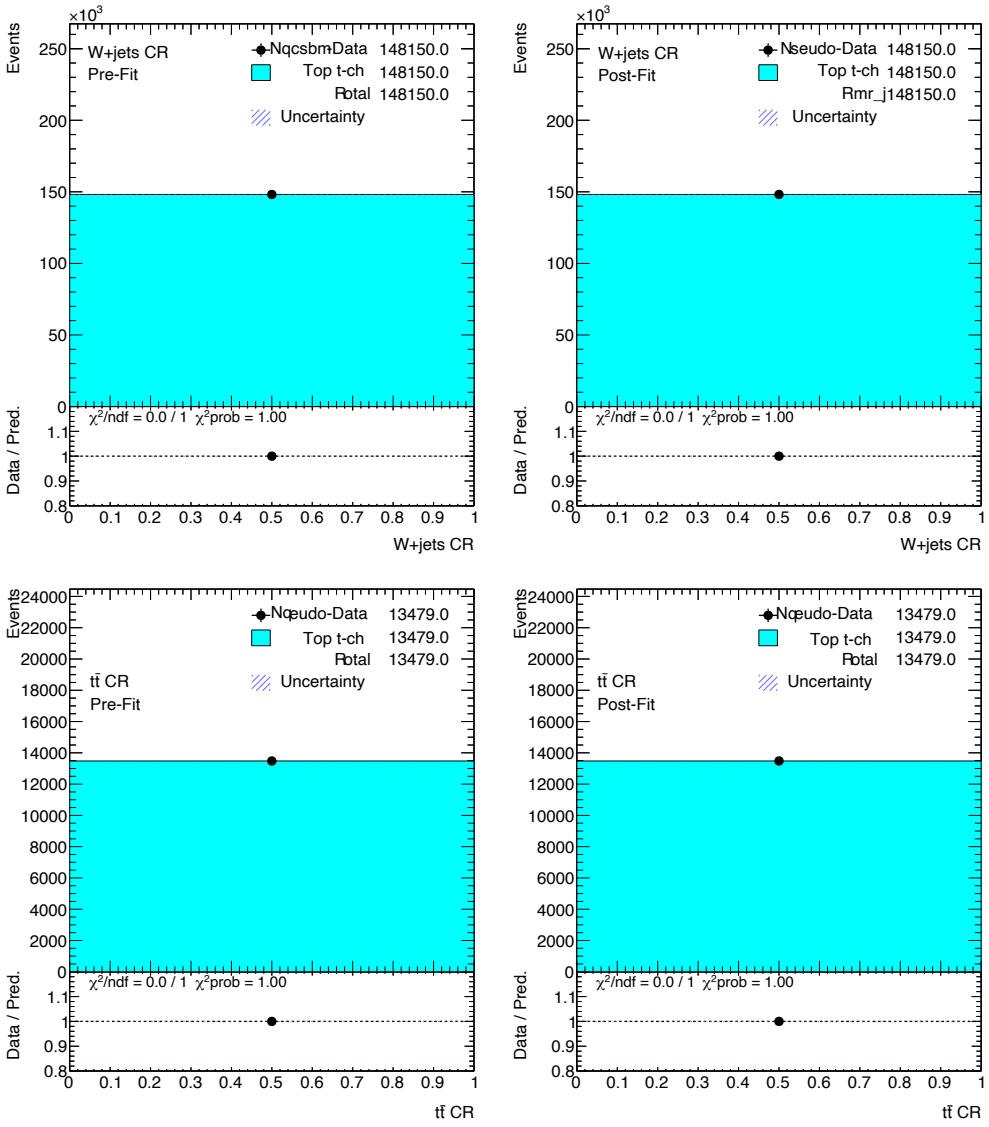

Figure 66: Observed (points with uncertainty bars) and expected (histograms) number of events in the pre-fit and post-fit W+jets control region and pre-fit and post-fit $t\bar{t}$ control region.

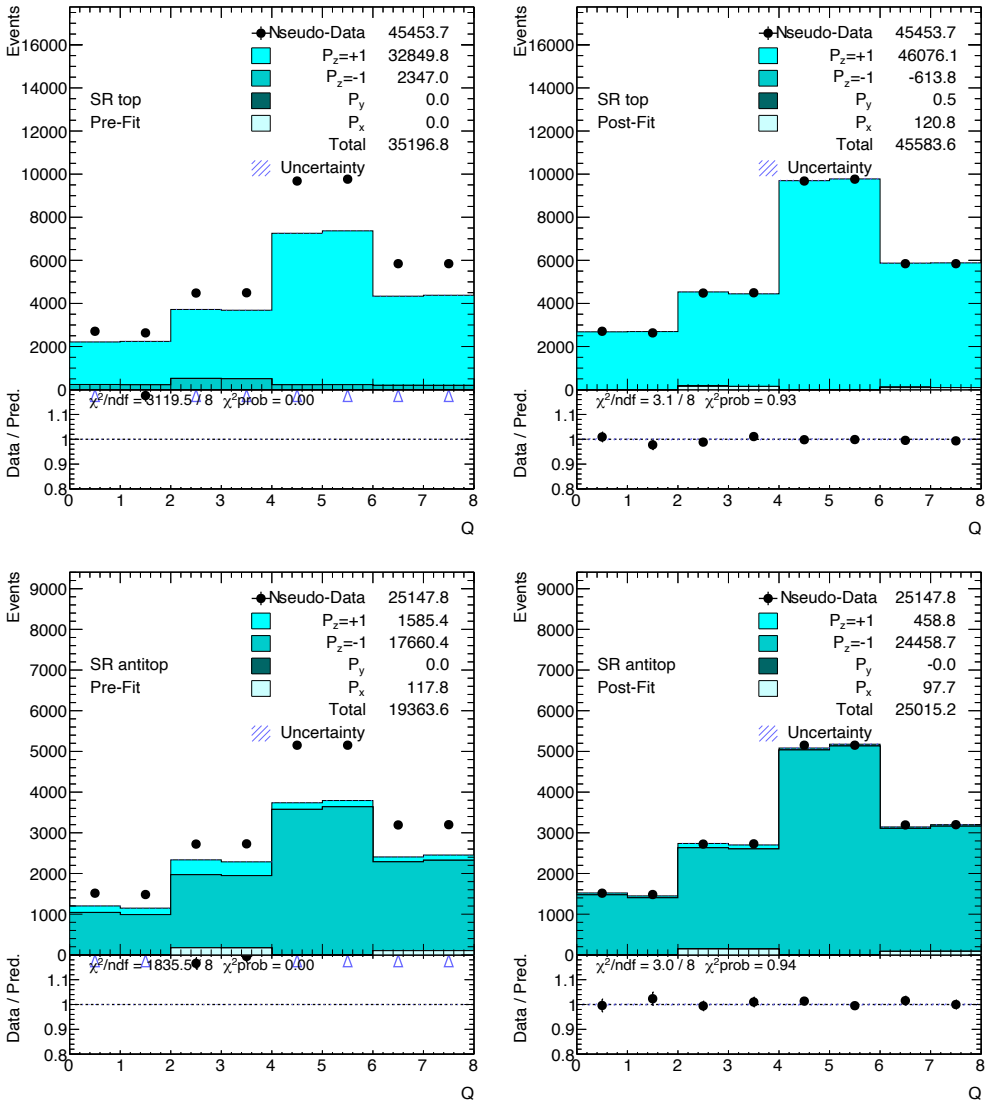

Figure 67: Observed (points with uncertainty bars) and expected (histograms) distribution of the discriminant variables Q in the pre-fit and post-fit in the top-quark signal region and pre-fit and post-fit in the top-quark signal region.

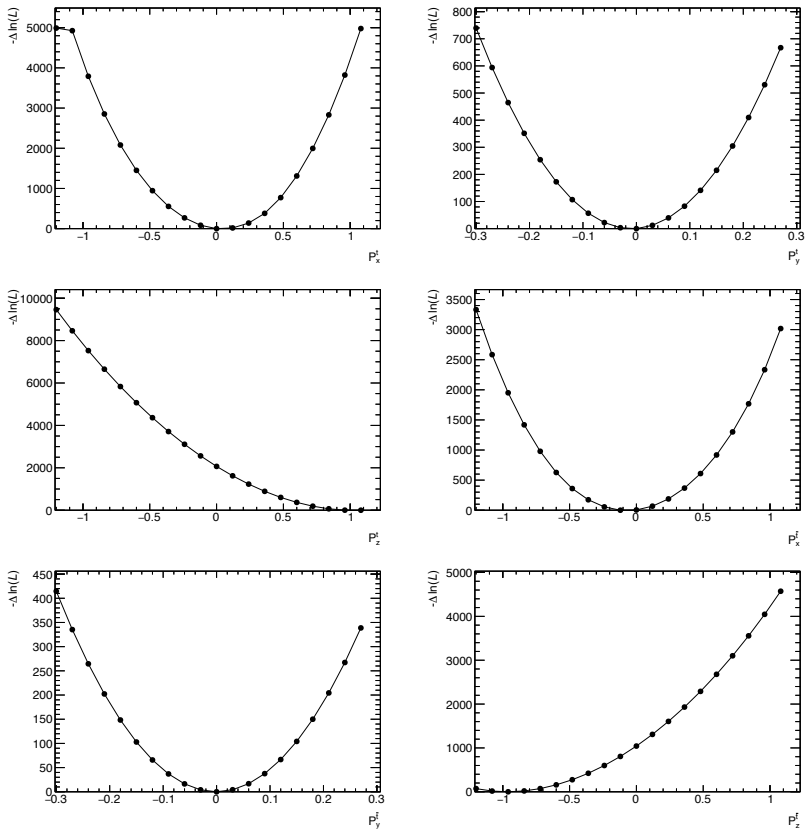

Figure 68: Logarithmic likelihood scans as a function of P_x^t, P_y^t, P_z^t, $P_x^{\bar{t}}$, $P_y^{\bar{t}}$ and $P_z^{\bar{t}}$ for the fit to data.

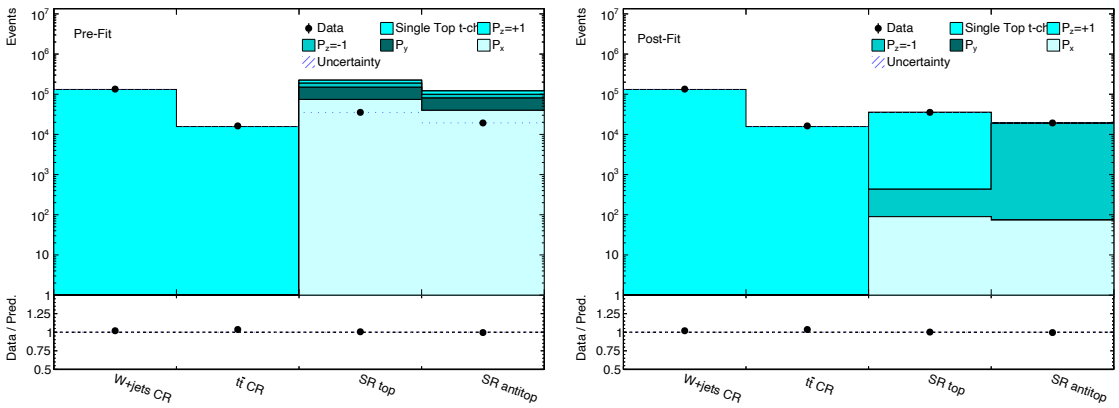

Figure 69: Comparison of the pre-fit and post-fit prediction to data in the four regions entering the profile likelihood fit. The statistical-only uncertainties on the predicted yields are indicated by the hashed blue bands.

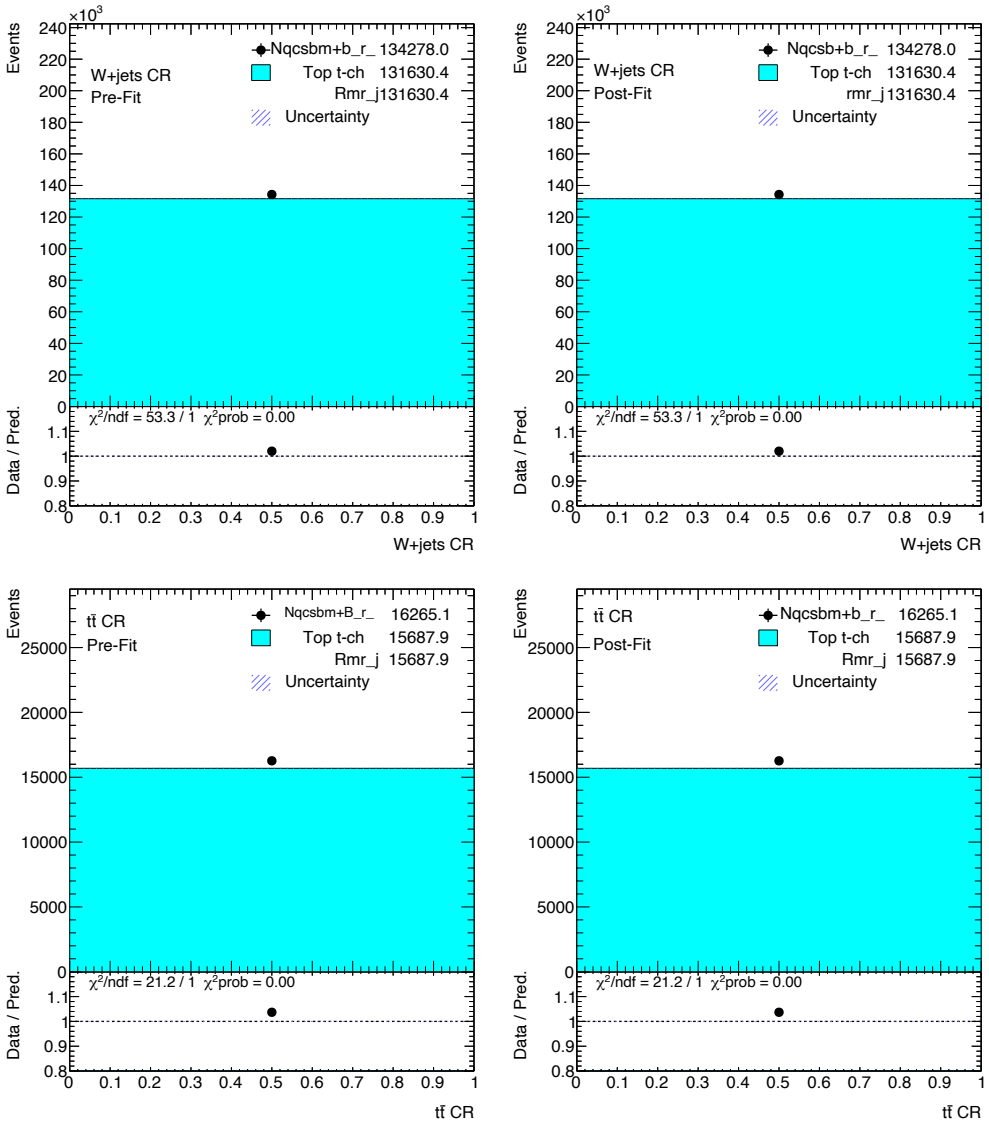

Figure 70: Observed (points with uncertainty bars) and expected (histograms) number of events in the pre-fit and post-fit W+jets control region and pre-fit and post-fit $t\bar{t}$ control region.

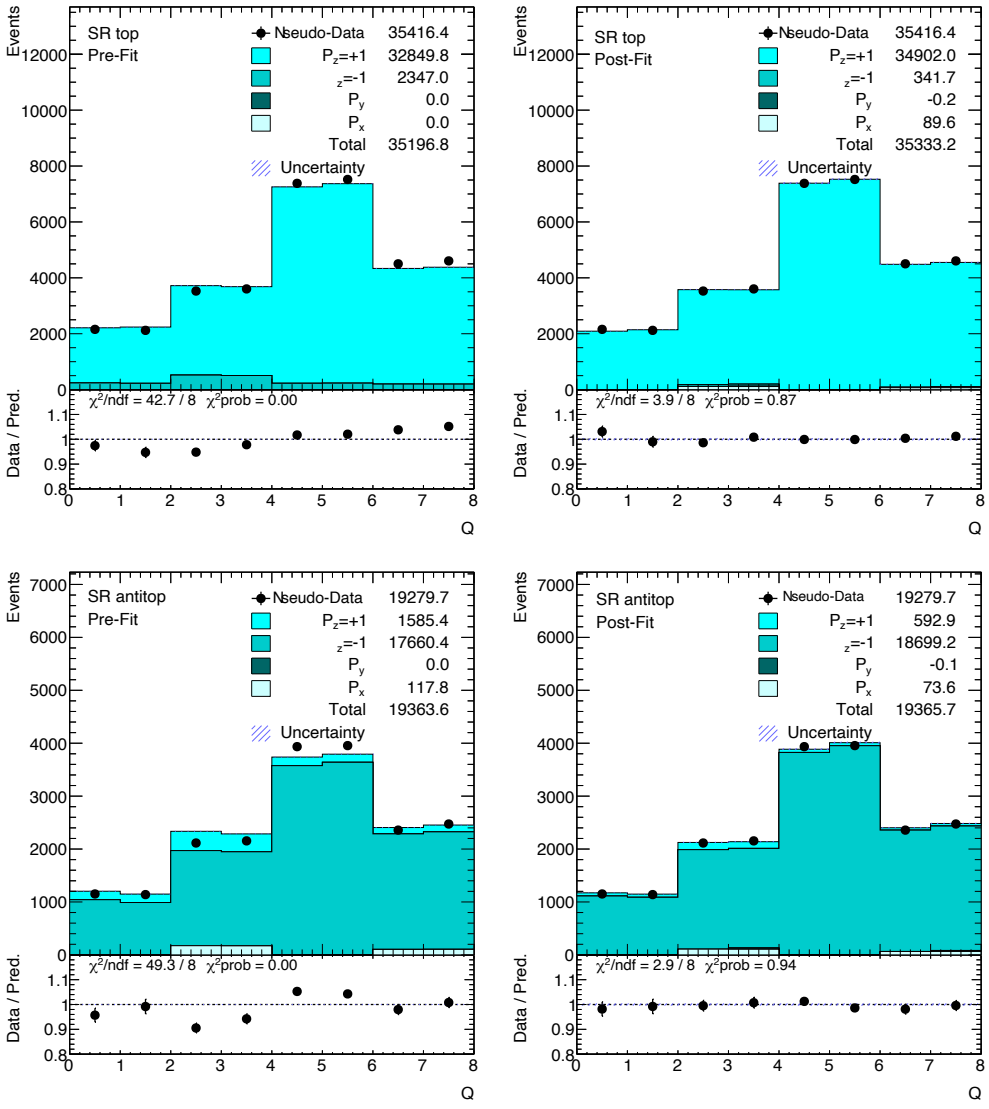

Figure 71: Observed (points with uncertainty bars) and expected (histograms) distribution of the discriminant variables Q in the pre-fit and post-fit in the top-quark signal region and pre-fit and post-fit in the top-quark signal region.

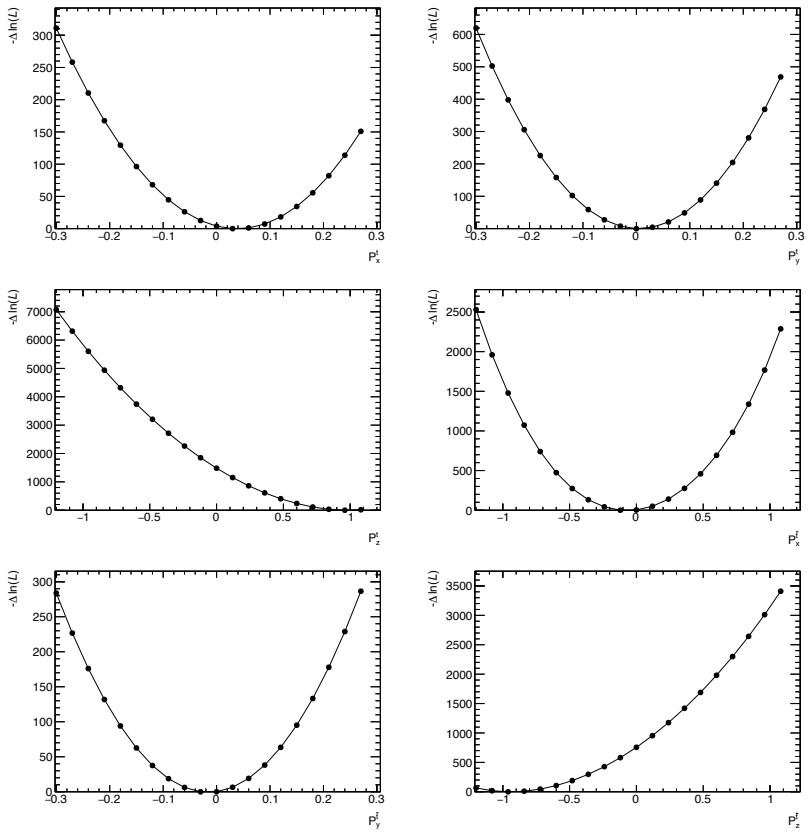

Figure 72: Logarithmic likelihood scans as a function of P_x^t, P_y^t, P_z^t, $P_x^{\bar{t}}$, $P_y^{\bar{t}}$ and $P_z^{\bar{t}}$ for the fit to data.

Bibliography

[1] J. J. Thomson. “Cathode Rays”. In: *Philosophical Magazine Series 5* 44.269 (1897).

[2] The ATLAS Collaboration. “Observation of a new particle in the search for the Standard Model Higgs boson with the ATLAS detector at the LHC”. In: *Physics Letters B* 716.1 (2012), pp. 1–29.

[3] The CMS Collaboration. “Observation of a new boson at a mass of 125 GeV with the CMS experiment at the LHC”. In: *Physics Letters B* 716.1 (2012), pp. 30–61.

[4] K.A. Olive. “Review of Particle Physics”. In: *Chinese Physics C* 40.10 (Oct. 2016).

[5] Michael E Peskin. *An introduction to quantum field theory*. CRC press, 2018.

[6] C. S. Wu, E. Ambler, R. W. Hayward, D. D. Hoppes, and R. P. Hudson. “Experimental Test of Parity Conservation in Beta Decay”. In: *Phys. Rev.* 105 (4 Feb. 1957), pp. 1413–1415.

[7] J. H. Christenson, J. W. Cronin, V. L. Fitch, and R. Turlay. “Evidence for the 2π Decay of the K_2^0 Meson”. In: *Phys. Rev. Lett.* 13 (4 July 1964), pp. 138–140.

[8] Mark Thomson. *Modern Particle Physics*. Cambridge University Press, 2013.

[9] F. Abe, H. Akimoto, A. Akopian, M. G. Albrow, S. R. Amendolia, D. Amidei, J. Antos, C. Anway-Wiese, S. Aota, G. Apollinari, and et al. “Observation of Top Quark Production in pp^- Collisions with the Collider Detector at Fermilab”. In: *Physical Review Letters* 74.14 (Apr. 1995), pp. 2626–2631.

[10] The D0 Collaboration. “Search for High Mass Top Quark Production in pp^- Collisions at s=1.8 TeV”. In: *Physical Review Letters* 74.13 (Mar. 1995), pp. 2422–2426.

[11] *Top Working Group Summary Plots — Autumn 2018*. Tech. rep. ATL-PHYS-PUB-2018-034. Geneva: CERN, Nov. 2018.

[12] Gregory Mahlon and Stephen Parke. “Single Top Quark Production at the LHC: Understanding Spin”. In: *Phys.Lett. B* 476 (2000), pp. 323–330.

[13] Gregory Mahlon. “Spin Polarization in Single Top Events”. In: ().

[14] J. A. Aguilar-Saavedra. “New directions for top quark polarization in the t-channel process”. In: *Physical Review D* 89.11 (2014).

[15] J. A. Aguilar-Saavedra. “Single top quark production at LHC with anomalous Wtb couplings”. In: *Nucl. Phys.* B804 (2008), pp. 160–192.

[16] J.A. Aguilar-Saavedra, C. Degrande, and S. Khatibi. “Single top polarisation as a window to new physics”. In: *Physics Letters B* 769 (2017), pp. 498–502.

[17] ATLAS Collaboration. “Probing the”. In: (Feb. 2017).

[18] ATLAS Collaboration. “Analysis of the Wtb vertex from the measurement of triple differential angular decay rates of single top quarks produced in the t-channel at $\sqrt{s} = 8$ TeV with the ATLAS detector”. In: *Journal of High Energy Physics* 2017.12 (Dec. 2017).

[19] Reinhard Schwienhorst, C.-P. Yuan, Charles Mueller, and Qing-Hong Cao. “Single top quark production and decay in thetchannel at next-to-leading order at the LHC”. In: *Physical Review D* 83.3 (Feb. 2011).

[20] M. Jeżabek and J.H. Kühn. “V - A tests through leptons from polarised top quarks”. In: *Physics Letters B* 329.2-3 (June 1994), pp. 317–324.

[21] CMS Collaboration. “Measurement of top quark polarisation in t-channel single top quark production”. In: (Nov. 2015).

[22] M. Jacob and G.C. Wick. “On the General Theory of Collisions for Particles with Spin”. In: *Annals of Physics* 281.1 (2000), pp. 774–799.

[23] Joseph Boudreau, Carlos Escobar, James Mueller, Kevin Sapp, and Jun Su. “Single top quark differential decay rate formulae including detector effects”. In: (Apr. 2013).

[24] J.A. Aguilar-Saavedra, J. Boudreau, C. Escobar, and J. Mueller. “The fully differential top decay distribution”. In: (Feb. 2017).

[25] Christiane Lefèvre. “The CERN accelerator complex.” Dec. 2008.

[26] Lyndon Evans and Philip Bryant. “LHC Machine”. In: *JINST* 3 (2008), S08001.

[27] ATLAS Collaboration. *ATLAS: technical proposal for a general-purpose pp experiment at the Large Hadron Collider at CERN*. LHC Tech. Proposal. Geneva: CERN, 1994.

[28] CMS Collaboration. *Technical proposal*. LHC Tech. Proposal. Cover title : CMS, the Compact Muon Solenoid : technical proposal. Geneva: CERN, 1994.

[29] LHCb Collaboration. *LHCb : Technical Proposal*. Tech. Proposal. Geneva: CERN, 1998.

[30] W Kienzle, M Oriunno, Anne Laure Perrot, S Weisz, M Bozzo, A Buzzo, M Macri, A Santroni, G Settle, M Buénerd, F Malek, Y Muraki, K Kasahara, G Sanguinetti, Giorgio Matthiae, P Privitera, V Verzi, A Faus-Golfe, J Velasco, and S Torii. *TOTEM, Total Cross Section, Elastic Scattering and Diffraction Dissociation at the LHC: Technical Proposal*. Tech. rep. CERN-LHCC-99-007. LHCC-P-5. Geneva: CERN, Mar. 1999.

[31] ALICE Collaboration. *ALICE: Technical proposal for a Large Ion collider Experiment at the CERN LHC*. LHC Tech. Proposal. Geneva: CERN, 1995.

[32] *ATLAS Collaboration, Luminosity Public Results*. https://twiki.cern.ch/twiki/bin/view/AtlasPublic/LuminosityPublicResultsRun2.

[33] *ATLAS inner detector: Technical Design Report, 1*. Technical Design Report ATLAS. Geneva: CERN, 1997.

[34] Krzysztof Sliwa. “”ATLAS Overview and Main Results””. In: *Proceedings, International School on High Energy Physics : Workshop on High Energy Physics in the near Future. (LISHEP 2013): Rio de Janeiro, Brazil, March 17-24, 2013*. 2013.

[35] N Ilic. “Performance of the ATLAS Liquid Argon Calorimeter after three years of LHC operation and plans for a future upgrade”. In: *Journal of Instrumentation* 9.03 (Mar. 2014), pp. C03049–C03049.

[36] C. Grupen and B. Shwartz. *Particle Detectors*. Cambridge Monographs on Particle Physics, Nuclear Physics and Cosmology. Cambridge University Press, 2008.

[37] Ricardo Achenbach, Paolo Adragna, M Aharrouche, Andrei Kelarev, B Asman, B Barnett, B Bauss, M Bendel, Christian Bohm, J Booth, J Bracinik, I Brawn, D Charlton, John Taylor Childers, N Collins, C Curtis, A Davis, S Eckweiler, E Eisenhandler, and M Wildt. “Analysis of the initial performance of the ATLAS Level-1 Calorimeter Trigger”. In: (Jan. 2008).

[38] T Cornelissen, M Elsing, S Fleischmann, W Liebig, E Moyse, and A Salzburger. *Concepts, Design and Implementation of the ATLAS New Tracking (NEWT)*. Tech. rep. ATL-SOFT-PUB-2007-007. ATL-COM-SOFT-2007-002. Geneva: CERN, Mar. 2007.

[39] M. Aaboud, G. Aad, B. Abbott, J. Abdallah, O. Abdinov, B. Abeloos, R. Aben, O. S. AbouZeid, N. L. Abraham, and et al. “Reconstruction of primary vertices at the ATLAS

experiment in Run 1 proton–proton collisions at the LHC". In: *The European Physical Journal C* 77.5 (May 2017).

[40] G. Aad, B. Abbott, J. Abdallah, A. A. Abdelalim, A. Abdesselam, O. Abdinov, B. Abi, M. Abolins, H. Abramowicz, and et al. "Electron performance measurements with the ATLAS detector using the 2010 LHC proton-proton collision data". In: *The European Physical Journal C* 72.3 (Mar. 2012).

[41] W. Lampl, S. Laplace, D. Lelas, P. Loch, H. Ma, S. Menke, S. Rajagopalan, D. Rousseau, S. Snyder, and G. Unal. "Calorimeter clustering algorithms: Description and performance". In: (2008).

[42] Alexey Ezhilov. *Electrons in ATLAS: from Run1 to Run2*. Tech. rep. ATL-PHYS-PROC-2015-180. Geneva: CERN, Dec. 2015.

[43] G. Aad, B. Abbott, J. Abdallah, S. Abdel Khalek, O. Abdinov, R. Aben, B. Abi, M. Abolins, O. S. AbouZeid, and et al. "Measurement of the muon reconstruction performance of the ATLAS detector using 2011 and 2012 LHC proton–proton collision data". In: *The European Physical Journal C* 74.11 (Nov. 2014).

[44] G. Aad, B. Abbott, J. Abdallah, O. Abdinov, B. Abeloos, R. Aben, M. Abolins, O. S. AbouZeid, N. L. Abraham, and et al. "Muon reconstruction performance of the ATLAS detector in proton–proton collision data at $\sqrt{s} = 13$TeV". In: *The European Physical Journal C* 76.5 (May 2016).

[45] G. Aad et al. "Muon reconstruction performance of the ATLAS detector in proton–proton collision data at $$\sqrt{s}$$s=13 TeV". In: *The European Physical Journal C* 76.5 (2016), p. 292.

[46] Matteo Cacciari, Gavin P Salam, and Gregory Soyez. "The anti-kt jet clustering algorithm". In: *Journal of High Energy Physics* 2008.04 (Apr. 2008), pp. 063–063.

[47] "Performance of b-jet identification in the ATLAS experiment". In: *Journal of Instrumentation* 11.04 (Apr. 2016), P04008–P04008.

[48] *Expected performance of the ATLAS b-tagging algorithms in Run-2*. Tech. rep. ATL-PHYS-PUB-2015-022. Geneva: CERN, July 2015.

[49] M. Aaboud, G. Aad, B. Abbott, O. Abdinov, B. Abeloos, S. H. Abidi, O. S. AbouZeid, N. L. Abraham, H. Abramowicz, and et al. "Performance of missing transverse momentum reconstruction with the ATLAS detector using proton–proton collisions at$\sqrt{s} = 13$TeV". In: *The European Physical Journal C* 78.11 (Nov. 2018).

[50] ATLAS Collaboration. "TopCommonObjects13TeV twiki". In: (2018).

[51] M. Tanabashi et al. "Review of Particle Physics". In: *Phys. Rev.* D98.3 (2018), p. 030001.

[52] Rikkert Frederix, Emanuele Re, and Paolo Torrielli. "Single-top t-channel hadroproduction in the four-flavour scheme with POWHEG and aMC@NLO". In: *JHEP* 09 (2012), p. 130.

[53] Paolo Nason. "A New Method for Combining NLO QCD with Shower Monte Carlo Algorithms". In: *Journal of High Energy Physics* 2004.11 (Nov. 2004), pp. 040–040.

[54] Simone Alioli, Paolo Nason, Carlo Oleari, and Emanuele Re. "A general framework for implementing NLO calculations in shower Monte Carlo programs: the POWHEG BOX". In: *Journal of High Energy Physics* 2010.6 (June 2010).

[55] J. Alwall, R. Frederix, S. Frixione, V. Hirschi, F. Maltoni, O. Mattelaer, H.-S. Shao, T. Stelzer, P. Torrielli, and M. Zaro. "The automated computation of tree-level and next-to-leading order differential cross sections, and their matching to parton shower simulations". In: *Journal of High Energy Physics* 2014.7 (July 2014).

[56] Torbjörn Sjöstrand, Stephen Mrenna, and Peter Skands. "A brief introduction to PYTHIA 8.1". In: *Computer Physics Communications* 178.11 (June 2008), pp. 852–867.

[57] Manuel et al. Bähr. "Herwig++ physics and manual". In: *The European Physical Journal C* 58.4 (Nov. 2008), pp. 639–707.

[58] S. Agostinelli and J. Allison et.al. "Geant4—a simulation toolkit". In: *Nuclear Instruments and Methods in Physics Research Section A: Accelerators, Spectrometers, Detectors and Associated Equipment* 506.3 (2003), pp. 250–303.

[59] Elzbieta Richter-Was, D Froidevaux, and Luc Poggioli. *ATLFAST 2.0 a fast simulation package for ATLAS*. Tech. rep. ATL-PHYS-98-131. Geneva: CERN, Nov. 1998.

[60] M. A. Dobbs, S. Frixione, E. Laenen, K. Tollefson, H. Baer, E. Boos, B. Cox, R. Engel, W. Giele, J. Huston, S. Ilyin, B. Kersevan, F. Krauss, Y. Kurihara, L. Lonnblad, F. Maltoni, M. Mangano, S. Odaka, P. Richardson, A. Ryd, T. Sjostrand, P. Skands, Z. Was, B. R. Webber, and D. Zeppenfeld. *Les Houches Guidebook to Monte Carlo Generators for Hadron Collider Physics*. 2004.

[61] Stefano Frixione, Eric Laenen, Patrick Motylinski, and Bryan R. Webber. "Angular correlations of lepton pairs from vector boson and top quark decays in Monte Carlo simulations". In: *JHEP* 0704 (2007), p. 081.

[62] D. J. Lange. "The EvtGen particle decay simulation package". In: *Nucl. Instrum. Meth. A* 462 (2001), p. 152.

[63] P. Kant, O. M. Kind, T. Kintscher, T. Lohse, T. Martini, S. Mölbitz, P. Rieck, and P. Uwer. "HatHor for single top-quark production: Updated predictions and uncertainty estimates for single top-quark production in hadronic collisions". In: *Comput. Phys. Commun.* 191 (2015), pp. 74–89.

[64] ATLAS Collaboration. "Luminosity determination in pp collisions at $\sqrt{s} = 7\,\text{TeV}$ using the ATLAS detector at the LHC". In: *Eur. Phys. J. C* 71 (2011), p. 1630.

[65] G. Avoni et al. "The new LUCID-2 detector for luminosity measurement and monitoring in ATLAS". In: *JINST* 13.07 (2018), P07017.

[66] Zachary Marshall. "Simulation of Pile-up in the ATLAS Experiment". In: *J. Phys. Conf. Ser.* 513 (2014), p. 022024.

[67] *Electron efficiency measurements with the ATLAS detector using the 2015 LHC proton-proton collision data*. Tech. rep. ATLAS-CONF-2016-024. Geneva: CERN, June 2016.

[68] *Electron and photon energy calibration with the ATLAS detector using data collected in 2015 at* $\sqrt{s} = 13\,\text{TeV}$. Tech. rep. ATL-PHYS-PUB-2016-015. Geneva: CERN, Aug. 2016.

[69] *Tagging and suppression of pileup jets with the ATLAS detector*. Tech. rep. ATLAS-CONF-2014-018. Geneva: CERN, May 2014.

[70] ATLAS Collaboration. "Jet energy scale measurements and their systematic uncertainties in proton–proton collisions at $\sqrt{s} = 13\,\text{TeV}$ with the ATLAS detector". In: *Phys. Rev. D* 96 (2017), p. 072002.

[71] ATLAS Collaboration. "Small-R ($R = 0.4$) jet energy scale and jet energy resolution uncertainties for full Run 2 analyses (release 21) twiki". In: (2019).

[72] ATLAS Collaboration. "Performance of b-jet identification in the ATLAS experiment". In: *JINST* 11 (2016), P04008.

[73] ATLAS Collaboration. "Top quark mass measurements". In: (2009).

[74] G. Aad et al. "Expected Performance of the ATLAS Experiment - Detector, Trigger and Physics". In: (2009).